Esta tesis cumple los requisitos necesarios para su publicación.
This thesis meets the appropriate criteria for publication.

1. Supervisor: Dr. Evencio Mediavilla Grádolph

2. Supervisor: Dr. Alejandro Oscoz Abad

Microlensing of AGN Spectra

Eduardo Guerras Valera

Instituto de Astrofísica de Canarias

A thesis submitted for the degree of

Doctor en Ciencias Físicas

2014

Abstract

Quasars are high redshift, extremely bright star-like objects identified with radio sources, that present large UV fluxes, prominent broad and narrow lines and a time-variable continuum flux (e.g. Schmidt 1969). They are considered to be the most luminous subclass among Active Galactic Nuclei. Although they appear to be distributed everywhere in the Universe, only a small fraction of them happen to be part of a fortuitous alignment with a galaxy or a galaxy cluster that lies along the line-of-sight, which results in multiple images of the background quasar by means of gravitational lensing. Compact objects, such as stars in the bulges or halos of the galaxies, may induce further changes in the mean lensing magnification that are uncorrelated among images. This *microlensing* effect due to unseen star-sized objects can be used to extract information about both the source quasar and the lens galaxy.

The small size of the emitting quasar regions, together with involved distances in the Gpc range, make spatially resolved observations of the background quasar hopeless, even with the largest available optical telescopes. Direct observation of the microlenses at such distances is also impossible. Microlensing can help overcoming these difficulties, at least in two ways:

- Microlensing magnification is very sensitive to the degree of alignment of the system. Thus, relative movement of the microlenses with respect to the background quasar causes measurable changes in brightness over finite periods of time.
- Although we cannot spatially resolve the image of the emitter, we have a growing number of detailed quasar spectra. Flux measures can be done across different constituents of the spectra (narrow and wide

emission lines, continuum flux, blended emission bands) that arise from regions with different sizes. As microlensing is sensitive to size, we can expect different microlensing magnifications for different constituents of the spectra.

In fact, nearly all we know from quasars has been inferred by studying their spectra, that are extraordinary rich. There is a time-variable continuum emission spanning several orders of magnitude in wavelength, whose generating mechanism can be explained by a dissipative accretion disk around a very massive object (e.g. Salpeter 1964 , Shakura & Sunyaev 1973). Broad emission lines follow the continuum variability pattern after different time delays, that have been used to impose upper limits on the distance to the central engine. This technique, known as *Reverberation Mapping* (e.g. Kollatschny 2010) can be applied to any of the known quasars as long as there is a high enough S/N ratio, but observation campaigns over long periods of time are required.

Microlensing is based upon a different approach that can help overcoming the difficulties of Reverberation Mapping, though it faces another challenging circumstances. Quasars undergoing strong lensing are only a small and rare subset. Moreover, the fraction of them that are brilliant enough as to allow detailed spectra is small. In addition to that, the observations are technically challenging, since they must consist on two independent, simultaneous long slit spectra with no contamination from each other, being the images only a few arc seconds apart. This has only been achieved for roughly a couple dozens of these objects. The authors did in each case their best to derive properties based on the detected microlensing signal, although the involved physical quantities are strongly unconstrained *when dealing with a single object.*

That is the starting point of this thesis, in which we bring together as many as possible of such spectra from the literature, with the goal of studying properties that could not be studied individually, of both the source quasar and the lens galaxy. The work requires collecting the data, designing the appropriate measuring process, generating sets of simulations to compare

the measures with, applying the Bayesian inference methods, and offering an interpretation of the results.

The thesis is structured in seven chapters:

Chapter 1 presents a theoretical introduction gathering the essentials required to work on extragalactic microlensing. It is deliberately short and has a personal taste: I have just lead the reader directly to whatever is strictly relevant, though aiming to self-consistency.

Chapter 2 presents a short motivation statement, explaining the need for this thesis work and why it may be useful for the scientific community. It develops, in short, the main motivation: processing a sample of lensed quasar spectra and build a single-epoch statistical study out of them, that overcomes the limitations of the individual object approach and the lack of observation campaigns over long periods of time.

In **Chapter 3** I present a consistent overview of all the spectra, brought together over a common wavelength scale, after their continua have been subtracted, and scaled so that they roughly overlap. This is intended to be a quick visual reference to the information and possibilities contained in each spectral pair (e.g. which lines are present, how the line profiles overlap, or where anomalies in the profiles lie and how consistently they appear in different emission lines).

Chapters 4 to 7 present the research papers that constitute the bulk of this thesis:

Chapter 4 sets the upper boundary on the content in MACHOs of extragalactic lens halos in less than 10% (Mediavilla et al. 2009), concluding that microlensing is likely caused by normal star populations.

Chapter 5 studies the size and temperature profile of the accretion disk of SBS 0909+532 (Mediavilla et al. 2011), showing that they are compatible with the thin disk theory.

Chapter 6 constraints the average size of the Broad Line Region (Guerras et al. 2013), obtaining results that are consistent with Reverberation Mapping studies.

Chapter 7 establishes the likely origin of the ionized iron emission bands in the very central part of the quasar engine (Guerras et al. 2014).

Chapter 8 summarizes the main conclusions of the thesis and offers some suggestions for future work in the field.

This thesis is dedicated to Ángela Guerras.

Contents

1

Theory Overview

1.1 Multiple mirages

Theories modeling the behavior of light have driven several revolutions in physics. Although the underlying theories are very different, there is one statement that survives, adapted to each particular formulation. It is Fermat's principle, that tells us that light, whatever it is, can be thought as something that leaves the source and reaches the observer through paths along which the total travel time is *stationary*:

$$\delta \int_{t_A}^{t_B} dt = 0 \tag{1.1}$$

By *Stationary* here it is understood, that any paths followed by light cannot be modified without increasing the total travel time, it is therefore a minimum travel time path. This is often misunderstood by stating that *light "chooses" the minimum time path*, which is incorrect: *if the physical conditions between the source and the observer allow for several stationary paths, light will choose all them simultaneously*, resulting in several images that arrive at the observer:

- from different angles, thus different apparent positions,
- after different time delays, depending on each path,
- having suffered different physical processes along each path (scattering, reddening...)
- subtending different solid angles, thus different magnifications.

This is the *raison-d'etre* of ordinary mirages. The physical mechanism underlying the possibility of curved stationary paths are the spatial variations of the speed of light, due to the physical conditions of the air at different points, since the latter formula for Fermat's principle can be written as

$$\delta \int_A^B \frac{dl}{c} = 0$$

which results in a straight line only if c is constant all along the way.

Another reason for spatial variations of the speed of light is the presence of a gravitational potential. We can get a position-dependent expression of the speed of light to plug into the integral, for most astrophysical application in which the spacetime metric $g_{\mu\nu}$ is nearly flat, by using that of Special Relativity $\eta_{\mu\nu}$ plus a small isotropic perturbation $A\delta_{\mu\nu}$:

$$g_{\mu\nu} \approx \eta_{\mu\nu} + A\delta_{\mu\nu}$$
$$|A| \ll 1$$

In order to get Newtonian gravity asymptotically from this, A must be the Newtonian gravitational potential ϕ scaled,

$$A = \frac{2\phi}{c^2}$$

Therefore, the infinitesimal interval is:

$$ds^2 = (1 + \frac{2\phi}{c^2})c^2dt^2 - (1 - \frac{2\phi}{c^2})(dx^2 + dy^2 + dz^2) \tag{1.2}$$

But photons evolve in phase space along null geodesics, therefore $ds^2 = 0$ and we can get an expression for the equivalent speed of light (squared) as measured by an asymptotic observer, in the so-called *weak field approximation*:

$$c'^2 = \frac{(dx^2 + dy^2 + dz^2)}{dt^2} = c^2\frac{1 + \frac{2\phi}{c^2}}{1 - \frac{2\phi}{c^2}}$$

Since $\frac{2\phi}{c^2} \ll 1$, $(\sqrt{\frac{1+x}{1-x}})^{-1} \approx 1 - x$, then:

$$\frac{1}{c'} = \frac{1}{c}(1 - \frac{2\phi}{c^2})$$

Therefore, Fermat's principle can be written as:

$$\delta \int_A^B (1 - \frac{2\phi}{c^2}) dl = 0 \tag{1.3}$$

where ϕ is the Newtonian potential. Solving for the path $x(l), y(l), z(l)$ under certain simplifying assumptions allows predicting and modeling gravitational mirages with multiple images that present the same four characteristics mentioned at the beginning of the section for ordinary mirages.

1.2 Historical Notes

Einstein had famously predicted light paths would bend 1.7 arcsec near the Sun in 1916 (Einstein 1916). In 1924 the Russian O. Chwolson (Chwolson 1924) realized the possibility of a fictitious spectroscopic double star, being one of the components a gravitationally deflected image from a star in another position.

He also correctly predicted that, in case of a perfect alignment, a ring-shape image would happen. Einstein analyzed the question in 1936 (Einstein 1936). We will later (sec. 1.5.1) derive the angular radius of such ring-shaped image (known in the literature as *Einstein Ring*), which is:determinate

$$\theta_E = \sqrt{\frac{4GM}{c^2} \frac{D_{ds}}{D_d D_s}} \tag{1.4}$$

where D_d,D_s,D_{ds} are the distances to the deflector, to the source and between them, respectively, and M is the mass of the deflector. Einstein was a theoretician and the notion of the Island Universe was probably still present in the backyard of his mind in 1936, so he only thought about the scenario of light deflection by single stars, which, according to this formula, gives an angular size of roughly 10^{-3} arc seconds, hopelessly beyond telescope resolution. However, a short increase in bright could be detected during the alignment. *There is no great chance of observing this phenomenon* was therefore his conclusion.

It was an astronomer, Fritz Zwicky, who realized in 1937 (Zwicky 1937) that the gravitationally-induced fictitious Chwolson objects and Einstein rings would be still resolvable with optic telescopes, when the involved masses were those of galaxies and

the distances in the cosmological range. In that case, the Einstein rings would have an angular diameter of several arc seconds.

When Zwicky died in 1974, the first detection of such phenomenon still was waiting to happen. Gravitational lensing research was then as a speculative field as astrobiology today. Models had been made and complete theories analyzing the mapping properties between source and image plane, number of images and so on had been developed. Predictions had been made about how gravitational lenses would help determining Hubble constant, constraint galaxy masses, rule out cosmological theories, et cetera (e.g. Refsdal 1964, Refsdal 1966) but not a single real example was known.

The first detection happened in 1979 (Walsh et al. 1979). A galaxy at $z = 0.36$ nearly perfectly aligned with a quasar at $z = 1.41$, produces two images with the same spectral fingerprint of the background object.

Other many detections have followed. Typically the lens is a galaxy or a cluster of galaxies, but sometimes the lens object is unseen. The background sources are usually galaxies and quasars. There are some ring-shaped images and giant arcs, but in the typical scenario of the kind of objects we deal with in this thesis, an asymmetric lens mass distribution together with a slight misalignment of the system produces multiple images of a background quasar.

In such systems the four characteristics of mirages mentioned above can be observed. In particular, we are interested here in the information carried by some specific way in which matter along the light paths affects each image, called *differential gravitational microlensing*.

1.3 Quasars

Quasars are high redshift, extremely bright star-like objects identified with radio sources, that present large UV fluxes, prominent broad and narrow lines and a time-variable continuum flux (Schmidt 1969). Their large luminosity arises from a region whose size is thought to be no larger than a few light-days across, so that spatially resolved images are impossible. However, quasars present the richest and most complex spectra among all astronomical objects. There is a time-variable continuum emission spanning several orders of magnitude in wavelength, whose mechanism can be explained by a dissipative accretion disk around a very massive object (e.g. Salpeter 1964, Shakura & Sunyaev

1973), and an superposed rich emission line spectrum with broad and narrow components that follow the variability pattern of the continuum with different amplitudes and after different time delays. An average QSO spectrum as shown in Francis et al. 1991 can be seen in Figure 1.1. The dashed and dotted lines show a fit to the continuum and the blended Iron line emission respectively.

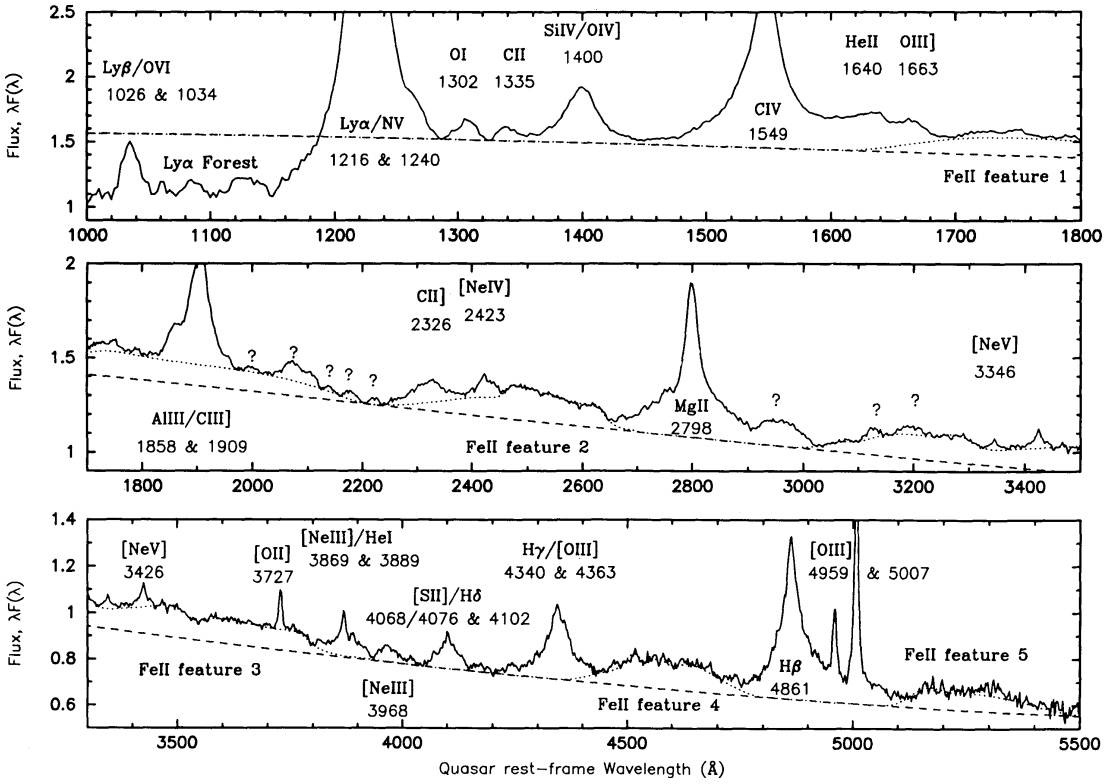

Figure 1.1: Detailed identification of QSO spectral features in Francis et al. 1991

Narrow and broad emission lines do not vary simultaneously, though their time variation patterns can be related. This all suggested from the beginning that quasars have a structure formed by different, dynamically interacting elements of several size scales.

Time variations in the different spectral components lead to modeling of the quasar engine. The typical time variation scale of the continuum flux is of several days, therefore suggesting an upper limiting size of some light-days for the emitting region. This variations are usually correlated with weaker variations in the different emission lines that follow after some longer delay, thus allowing for size estimations based on the finite

speed of propagation of the perturbation, a technique known as *reverberation mapping* (e.g. Kollatschny 2010)

This all lead to the standard model of quasar, whose structure can be summed up as:

- A Shakura-Sunyaev accretion disk at the very center, around a supermassive black hole. This is the origin of the synchrotron continuum. Magnetohydrodynamic instabilities in the disk and changes in opacity would lead to continuum variability. The enormous quasar intrinsic luminosity mostly arises from thermalization of gravitational potential energy here, as a result of a high accretion rate of matter, typically in the range of 1 to 10 $M_{\odot}\, yr^{-1}$ (Carroll & Ostlie 2007)
- A surrounding region with hot, quickly orbiting clouds that are the origin of broad lines by means of Doppler broadening, known as the Broad Line Region, hence BLR.
- A much bigger region with slow moving, low density gas clouds, origin of the narrow lines, hence NLR.
- A couple of collimated jets, mostly emitting in the radio range.
- An obscuring torus, essential to unify the zoo of active galaxies as merely the same kind of structure but seen from different angles.

Each of this structures leaves its trace in the spectra of the quasar (see Figure 1.2).

The time it takes for the central engine flux changes to propagate to the line emitting regions, is the tool upon which reverberation mapping measures are based. But, when the quasar is part of a gravitational lens, there are other ways in which the variability helps extracting information about the system.

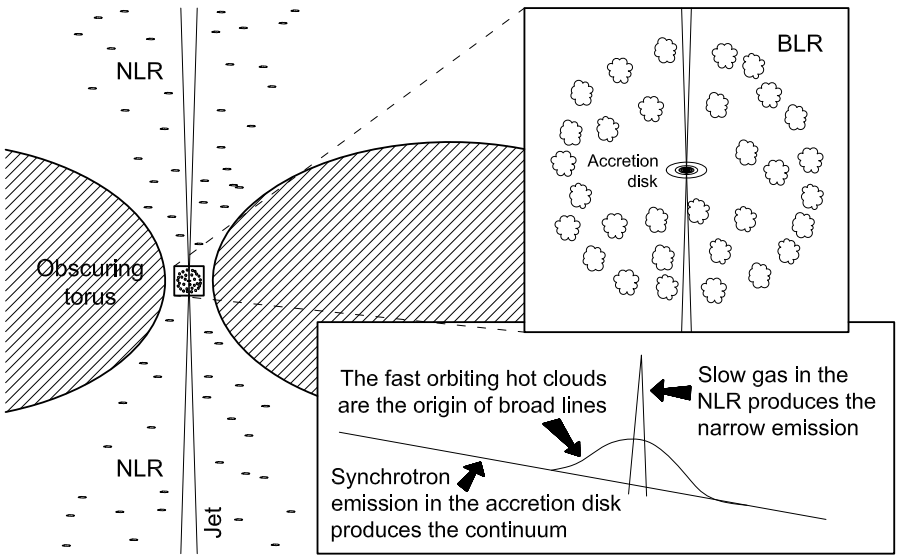

Figure 1.2: Schematic view of the different structures giving rise to the common QSO spectral features

1.4 Shapiro time delays

Back to our weak-field version of Fermat's principle (eq. 1.3), it is easy to obtain the total travel time along each path between the source and the observer, as

$$t = \frac{1}{c}\int_0^S (1 - \frac{2\phi}{c^2})dl = \frac{1}{c}\int_0^S dl - \int_0^S \frac{2\phi}{c^3}dl$$

where S is the total length along the geometrical path. Note that this expression corresponds to the travel time along the path in the absence of gravitational potential plus the so-called *Shapiro delay* (Shapiro 1964).

In a lensed quasar with several images, flux variations following physical changes at the source are not observed simultaneously through all the images due to Shapiro delays. Relating the time shifts between the light curves to a model of the lens allows for an estimation of the mass generating the potential ϕ. An example is SDSS J1029+2623 (Fohlmeister et al. 2013), where light curves can be superposed only after a relative shift of two-years (see Fig. 1.3).

However, in many cases an accurate superposition of the light curves is not possible (e.g. Keeton et al. 2006, or Morgan & Kochanek 2006, see Fig. 1.4). In those cases, there is some physical phenomenon introducing additional uncorrelated flux variations. The best explanation is additional gravitational lensing on a smaller scale due to the presence of mass substructure in the galaxy acting as a lens. We will expand this idea in the following sections.

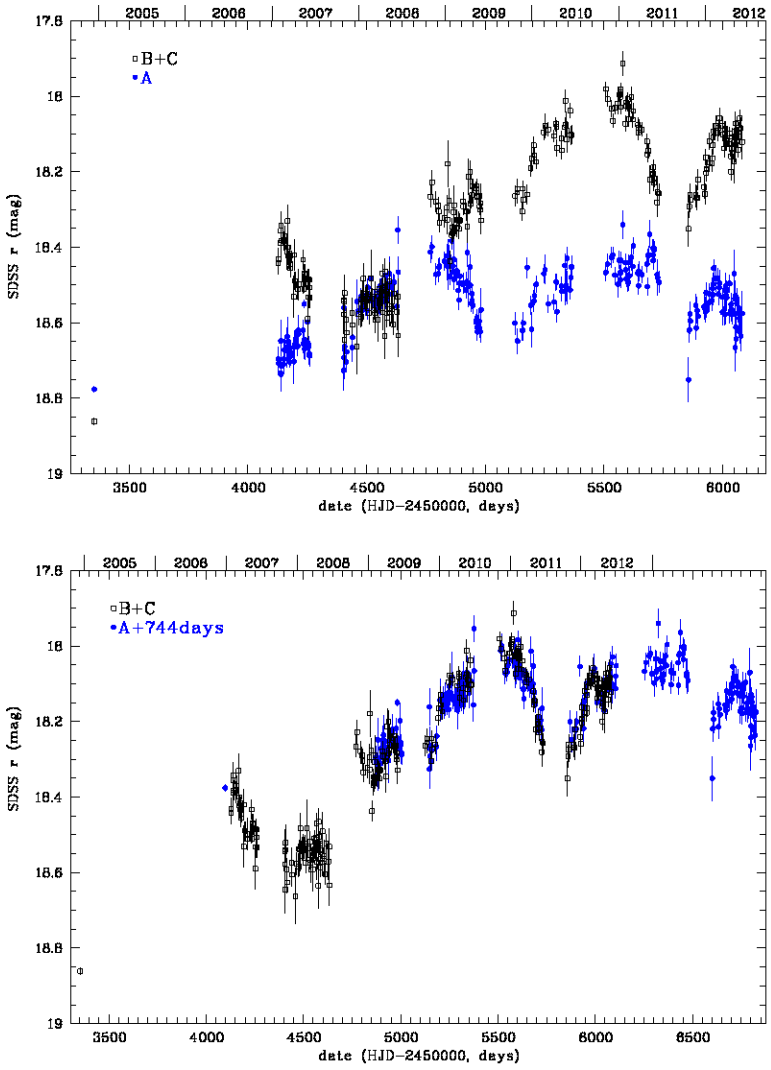

Figure 1.3: On the upper image, raw light curves for SDSS J1029+2623. After a two-year shift they superimpose nicely (lower image). This is not always possible. From Fohlmeister et al. 2013

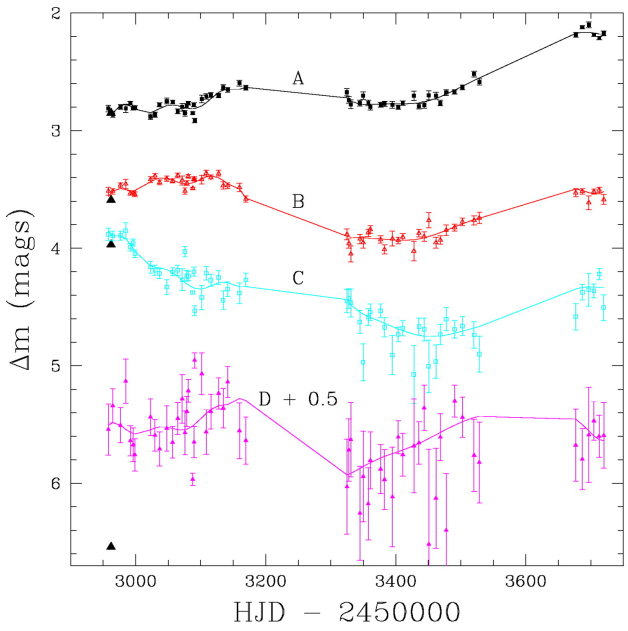

Figure 1.4: Differential Microlensing induced variability in SDSS J0924+0219, as shown in Morgan et al. 2006. The microlensing component of the variability is so strong in this system, that Shapiro delays could not be estimated.

1.5 The basics of Gravitational Lensing

In the usual lensed system, the background quasar is split into several images. Additionally, these images cross the lens galaxy and its halo at different points. As part of the galaxy mass is not smoothly distributed but highly heterogeneously distributed in point-like stars, the gravitational potential has strong local changes that may induce strong and uncorrelated changes in the image magnifications. Since the stars have transverse speeds, a variable component is superposed to that of the continuum source, making it difficult to estimate the Shapiro time delays.

This scenario that consists on a soft varying potential from the bulk mass of the galaxy with the addition of point-like deflectors to account for mass substructure, is the one we are going to rely on for the rest of the thesis. However we are neglecting the likely presence of intermediate-sized dark matter clumps, that might introduce some inaccuracies, specially in close-separation pairs (Xu el al. 2013, Zackrisson & Riehm 2010).

Therefore, we will deal with the same physical phenomenon, acting on two different spatial and time scales:

- Splitting of the source image in several images, caused by the soft-varying potential created by the lens galaxy bulk mass, in the *strong lensing regime*.
- Additional magnification with different time scales due to line-of-sight cross crossing compact objects, in the *microlensing regime*.

Both phenomena must be addressed with quite different tools. A minimalist overview follows:

1.5.1 Introducing lensing by spherically symmetric mass distributions

We followed above some steps similar to those in Einstein's famous 1916 paper (Einstein 1916) to obtain the speed of light in the presence of a weakly perturbed flat metric. Near the end of that paper is the derivation for the bending angle of light paths grazing the surface of the Sun. Let γ denote the speed of a light beam in $c = 1$ units (refractive index) that propagates according to Fig. 1.5. Then:

> *We can easily see that, with reference to the co-ordinate system, the rays of light must appear curved in case $g_{\mu\nu}$ are not constant.*
>
> *If n be the direction perpendicular to the direction of propagation, we have, from Huygen's principle, that light-rays (taken in the plane (γ, n)) must suffer a curvature $-d\gamma/\partial n$.*
>
> *We find out the curvature which a light-ray suffers when it goes by a mass M at a distance Δ from it. If we use the co-ordinate system according to the above scheme, then the total bending B of light-rays (reckoned positive when it is concave to the origin) is given as a sufficient approximation by*

$$B = \int_{-\infty}^{+\infty} \frac{\partial \gamma}{\partial x_1} dx_2$$

That *sufficient approximation* is analogous to the Born approximation to scattering (Born 1926), which essentially integrates the transversal change in momentum along an unperturbed, straight path between the source plane and the observer instead of

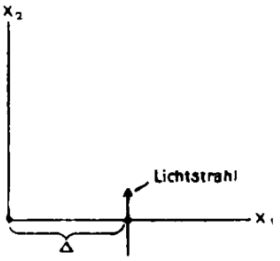

Figure 1.5: A light beam goes by a mass M at the origin of a (x_1, x_2) coordinate system in the vertical direction at a minimum distance Δ, as depicted in Einstein 1916

doing it along the real, curved path. The result, for a spherically symmetric inner mass M, is:

$$B = \frac{4GM}{c^2\Delta} \tag{1.5}$$

This allows to set a simple lensing scenario (figure 1.6).

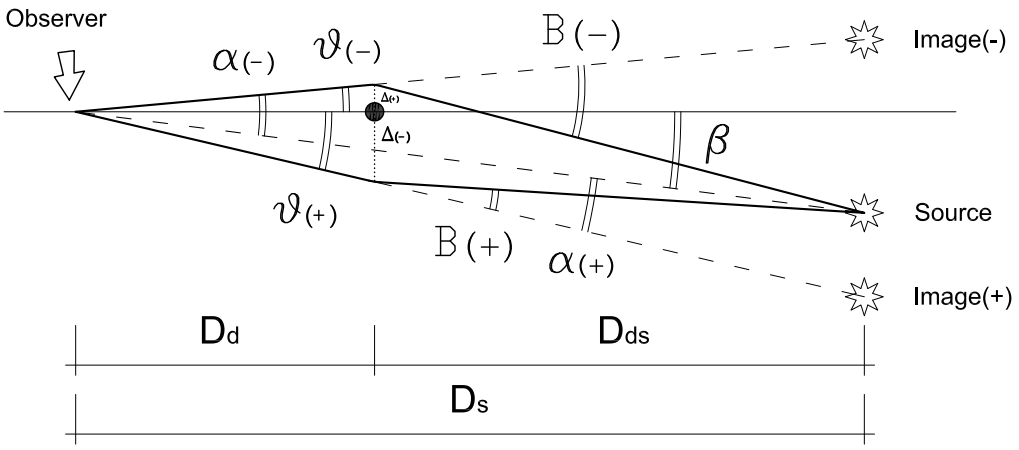

Figure 1.6: Lens equation geometry

The relation between source and image angular positions, β and θ respectively, follows from figure 1.6:

$$\beta + \alpha = \theta$$

where the usual sign criterion has been adopted. The symmetry of the system implies that all rays belong to the same plane. There are two stationary trajectories for a spherically symmetric lens, as we are about to see analytically, each associated with positive (just deviated image) or negative parity (deviated and mirrored image).

Since all angles are small, it follows

$$\alpha D_s = B D_{ds}$$

$$D_d \theta = \Delta$$

therefore

$$\beta(\theta) = \theta - \frac{D_{\rm ds}}{D_{\rm d} D_{\rm s}} \frac{4GM(\theta)}{c^2\,\theta} \tag{1.6}$$

is the *lens equation* that relates θ (angular position of an image) with β (true angular position of the unlensed source). $M(\theta)$ is the axially symmetric mass enclosed by the angular radius θ.

Note that we have assumed the validity of *high = angle* $\times$ *distance* which implies that we are dealing with *angular-diameter distances*. Note too, that in the cosmological range, $D_{ds} \neq D_s - D_d$.

A very interesting feature of this equation is the degeneracy of the solution for a perfectly aligned source ($\beta = 0$), which represents an axially symmetric image (the *Einstein ring* θ_E, see eq. 1.4) whose radius is found by setting $\beta = 0$ in the lens equation (eq. 1.6) and solving for θ:

$$0 = \theta_E - \frac{D_{\rm ds}}{D_{\rm d} D_{\rm s}} \frac{4GM(\theta_E)}{c^2 \theta_E}$$

$$\theta_E = \sqrt{\frac{4GM(\theta_E)}{c^2} \frac{D_{ds}}{D_d D_s}} \tag{1.7}$$

The lens equation can be written in a particularly simple way by means of the Einstein radius:

$$\beta = \theta - \frac{\theta_{\rm E}^2(\theta)}{\theta} \tag{1.8}$$

However, note that the dependency of θ_E with θ is given by the particular mass distribution of the lens (in other words, knowledge of $M(\theta_E)$ is required in advance, before being able to solve for θ_E in eq. 1.7). Thus, as simple as it might seem, there is no general solution to equation eq. 1.8, and one of the difficulties in real astrophysical lensing problems is the need of assuming a specific mass model for the deflector.

1.5.2 The Simplest Lens Model

The so-called *Schwarzschild lens* consist on a point mass as deflector. In this simple case $M(\theta) = M$, the Einstein angle is a constant, and the lens equation is easily solved:

$$\beta = \theta - \frac{\theta_{\rm E}^2}{\theta} \tag{1.9}$$

There are always two solutions, outside and inside a (fictitious) ring with radius θ_E:

$$\theta_{\pm} = \frac{1}{2}\left(\beta \pm \sqrt{\beta^2 + 4\theta_{\rm E}^2}\right) \tag{1.10}$$

Conservation of étendue in phase space (Winston et al. 2004) assures that the flux per unit solid angle is not altered by gravitational lensing. This leads to define *magnification* of each image as the ratio between the projected area of the image and source[1]. From fig. 1.7 we have:

$$\mu = \frac{\theta}{\beta}\frac{d\theta}{d\beta} \tag{1.11}$$

By differentiation of 1.9, this can be written as a function of the image position alone:

$$\mu(\theta_{\pm}) = \left[1 - \left(\frac{\theta_{\rm E}}{\theta_{\pm}}\right)^4\right]^{-1}$$

which shows that

[1] This is a general definition. See also explanation in sec. 2.3 of Schneider & Ehlers & Falco 1992

- the negative parity image (inside one Einstein radius) is demagnified,
- the positive parity image (outside one Einstein radius) is magnified,
- adding $\mu_+ + \mu_-$ results always in an increase in the total magnification
- as β approaches zero, θ become θ_E, and the total magnification becomes infinite
- as β becomes bigger the negative image gets infinitely demagnified and close to the center, whereas the positive image becomes the source.

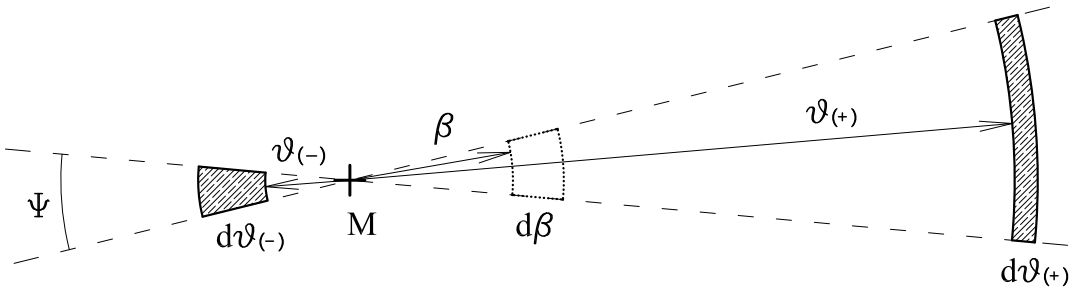

Figure 1.7: When the projected size of the source is smaller than the Einstein radius of the lens, the magnifications as quotient of areas follow straightforwardly.

1.5.3 Introducing Reduced Lens Equations

All systems with the same kind of mass distribution have lens equations that differ only by the value of θ_E. Thus it is convenient to reduce all angles to normalized distances by means of the Einstein angle:

$$x = \frac{\theta}{\theta_{\rm E}} \ , \ y = \frac{\beta}{\beta_{\rm E}} \tag{1.12}$$

A usual alternative is dealing with linear distances at the lens or source. Then, normalization is done by dividing distances by the *characteristic length in the lens plane* ξ_0, or the *characteristic length in the source plane* η_0, which are simply the projected distances $\theta_E D_d$ and $\theta_E D_s$ respectively.

Equation 1.9 results particularly simple:

$$y = x - \frac{1}{x}$$

An analogous procedure is defined for more complex lens models. In general, the reduced lens equation has the form

$$\vec{y} = \vec{x} - \vec{\alpha} \tag{1.13}$$

where the deflection $\vec{\alpha}$ depends on the mass distribution model we use for the lens.

1.5.4 Lensing as a mapping

The time spent by the photons within the influence of the lens potential is completely negligible, as compared with their total travel time from the source to us. This justifies the *thin screen approximation*, in which the mass distribution of the lens in projected in a single plane, normal to the line-of-sight.

The deflection angle in eq. 1.5 is linear in M, therefore a superposition principle holds, and a first approach to a more complex lens mass distribution is simply a collection of point masses:

$$\vec{B}(\vec{r}) = \sum_i \frac{4Gm_i}{c^2} \frac{\vec{r} - \vec{r}_i}{|\vec{r} - \vec{r}_i|^2} \tag{1.14}$$

where $\vec{r} - \vec{r}_i$ is the impact vector[1] for light rays for the mass m_i, as they cross the *lens plane*. The analogous expression for a continuous distribution (see Fig. 1.8) is

[1]We will use the notation $\vec{\theta}$ and $\vec{r}$ indistinctly. All angles in the lensing problem are very small, and we always deal with projected linear distances. Not to be confused with the notation $\vec{x}, \vec{y}$ that is usually reserved for *normalized* distances (this will be in any case specified in the text)

$$\vec{B}(\vec{r}) = \frac{4G}{c^2} \int \frac{\vec{r} - \vec{r}\,'}{|\vec{r} - \vec{r}\,'|^2} \Sigma(\vec{r}\,') d^2 r\,' \tag{1.15}$$

where $\Sigma(\vec{r}\,')$ denotes the *surface mass density* [1] obtained by projecting the mass along the line of sight onto the lens plane:

$$\Sigma(\vec{r}\,') = \int \rho(\vec{r}\,') dz \tag{1.16}$$

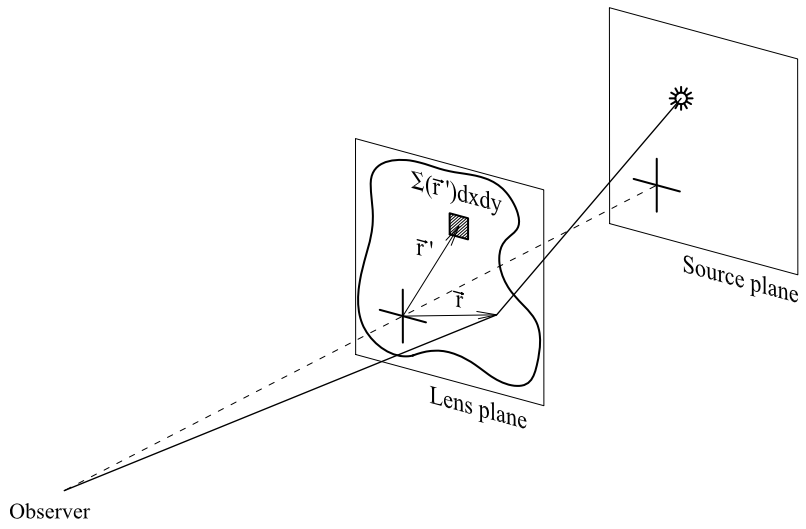

Figure 1.8: The mass distribution is projected onto the lens plane. Each deflecting point-mass m_i is replaced now by a surface mass element $\Sigma dx'dy'$

Bigger surface mass densities yield higher deflection angles. This leads to defining the *convergence* field κ by rescaling the surface mass density to dimensionless units:

$$\kappa(\vec{r}) = \frac{\Sigma(\vec{r})}{\Sigma_{cr}} \tag{1.17}$$

where Σ_{cr} is known as the *critical density*

[1] Not to be confused with any summation sign

$$\Sigma_{cr} = \frac{c^2}{4\pi G}\frac{D_s}{D_d D_{ds}} \tag{1.18}$$

There is a scalar potential ψ for the deflection angle, so that

$$\vec{\nabla}\psi = \vec{B} \tag{1.19}$$

This *effective lensing potential* results from the projection (as in eq. 1.16) of the gravitational potential onto the lens plane, conveniently scaled:

$$\psi(\vec{r}) = \frac{D_{LS}}{D_L D_S}\int \frac{2\phi}{c^2}dz \tag{1.20}$$

The relation between κ and ψ follows[1]:

$$\nabla^2\psi = 2\kappa(\vec{r}) \tag{1.21}$$

Our interest here in the lensing potential is because we can derive out of it a *Jacobian* of the mapping. Actually the lensing problem can be considered as a mapping between the source and the lens plane. If a (projected) source is much smaller than the angular size on which the physical properties of the lens change, the distortion on the image can be locally linearized, being described by the Jacobian matrix A:

$$A_{ij}(\vec{r}) = \left(\delta_{ij} - \frac{\partial^2\psi(\vec{r})}{\partial r_i \partial r_j}\right) \tag{1.22}$$

Following Narayan & Bartelmann 1996, we will rewrite now the Jacobian in a more useful fashion. For convenience, we introduce the abbreviation

$$\frac{\partial^2\psi}{\partial r_i \partial r_j} \equiv \psi_{ij} \tag{1.23}$$

Then, because of 1.21 ,

$$\kappa = \frac{1}{2}\left(\psi_{11} + \psi_{22}\right) \tag{1.24}$$

We introduce another definition whose purpose will become clear immediately. The two components γ_1, γ_2 of the *shear tensor* are

[1]Doing the line-of-sight projection of Poisson's equation for the gravitational potential and applying definitions 1.17 and 1.20

$$\gamma_1(\vec{r}) = \frac{1}{2}\left(\psi_{11} - \psi_{22}\right) \quad , \quad \gamma_2(\vec{r}) = \psi_{12} = \psi_{21} \tag{1.25}$$

With these definitions, the Jacobian matrix can be written:

$$A \;=\; (1-\kappa)\begin{pmatrix} 1 & 0 \\ 0 & 1 \end{pmatrix} - \begin{pmatrix} \gamma_1 & \gamma_2 \\ \gamma_2 & -\gamma_1 \end{pmatrix} \tag{1.26}$$

Alternatively we can write

$$A \;=\; (1-\kappa)\begin{pmatrix} 1 & 0 \\ 0 & 1 \end{pmatrix} - \gamma \begin{pmatrix} \cos 2\phi & \sin 2\phi \\ \sin 2\phi & -\cos 2\phi \end{pmatrix} \tag{1.27}$$

where γ, ϕ follow the definitions

$$\gamma_1 = \cos 2\phi \quad , \quad \gamma_2 = \sin 2\phi \tag{1.28}$$

so that $\gamma = \sqrt{\gamma_1^2 + \gamma_2^2}$. Now it is clear that the linearized Jacobian has two contributions, and the meaning of convergence and shear become evident (See figure 1.9):

- the convergence κ acting alone yields an isotropic increase in size of the source, with no change in shape,
- the shear γ describes a directional deformation, with no change in the area of the source, and ϕ describes its orientation.

Since, as said, the magnification is measured as the ratio between the image and source area, then

$$\mu = \frac{1}{\det A} = \frac{1}{[(1-\kappa)^2 - \gamma^2]} \tag{1.29}$$

As a summary: Once only angular distances are considered, the lensing problem is a mapping between source and image planes. *Establishing this mapping requires a physical mass distribution model of the lens* that allows to derive an effective lensing potential. Three combination of components of its associated Hessian matrix are of importance: one is called *convergence*, the others are the components of the *shear* tensor. They are position-dependent quantities describing the deformation field of the image by the lens.

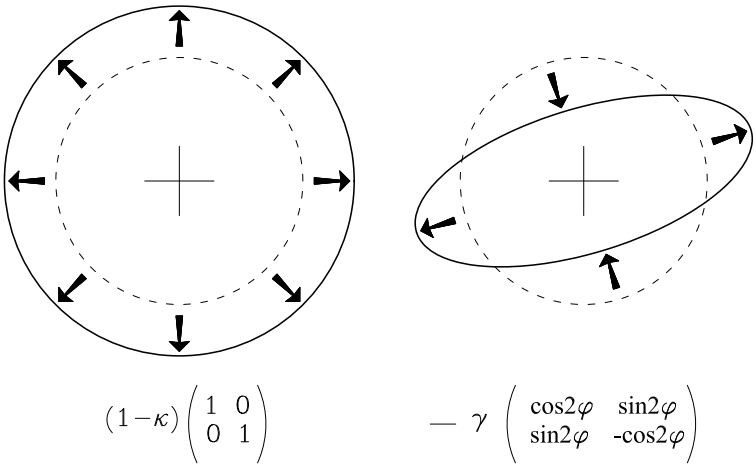

Figure 1.9: The two terms of the linearized Jacobian have a straightforward geometrical interpretation. The dashed circle represents a small, undistorted circular source.

1.5.5 Basic Lens Models

Thanks to Theorem XXXI in *Principia* (Newton 1687), the simplest model of a single mass point is still useful in some situations where the images are far from the center of the lens (Carroll & Ostlie 2007) and the mass distribution is not strongly asymmetrical. Moreover, axially symmetric lenses present a particularly simple form for the deflection angle, merely proportional to the mass enclosed within the circle whose radius is the impact parameter[1]. In normalized units, this is:

$$\alpha(x) = \frac{m(x)}{x} \tag{1.30}$$

However, more complex mass models are needed in the general case. We present an overview of the two most relevant mass distributions leading to lens modeling and the simplest way to deal with the presence of asymmetry in the distribution.

These models yield different deflection angles, and the key concept is that, as was mentioned, deflection angles obey a superposition principle we will use to create more realistic approaches, by simply adding the individual potentials or deflections, *provided*

[1]This results from a direct substitution of an axially symmetric surface density distribution into eq. 1.15. See 8.1.1 in Schneider & Ehlers & Falco 1992

that the same numerical scaling has been done on all the reduced expressions. Once we have an expression for the deflection angle $\vec{\alpha}$, the lens equation is simply 1.13)

$$\vec{y} = \vec{x} - \vec{\alpha} \tag{1.31}$$

1.5.5.1 The Many-points Lens

The deflection angle for a collection of points in the lens plane is given by eq. 1.14. Normalization (eq. 1.12) leads to the reduced form:

$$\vec{\alpha} = \sum_i m_i \frac{\vec{x} - \vec{x}_i}{|\vec{x} - \vec{x}_i|^2} \tag{1.32}$$

This deflection angle will play an important role for modeling microlensing by many point-like objects in extragalactic halos. Note the absence of axial symmetry.

1.5.5.2 The Uniform Sheet Model

A uniform sheet of surface density Σ_0 perpendicular to the line of sight, encloses the mass $\pi\xi^2\Sigma_0$ within a radius given by the impact parameter ξ of a chosen ray. Then, the deflection angle is given by means of 1.5 as

$$B = \frac{4\pi G\Sigma_0\xi}{c^2} \tag{1.33}$$

This is another axially symmetric system. With definitions 1.17, 1.18 and 1.12, this deflection angle is rewritten in dimensionless form as:

$$\vec{\alpha} = \kappa\vec{x} \tag{1.34}$$

The uniform sheet will be a useful approximation to a very small region within a soft potential. This will become clear in section 1.6 when we deal with modeling microlensing by halo stars around every quasar image.

1.5.5.3 The Isothermal Sphere (SIS)

The isothermal sphere model assumes that mass particles (i.e. stars or dust) follow a Maxwellian velocity distribution, such as that of ideal gas particles in thermal equilibrium. Such mass distribution is described by

$$\rho(r) = \frac{\sigma_v^2}{2\pi G}\frac{1}{r^2} \tag{1.35}$$

(Narayan & Bartelmann 1996) where σ_v is the one-dimensional velocity dispersion in thermal equilibrium. Integration along the line-of-sight with fixed impact parameter ξ yields the surface mass density already introduced in 1.15 for the case of an isothermal sphere:

$$\Sigma(\xi) = \frac{\sigma_v^2}{2G}\frac{1}{\xi} \tag{1.36}$$

which resembles the matter distribution in inner region of galaxies quite well for non-zero values of σ, since it yields the flat rotation curve of spiral galaxies.

We make the transition to dimensionless equations by defining

$$\xi_0 = 4\pi\,\frac{\sigma_v^2}{c^2}\frac{D_d D_{ds}}{D_s}\;, x = \frac{\xi}{\xi_0} \tag{1.37}$$

and, using 1.18, the surface mass density can be written as function of x as

$$\Sigma_0(x) = \frac{1}{2x}\Sigma_{cr} \tag{1.38}$$

Thus, the convergence field (eq. 1.17) is:

$$\kappa(x) = \frac{1}{2x} \tag{1.39}$$

The deflection angle follows from eq. 1.30[1]

$$\vec{\alpha} = \frac{\vec{x}}{|x|} \tag{1.40}$$

It is interesting to examine the behavior of the shear field produced by the isothermal sphere. From the lensing potential and definitions 1.25 it follows that

$$\gamma_1 = -\frac{1}{2}\frac{\cos 2\theta}{|x|}\;, \gamma_2 = -\frac{1}{2}\frac{\sin 2\theta}{|x|} \tag{1.41}$$

[1] Additional details in sec. 8.1.4 of Schneider & Ehlers & Falco 1992

where θ is the polar angle (and $|x|$ corresponds to the radial coordinate). This corresponds to a deformation of the images normal to the radius (Figure 1.10)

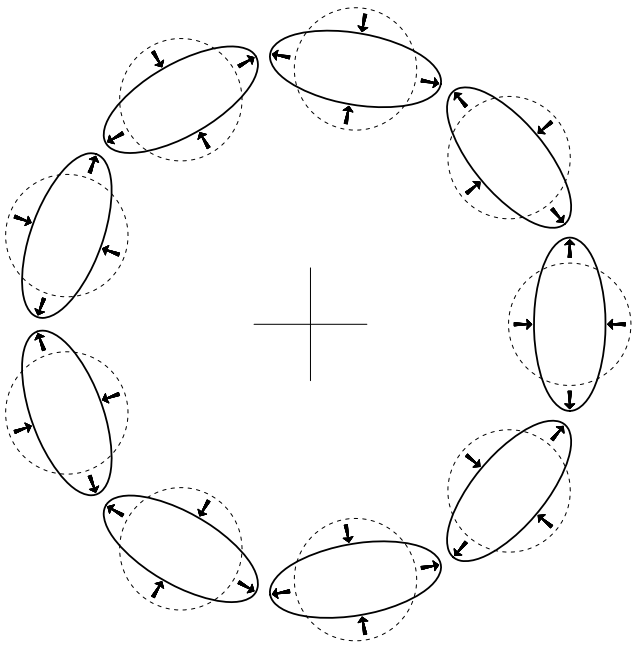

Figure 1.10: Visualization of the shear field introduced by a pure SIS model

Additionally, note that the shear modulus equals the convergence:

$$\gamma(x) = (\gamma_1^2 + \gamma_2^2)^{\frac{1}{2}} = \frac{1}{2x} = \kappa(x) \tag{1.42}$$

1.5.5.4 External Shear Field

We have so far seen only axially symmetric models. To account for an approximation to an asymmetric lens, we want to embed any of the preceding models into an external shear field that results in a uniform directional deformation that leaves magnification unaltered. This is equivalent to setting $\kappa = 0$ and constant values for γ_1, γ_2 in eq. 1.26. Since $\kappa = 0, \gamma_1, \gamma_2$ are related to the second differentials of the lensing potential by eqs. 1.24 and 1.25 , the effective lensing potential is easily recovered from eq. 1.23 as

$$\psi_\gamma = \frac{\gamma_1}{2}(x_1^2 - x_2^2) + \gamma_2 x_1 x_2 \tag{1.43}$$

This is a perturbing term to be added to the axially symmetric lens potential ψ_a, so that

$$\psi(x) = \psi(x)_a + \psi_\gamma \tag{1.44}$$

is the effective potential of the combined model. The deflection angle to be added to that of the axially symmetric lens, follows from eq. 1.19 and has the form

$$\vec{\alpha} = \begin{pmatrix} \gamma_1 & \gamma_2 \\ \gamma_2 & -\gamma_1 \end{pmatrix} \vec{x} \tag{1.45}$$

or, when adopting the shear eigenvectors reference frame,

$$\vec{\alpha} = \begin{pmatrix} \gamma & 0 \\ 0 & -\gamma \end{pmatrix} \vec{x} \tag{1.46}$$

It is important to remember that the shear field alone causes a directional deformation, but no change in the total area of the imaged source. When adding a shear field to any model, the expression for the convergence remains unaltered.

1.6 Modeling Extragalactic Microlensing

Extragalactic microlensing consists of two simultaneous gravitational lensing scenarios at different scales:

- The splitting of the source in several different images by the action of the lens galaxy, whose mass distribution requires a model, usually an ellipsoid or an isothermal sphere with additional external shear.
- The other scenario happens at each image position, where additional point-like sources embedded in the big scale field of the macro lens, produce additional magnification.

We focus now on the second, small-scaled lensing scenario, where the lens consists of a set of compact objects embedded on the galactic halo. The exact location of such micro lenses is unknown, but the higher their number, the higher the probability

of microlensing. Thus, a numerical simulation with different spatial distribution but the same number of micro-lenses, would allow us to extract the same magnification histogram as the real, unknown distribution. Such tool is a *Magnification Pattern* or *Magnification Map*:

1.6.1 Magnification Patterns

Convergence and Shear fields are dependent upon the position of the source plane as we have seen. Yet, the microlensing scenario involves a very small area of the projected galactic halo around one of the quasar images. This area typically ranges from hundreds to some thousands light-days (whereas the typical size of a galactic halo is bigger by two orders of magnitude) and so the convergence and shear from the lens galaxy are reasonably approximated by uniform quantities.

Thus, the deflection angle $\vec{\alpha}$ in the normalized lens equation $\vec{y} = \vec{x} - \vec{\alpha}$ results from the superposition of the deflection angles produced by

- a uniform sheet model (1.34) whose κ value is that of the macro lens at the image location, to account for the isotropic magnification at the location of the image caused by the macro lens potential.
- a shear field (1.45) whose value γ is given by that of the macro lens at the image location, to account for the shear deformation at the location of the image caused by the macro lens potential.
- a Many-Points lens(1.32), to account for the presence of star-sized compact objects.

$$\vec{y} = \vec{x} - \vec{\alpha}_{Uniform\,Sheet} - \vec{\alpha}_{External\,Shear} - \vec{\alpha}_{Many-Points} \tag{1.47}$$

$$\vec{y} = \vec{x} - \begin{pmatrix} \kappa & 0 \\ 0 & \kappa \end{pmatrix} \vec{x} - \begin{pmatrix} \gamma & 0 \\ 0 & -\gamma \end{pmatrix} \vec{x} - \sum_i m_i \frac{\vec{x} - \vec{x}_i}{|\vec{x} - \vec{x}_i|^2} \tag{1.48}$$

Note that we choose to work in the shear eigenvectors reference frame. How we get to know the numerical values of κ and γ at the image position, will become clear in the next section. For the moment, they are input values for the microlensing problem. The positions of the point lenses are chosen randomly.

This lens equation is used for the generation of the *Magnification Patterns*. Essentially, a magnification pattern is a numerical subdivision of a region of the image plane in surface elements, to which numerical values are assigned. The value assigned to each pixel corresponds to the magnification that pixel would suffer in case it were covered by the source.

The simplest example of magnification pattern is that of a single point-like lens (left image in 1.11), that simply shows how the microlensing magnification increases when the source is closer to the angular position of the lens, as expected (see discussion in sec. 1.5.2).

This is achieved numerically by the technique of *Inverse Ray Shooting*. The source plane is first subdivided in cells (or 'pixels' although no CCD imaging is involved here). Then, for a certain number of points x_i across the image plane, the corresponding source positions y_i are trivially given by the above lens equation. The total number of points y_i that fall into each source pixel is directly proportional to the total magnification of a source that were at that angular position and had the exact size and shape of the pixel.

Image 1.11 shows the magnification patterns for a single point-like lens, a two point-,like lens, and one example of the complicated patterns we use in this thesis to model the extragalactic halo microlensing scenario, with many-point lenses and κ, γ values provided by the macro lens halo model. The complicated lines of high magnification are called *caustics* in analogy with optics. If the lenses are geometrically perfect points, the caustics correspond to the mathematical locus of singular points of the transformation, where the Jacobian becomes zero and therefore the magnification diverges. Caustics location are the back-transformed location of *critical curves* at the image plane. An Einstein ring (see eq. 1.4 and section 1.5.1) is the simplest critical curve, whose corresponding caustic is a point at the angular position of the lens.

Raising the number of rays per pixel would ensure a higher accuracy, specially in those areas of the maps presenting more complexity, but this brute-force approach demands an huge amount of CPU power. All the magnification patterns used for this thesis rely on the *Inverse Polygon Mapping* optimized algorithm (Mediavilla et al. 2006), which is an improvement over Inverse Ray Shooting.

The Inverse Polygon Mapping algorithm essentially divides the lens plane in polygonal cells that are in principle much bigger than a single pixel. Instead of shooting a

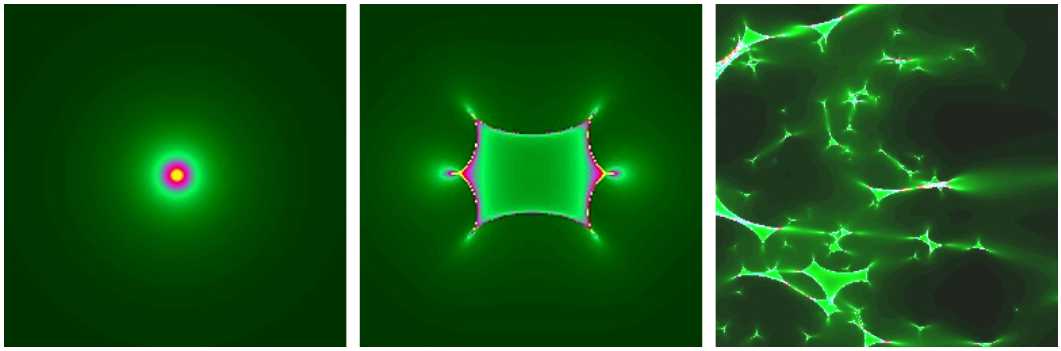

Figure 1.11: From left to right: magnification patterns of a single point lens, a two points lens and a more complicated halo microlensing scenario with multiple, scattered point lenses and uniform macro lens values of convergence and shear.

high number of rays, only a small number of points defining each cell are taken into account, mapping back each cell onto the source plane. Instead of counting the number of rays shooting each source pixel, the magnification at each source pixel is computed by adding each fraction of transformed cell surface that overlays with that pixel during the process of transformation of all cells (see Fig. 1.12).

For this process to be valid, the Jacobian of the transformation must remain nearly constant across each cell. The algorithm detects those cells that do not fulfill the appropriate conditions and subdivides them until critical curves are left outside cell borders. This results in a great performance increase, sparing CPU time in the less complex parts of the map.

Magnification patterns are useful to us because we will extract a histogram of magnification from each pattern. Although the real positions of halo stars are unknown, our histogram will match the real probability distribution function for the magnification, provided that we use the same number of stars and the same physical values of κ, γ at the image position. How we get to know that values is the subject of the next section.

1.6.2 The $SIS + \gamma^*$ macrolens fit

In order to obtain the κ and γ values at each image location, fitting a model of the lens galaxy to the observed data is required. The isothermal sphere alone, due to its axial symmetry, provides a poor model in many cases. The simplest improvement is the addition of an external shear field specified by γ_1^*, γ_2^*. The result is the $SIS + \gamma^*$

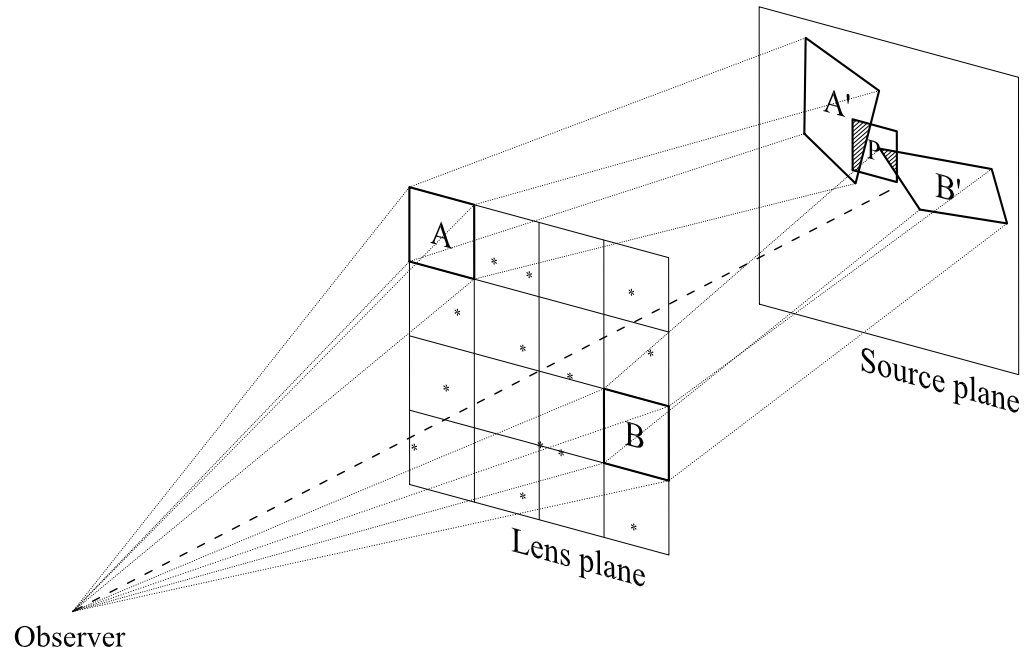

Figure 1.12: A schematic insight into Inverse Polygon Mapping. Two different cells A and B of the lens plane are mapped back onto A' and B' at the source plane, contributing with two area portions (shaded) to the magnification in pixel P

lens equation[1], whose deflection angle is obtained as a superposition of simpler models we have seen:

$$\vec{y} = \vec{x} - \vec{\alpha}_{Isothermal\,sphere} - \vec{\alpha}_{External\,Shear} \tag{1.49}$$

$$\vec{y} = \vec{x} - \frac{1}{|x|}\vec{x} - \begin{pmatrix} \gamma_1^* & \gamma_2^* \\ \gamma_2^* & -\gamma_1^* \end{pmatrix} \vec{x} \tag{1.50}$$

In this case, the shear direction is part of the model, therefore the need for two parameters γ_1^*, γ_2^*. There are more precise models (ie. we may use a Navarro-Frenk and White density profile (Navarro & Frenk & White 1996) or an ellipsoid) which may be useful for individual objects where somewhat detailed information about the

[1]The notation for the added shear field is γ_1^*, γ_2^*, not to be confused with the total shear value γ_1, γ_2 that results from the superposition of the external field with the one produce by the isothermal sphere $\gamma_1^{(SIS)}, \gamma_2^{(SIS)}$ at each point (see eq. 1.55).

lens galaxy can be directly detected. However, we deal with a heterogeneous quasar sample, where the lens galaxy is often poorly characterized. Thus, we are bound to use the simplest model available, yet producing good results with a minimum number of adjustable parameters.

The values κ and γ at each image position are obtained by a numerical fit. The observable quantities are:

- angular position of the ith image with respect to the center of the lens $\vec{\theta}^{(i)} = \theta_E \vec{x}^{(i)}$,
- integrated flux ratio between images $f^{(i)}/f^{(j)}$.

Equation 1.50 must hold for each of the images of a lensed quasar. Thus, for each image, we rewrite eq. 1.50 as the following two scalar equations:

$$\begin{aligned} \beta_1 - \theta_1^{(i)} + \frac{\theta_E}{\sqrt{\theta_1^2 + \theta_2^2}}\theta_1^{(i)} + \gamma_1^* \theta_1^{(i)} + \gamma_2^* \theta_2^{(i)} = 0 \\ \beta_2 - \theta_2^{(i)} + \frac{\theta_E}{\sqrt{\theta_1^2 + \theta_2^2}}\theta_2^{(i)} + \gamma_2^* \theta_1^{(i)} - \gamma_1^* \theta_2^{(i)} = 0 \end{aligned} \tag{1.51}$$

where the angular position of the source β_1, β_2, the Einstein angle θ_E and γ_1^*, γ_2^* are unknown.

For a system with two images, this means four equations and five unknowns $\beta_1, \beta_2, \theta_E, \gamma_1^*, \gamma_2^*$. The missing equation is obtained from the flux quotient, that equals the quotient of magnifications[1]:

$$\frac{f^{(i)}}{f^{(j)}} - \frac{\mu^{(i)}}{\mu^{(j)}} = 0 \tag{1.52}$$

Each μ is a function of the unknowns $\theta_E, \gamma_1, \gamma_2$ by means of eq. 1.29

$$\mu = \frac{1}{[(1-\kappa)^2 - \gamma^2]} \tag{1.53}$$

because κ is obtained from the SIS model (eq. 1.39), resulting in

[1] See 2.3 in Schneider & Ehlers & Falco 1992

$$\kappa = \frac{1}{2}\frac{\theta_E}{\sqrt{\theta_1^2 + \theta_2^2}} \tag{1.54}$$

and $\gamma = \sqrt{\gamma_1^2 + \gamma_2^2}$ is the total shear value at each image position, which results from the superposition of unknown external shear field and the shear from the SIS model:

$$(\gamma_1, \gamma_2) = (\gamma_1^{(SIS)} + \gamma_1^*, \gamma_2^{(SIS)} + \gamma_2^*) \tag{1.55}$$

The $\gamma^{(SIS)}$ components can be obtained from eq. 1.41, resulting in

$$\gamma_1^{(SIS)} = \frac{1}{2}\frac{\theta_1^2 - \theta_2^2}{(\theta_1^2 + \theta_2^2)^{3/2}}\theta_E \tag{1.56}$$

$$\gamma_2^{(SIS)} = -\frac{\theta_2\theta_1}{(\theta_1^2 + \theta_2^2)^{3/2}}\theta_E \tag{1.57}$$

To sum up, expressions 1.51 and 1.52 provide five equations for five unknowns, and the system can be numerically solved easily. For systems with more than two images, there are more equations than unknowns. Then, instead of solving theses quantities for zero, a Chi square is built out of them and the solution is found by a minimization algorithm. Alternatively, the software *Gravlens* (Keeton 2001) can be used to ease this task (e.g. to apply it on a large set of systems) with a rich variety of different lens models.

1.7 Conclusion

In this theory introduction we have tiptoed on the essential ingredients needed to understand this thesis.

We started with a brief overview of light deflection in ordinary mirages. Then, we have seen that Einstein created the theory and gave the mathematical expression for the analogous deflection by gravity, and Zwicky then predicted the detection of such *gravitational lensing* phenomenon at extragalactic distances, decades before it could be detected.

The typical scenario of gravitational lensing we are interested in, happens when light from a background quasar is split in several images by the mass of an intermediate galaxy. Changes in the quasar brightness are detected with different time delays at

each image, so that the individual light curves of the images are shifted with respect to each other. De-shifting and superposing that curves usually does not yield an exact match, and sometimes it is impossible, due to an additional phenomenon that introduces uncorrelated brightness changes between images. This phenomenon is additional lensing on a smaller scale due to the presence of matter substructure. Our models consider microlensing by compact objects present in the lens galaxy.

Gravitational lensing can be modeled as a transformation between an image and a source plane. We have seen the basic lens models (single and many-point lens, constant density sheet, isothermal sphere, external shear field) and how they can be combined to account for more complex situations. The linearity of the deflection angle with respect to the deflecting masses allow to combine these models easily. However, the total magnification probability for a combination of lenses is not a simple addition, therefore microlensing by halo stars must be statistically modeled.

For that statistical approach, we model microlensing by extragalactic halo stars, by combining a constant density sheet with a constant shear field, plus random sets of point lenses. This produces sets of differential magnification histograms that can be compared with the real microlensing measures, yielding the most likely value intervals for the physical parameters of interest. Prior to the numerical modeling of microlensing, some input values specific to each image position must be found by a numerical fit of the observed data to a macro lens model.

This introduction was specifically tailored towards the studies we will present in the forthcoming pages, but it is not intended to be a general description of gravitational lensing. Excellent, already classic references for that purpose are the short review by Narayan & Bartelmann 1996, which is recommended as a general introduction, and the canonical book by Schneider & Ehlers & Falco 1992 for a comprehensive description.

2

Aims of the Thesis

2.1 Motivation

We have done a review on the physics behind extragalactic gravitational microlensing, and the tools we make use of in this thesis. But, despite our understanding of the physical mechanisms, we still face a main impediment to use gravitational lenses as a tool in astrophysics and cosmology: the lens models are unconstrained. The isothermal sphere or any other model, are usually a useful fit to the soft varying, unknown lens mass distribution, where the image positions and flux quotients impose constraints to the model. However, the flux (and in lesser extent the position) of each image is affected both by the macro lens effect and microlensing simultaneously, being the amount corresponding to each of them unknown. Both scales of the lensing phenomenon operate simultaneously, in variable and unclear proportion.

One common approach to disentangle macro and micro magnification is based upon microlensing time variability (e.g. Morgan & Kochanek 2006). This approach faces two difficulties, namely

- the large timescales (up to several years) associated with quasar microlensing variability, and
- the lack of a baseline for no microlensing magnification: while exoplanets are detected by single microlensing events that produce and abnormal increase of bright for a short period of time of a star with well-known magnitude, we do not have an unlensed quasar image as a reference we can compare with.

The main goal of this thesis work is removing the first obstacle by doing a single-epoch statistical study of a set of quasars.

Our approach is based on defining a no-microlensing baseline by taking advantage of the fact that microlensing magnification decreases with the size of the source [1] and, although there is no chance of resolving quasar images with spatial resolution, we can distinguish spectral features from different sized regions of the quasar. In general terms, the continuum emission -strongly affected by microlensing- is supposed to originate at the very center of the quasar engine, with barely some light-days in diameter, whereas the spatially more extended emitting regions (weakly affected by microlensing) are thought to be the origin of the emission lines (we will see later how microlensing affects differently the wings and core components of the emission lines, making it also possible to separate the origin of both components).

Thus, it is our assumption that the core emission is only weakly affected by microlensing, which provides a useful baseline to measure microlensing magnification of other spectral features. Additionally, this approach to the problem allows us to get rid of the differential extintion issues as well. If we note by F_λ^0 the flux within a certain narrow wavelength interval centered in an emission line, once separated from the continuum emission, and we write F_λ for the flux of the underlying continuum, then we would expect the quantity

$$\frac{F_\lambda}{F_\lambda^0} \tag{2.1}$$

to be the same for all the images of a system. To quantify the presence of microlensing, we build this measure out of images A and B.

$$\frac{F_\lambda(A)/F_\lambda^0(A)}{F_\lambda(B)/F_\lambda^0(B)} \tag{2.2}$$

that will be called *differential microlensing magnification* hereafter. It is more usually expressed in magnitudes:

[1] When the Einstein radius of the lens is smaller than the solid angle covered by the source, many portions of source surface undergo little or no distortion. The contribution of the unlensed area will trend to lessen the magnification, since the later is equivalent to the ratio of the image and source areas, as seen in sections 1.5.2 and 1.5.4. There is no simple formula relating source size and magnification. One of the tasks in this thesis is achieving indirect estimates of several physical region sizes by means of Bayesian Montecarlo methods.

$$\Delta m = (m_\lambda(A) - m^0_\lambda(A)) - (m_\lambda(B) - m^0_\lambda(B)) \tag{2.3}$$

Note that this measure is free from extinction, since both the measured feature and the baseline core are equally affected, thus cancelling out.

The starting point for all our studies are the measured Δm. Note that Δm does not give information of the individual microlensing magnifications $m_\lambda(A)$ and $m_\lambda(B)$.

Our approach is one of a statistical nature. For that purpose we will use magnifications patterns. Since a magnification pattern is essentially a huge collection of magnifications associated with possibles hypothetical source positions (see sec. 1.11), we can extract different kinds of microlensing magnification histograms out of them. Specifically, we are interested in obtaining *differential magnification histograms* since we can only compare them with differential microlensing measures[1]. For that reason, this work starts by putting together a sample of quasar spectra available in the literature. Based on that set, the different works that make up this thesis, follow roughly the following steps:

- Designing and applying to the spectra a unified measuring procedure to separately obtain fluxes corresponding to the quantities of interest in each case: line cores, underlying continuum, line wings and blended iron line intervals.
- Computing the corresponding differential microlensing ratios out of the flux measures.
- Running the appropriate numerical simulations yielding differential magnification histograms within a range of possible values of the physical quantities of interest.
- Doing Bayesian comparison with the simulations, finding those parameter values with higher likelihood.

2.2 Scientific Goals

The first target quantity of our study was the continuum under the emission lines (chapter 4). The amount of microlensing for the region originating the continuum

[1]See Fig. 4.2 for a specific example, or a detailed exposition in the introductory section of Mediavilla et al. 2009

is strongly dependent on the density of deflectors in galactic halos. Comparison of the set of real measures with a set of predicted differential microlensing probability distributions will allow us to set an upper boundary to the mass fraction in MACHOs of galactic lens halos. The idea is extending the results of the M31 experiment (Alcock et al. 2000) to the extragalactic domain.

The goal of chapter 5 is somewhat different to those of the other chapters. Usually the data allow measuring differential microlensing for no more than three or four lines, then we build our measures for the idealized average lens out of a sample of quasars. But for this study we will use composite spectra from the Hubble Space Telescope and the 4.2 m William Herschell Telescope in La Palma, covering a very large wavelength region from the UV to the near IR, that will allow to measure many lines in a single object, SBS0909+532, thus mapping a wavelength dependence of the continuum microlensing signal.

Such wavelength dependence will be used to study the temperature profile of the accretion disk.

The target of chapter 6 is the Broad Line Region. We will use the broad emission wings as the comparison quantity to check against the narrow core emission baseline. Reverberation mapping studies suggest the origin of this emission in a intermediate region of fast orbiting clouds, up to several hundred light-days across, known as BLR (Broad Line Region). The wide range of projected velocities along the line of sight gives rise to Doppler broadening of the emission in broad wings around the central core wavelength for each line. Our goal will be studying whether microlensing affects this broad emission according to what is expected from the assumed size of the BLR.

The last of the objectives is to extend the study of microlensing to the iron emission lines. Although they are an important feature of quasar spectra, their origin is poorly understood. Iron has an extremely rich set of emission lines from many possible electronic transitions, that appear observationally blended as several regions at different locations in the spectra. We will examine microlensing on two UV iron bands, to arrive at an estimate of the size of the iron emitting region.

3

Database of Lensed Quasar Spectra

3.1 Introduction

Our first goal is to join a sample of lensed quasar spectra from the literature. For the sample to be useful for our scientific goals, we need two simultaneous spectra of at least two images of each same lens system. A wide range of redshifts, heterogeneous spectral coverage and instrumentation, makes comparisons among different objects from the literature a difficult task. Additionally, we had to apply a single, homogeneous continuum subtraction and flux measuring procedure all across the sample, for the results to be consistent.

In this chapter, we have arranged all continuum-subtracted spectra on a common wavelengths axis (Figures 3.1,3.2,3.3,3.4). Every frame represents a superposition of two spectra corresponding to two different lensed images of the same quasar. The spectrum of the faintest image (red colour) has been arbitrarily scaled so that it follows closely the spectrum of the brightest image (black line). This kind of representation allows a quick overview of the features and possible utility of the data, e.g. where microlensing may take place because some line profiles do not coincide.

Most spectra contain both the CIII] λ1909 and MgII λ2798 lines, but some of them cover the near UV region and, in one case, H_α λ6563 has been observed. A table has been included with the lens redshift, the de-reddened spectral coverage, acquisition date, and a reference to the original papers where the spectra appear. The authors

provide the specific details on each data acquisition, reduction and even their own flux quotient measures. When spectra have been combined but the acquisition dates differed only in a few days, it is the last date what figures in the table. When the data were acquired along months or even years and then combined, no date has been shown in the table. It must be taken into consideration that typical microlensing variability timescales are in the range of hundreds days (Carroll & Ostlie 2007).

3.2 Visual Reference to the Database

	Z	Observation Date	Wavelength	Reference
HE 0047-1756 A,B	1.67	2002 Sep 4	(1461-2547)	Wisotzki et al. 2004
HE 0435-1223 A,B	1.69	2008 Ene 12	(1210-3030)	Unpub. (Motta, V.)
HE 0435-1223 B,D	1.69	2004 Oct 12	(1638-2996)	Unpub. (Motta, V.)
HE 0435-1223 A,B	1.69	2002 Sep 7	(1413-2529)	Wisotzki et al. 2003
HE 0435-1223 C,D	1.69	2002 Sep 7	(1413-2529)	Wisotzki et al. 2003
HE 0512-3329 A,B	1.58	2001 Aug 13	(0775-2171)	Wucknitz et al. 2003
SDSS 0806+2006 A,B	1.54	2005 Abr 12	(1575-3504)	Inada et al. 2006
HE 2149-2745 A,B	2.03	2000 Nov 19	(1430-3174)	Unpub. (Motta, V.)
SDSS J0924+0219 A,B	1.52	2005 Feb 1	(1783-3170)	Eigenbrod et al. 2006
FBQ 0951+2635 A,B	1.24	1997 Feb 14	(1786-4018)	Schechter et al. 1998
QSO 0957+561 A,B	1.41	2008 Ene 13	(1330-3380)	Motta et al. 2012
QSO 0957+561 A,B	1.41	(several)	(0913-4149)	Goicoechea et al. 2005
SDSS J1001+5027 A,B	1.84	2003 Nov 20	(1409-3136)	Oguri et al. 2005
SDSS J1004+4112 A,B	1.73	2004 Jan 19	(1318-2928)	Richards et al. 2004
SDSS J1004+4112 C,D	1.73	2004 Jan 19	(1318-2928)	Richards et al. 2004
QSO 1017-207 A,B	2.55	1996 Oct 28	(1016-1975)	Surdej et al. 1997
HE 1104-1805 A,B	2.32	2008 Abr 7	(1310-2909)	Motta et al. 2012
HE 1104-1805 A,B	2.32	1993 May 11	(1211-2846)	Wisotzki et al. 1995
PG 1115+080 A,B	1.72	1996 Jan 24	(0846-1213)	Popovic et al. 2005
SDSS J1206+4332 A,B	1.79	2004 Jun 21	(1362-3048)	Oguri et al. 2005
SDSS J1353+1138 A,B	1.63	2005 Abr 12	(1521-3385)	Inada et al. 2006
WFI J2033-4723 B,C	1.66	2008 Abr 14	(1620-3625)	Unpub. (Motta, V.)
WFI J2033-4723 A1,A2	1.66	2003 Sep 15	(1429-3008)	Morgan et al. 2004
WFI J2033-4723 B,C	1.66	2003 Sep 15	(1429-3008)	Morgan et al. 2004
SBS 1520+530 A,B	1.86	1996 Jun 12	(1331-2452)	Chavushian et al. 1997
SBS 0909+532 A,B	1.38	(several)	(0957-2378)	Mediavilla et al. 2005

Table 3.1: General data for the spectral database

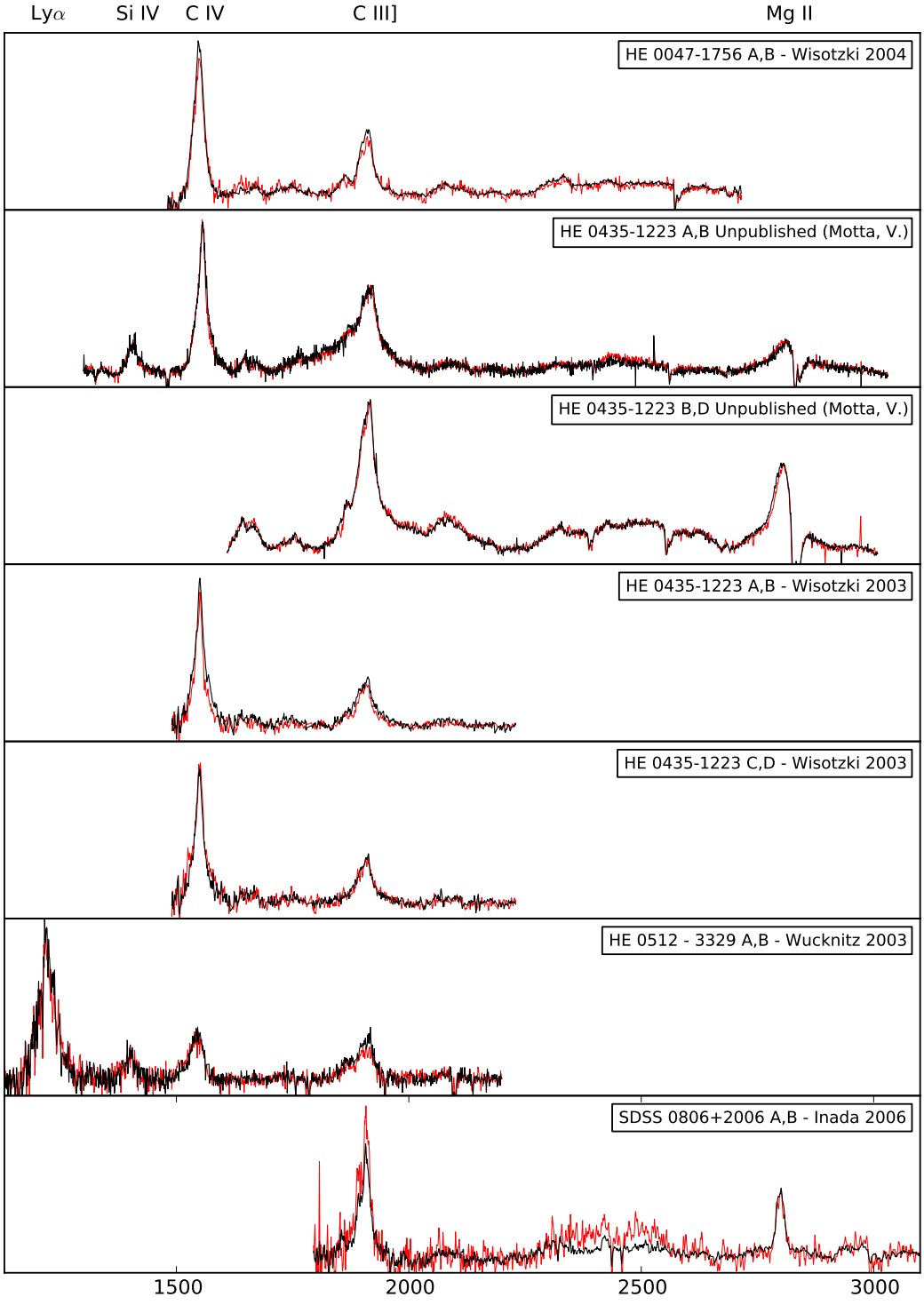

Figure 3.1: Superposition of scaled spectrum pairs

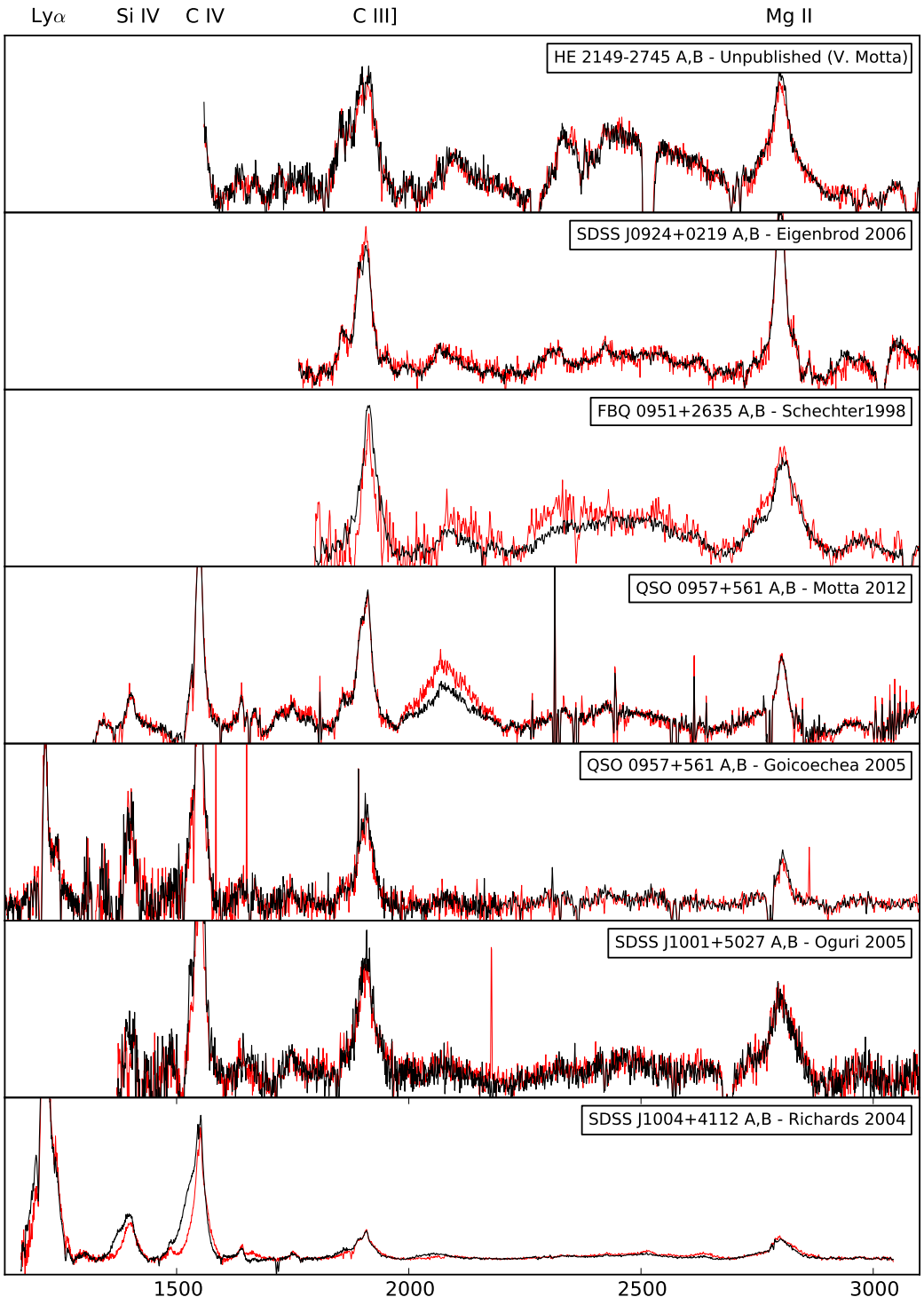

Figure 3.2: Superposition of scaled spectrum pairs

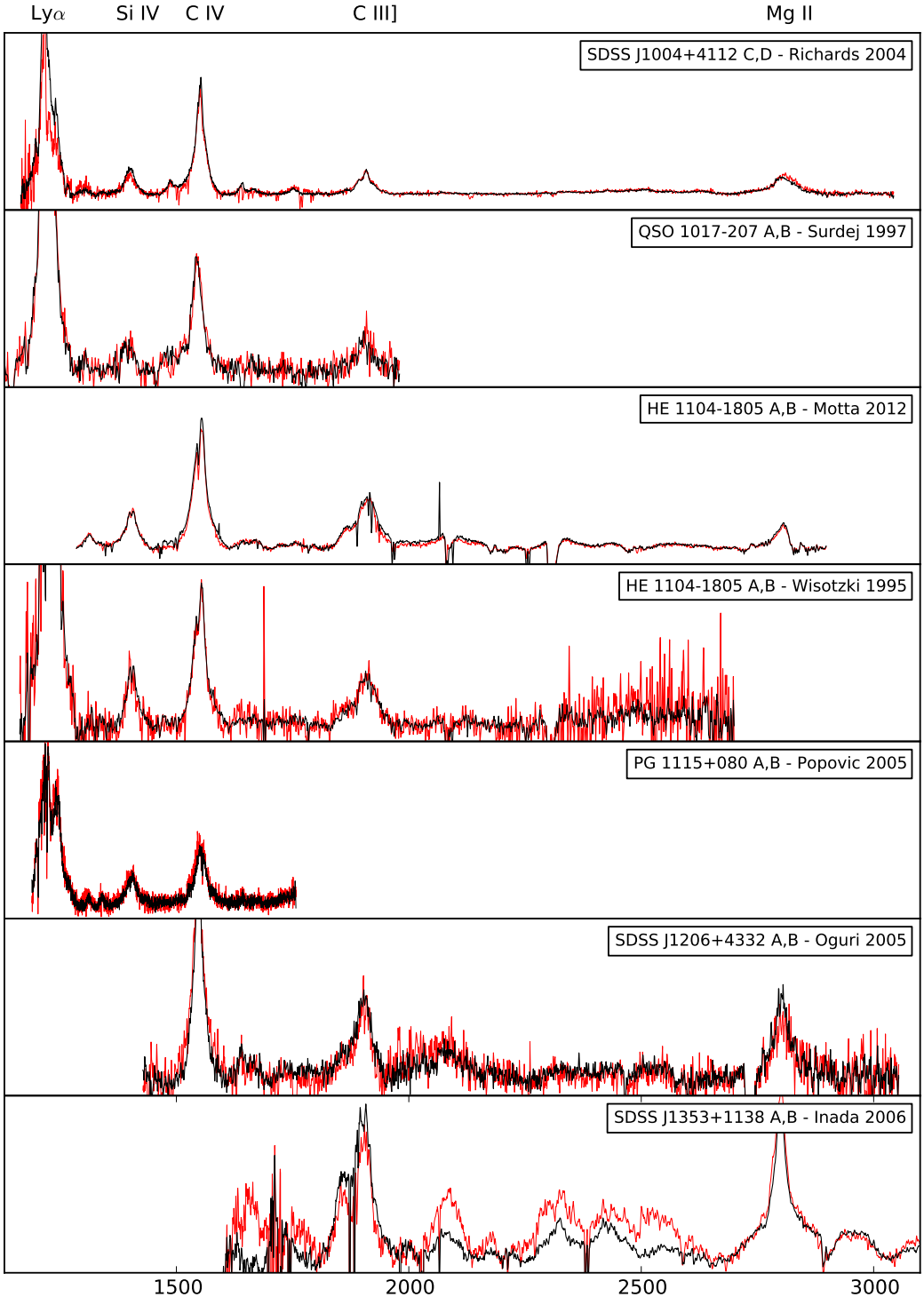

Figure 3.3: Superposition of scaled spectrum pairs

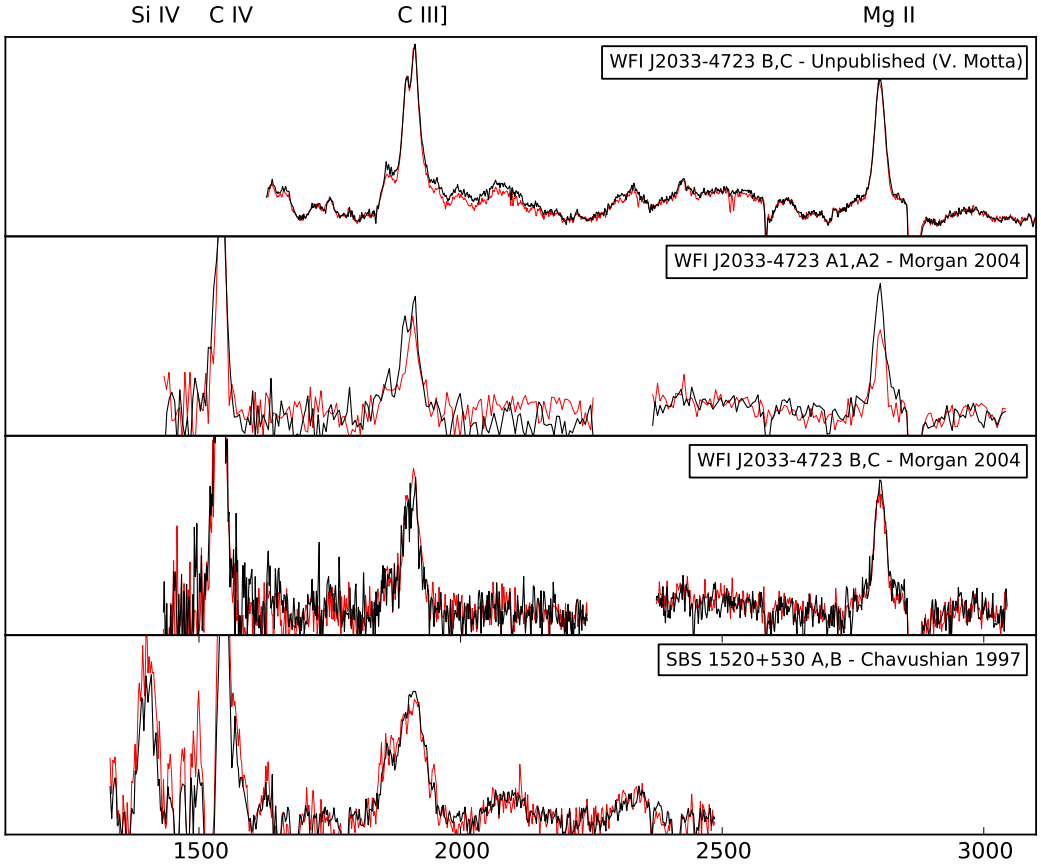

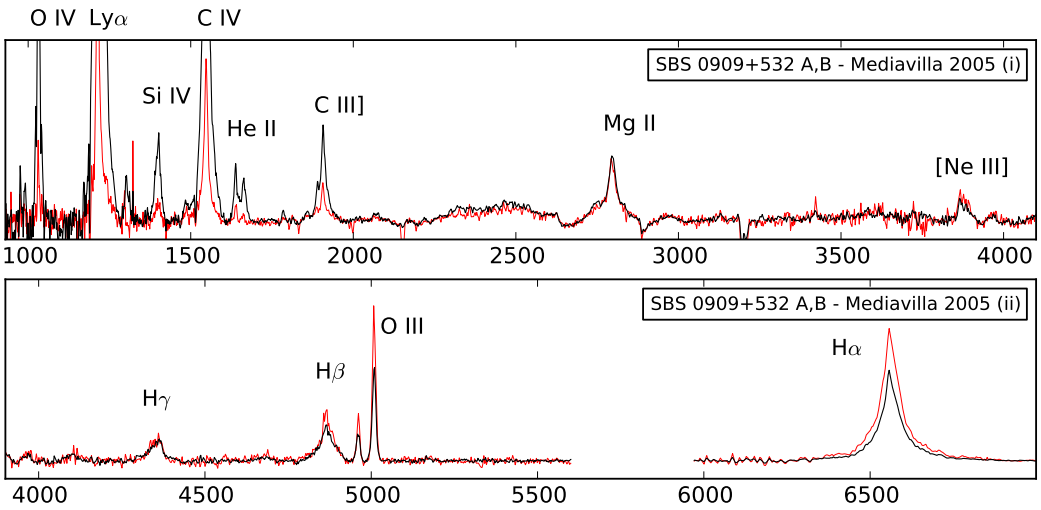

Figure 3.4: Superposition of scaled spectrum pairs

Ly_α	$\lambda 1216$
Si IV	$\lambda 1400$
C IV	$\lambda 1549$
CIII]	$\lambda 1909$
MgII	$\lambda 2798$
H beta	$\lambda 4861$
[O III]	$\lambda\lambda 4959, 5007$
H_α	$\lambda 6563$

Table 3.2: Most common emission lines.

4

Microlensing-based Estimate of the Mass Fraction in Compact Object in Lens Galaxies

4.1 Introduction

This is the first of the four paper series that make up this thesis. Its main purpose was the quantification of the typical quantity of compact objects in extragalactic halos. The famous search for such objects in the Milky Way halo (Alcock et al. 2000) was based on the detection of single events via light curves with typical times in the order of several days.

This was possible, since the light curve caused by the alignment of a single point-like lens with a background star is simple (see Figure 4.1). However, several obstacles make this approach impossible for the study of extragalactic microlensing:

- Lack of a baseline for no magnification, needed to detect and quantify microlensing.
- Larger timescales for microlensing variability.
- Unlike the deflection angle, the magnification of a source by a star field is different from the sum of its components, therefore high optical depth microlensing should be statistically modeled.

4. MICROLENSING-BASED ESTIMATE OF THE MASS FRACTION IN COMPACT OBJECT IN LENS GALAXIES

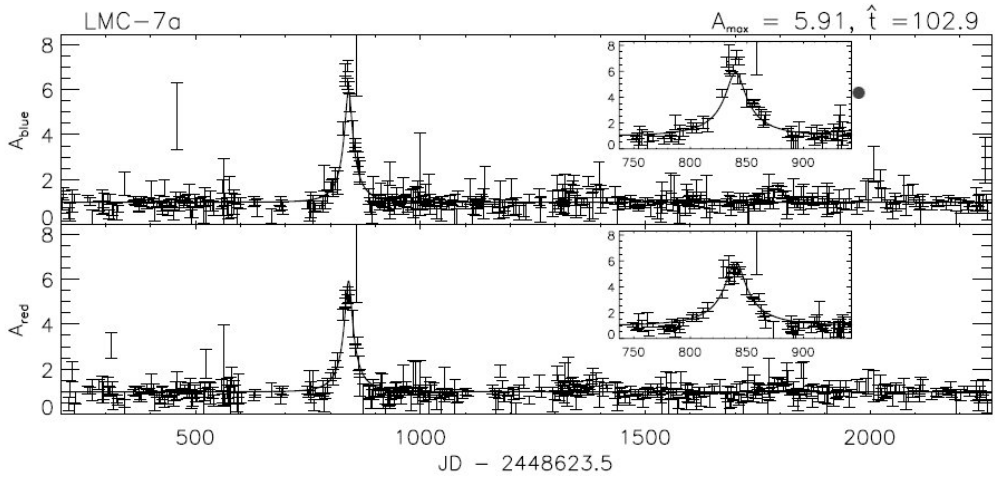

Figure 4.1: Light curves from single microlensing events of LMC stars by Milky Way MACHOs in Alcock et al. 2000

We use the following approach: Given a big enough sample of differential microlensing measures, the shape of the associated histogram should be related to the mean mass fraction in MACHOs of galactic halos, e.g halos with a low content in compact objects are likely to yield mostly zero microlensing measures, resulting in a histogram highly concentrated around zero. Conversely, a high content in MACHOs produces a wide spread histogram as a result of all possible microlensing measures at high optical depth.

We built the histogram of differential microlensing measures out of 29 lensed pairs from 20 lenses. The target quantity that was compared with the emission line fluxes (which are considered to be not affected by microlensing, as explained in chapter 2), was the continuum flux underlying each line. Different emission line measurements were averaged to yield a single differential microlensing value for each pair.

The histogram for such microlensing values is strongly concentrated below 0.6 mag, pointing out that the additional magnification due to microlensing by halo stars is generally low, and so the content in MACHOs of galactic halos.

To back up this conclusion with numerical results, we wanted to compare this histogram with a set of computer-generated histograms for different compact objects mass fractions. We extracted them from a set of magnification maps, each one reproducing the physical conditions at the image locations given by the isothermal sphere model

with external shear, and a range of different values of the mass fraction in MACHOs and source sizes. The process is illustrated in Figure 4.2.

The comparison was done via a maximum likelihood analysis. The result was a mass fraction of MACHOs under 10%, at 90% confidence level. This was the first time an insight into the MACHO contents of extragalactic halos was done, ruling out the possibility of dark matter being composed of dark compact objects. In fact, our result is compatible with no content in MACHOs at all, and the small amount of differential microlensing found may arise from normal stellar populations.

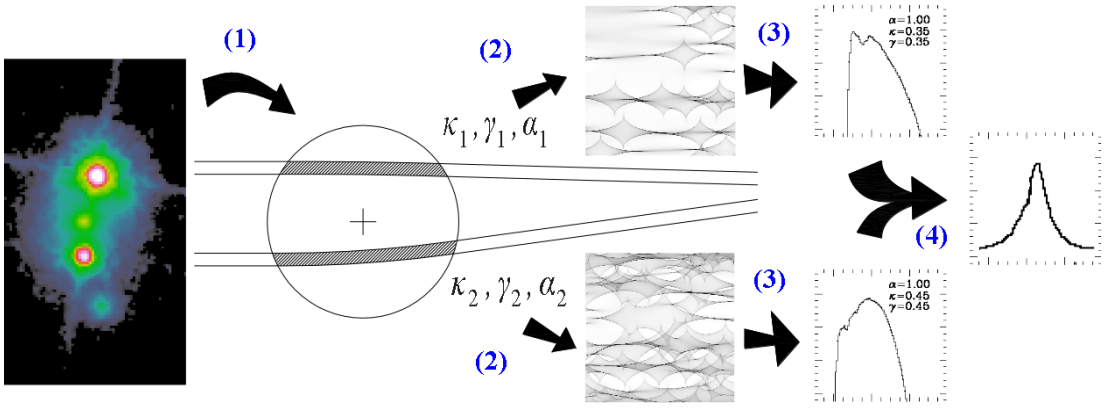

Figure 4.2: An illustration of the process leading to the simulated histograms. (1) Adjusting the image positions and integrated flux quotients to the SIS model yields the projected kappa at image position and shear value. (2) These and the mass fraction in randomly distributed compact objects α are the inputs for the generation of the magnification maps. (3) Microlensing magnification histograms are extracted from each map (4) Convolution of the histograms results in the differential magnification histogram

4. MICROLENSING-BASED ESTIMATE OF THE MASS FRACTION IN COMPACT OBJECT IN LENS GALAXIES

4.2 Mediavilla et al. 2009

4. MICROLENSING-BASED ESTIMATE OF THE MASS FRACTION IN COMPACT OBJECT IN LENS GALAXIES

The Astrophysical Journal, 706:1451–1462, 2009 December 1 doi:10.1088/0004-637X/706/2/1451

MICROLENSING-BASED ESTIMATE OF THE MASS FRACTION IN COMPACT OBJECTS IN LENS GALAXIES

E. Mediavilla[1,2], J. A. Muñoz[3], E. Falco[4], V. Motta[5], E. Guerras[1], H. Canovas[1], C. Jean[2], A. Oscoz[1], and A. M. Mosquera[2]

[1] Instituto de Astrofísica de Canarias, Vía Láctea S/N, 38200-La Laguna, Tenerife, Spain
[2] Departamento de Astrofísica, Universidad de La Laguna, E-38205 La Laguna, Tenerife, Spain
[3] Departamento de Astronomía y Astrofísica, Universidad de Valencia, 46100-Burjassot, Valencia, Spain
[4] Smithsonian Astrophysical Observatory, FLWO, P.O. Box, 97, Amado, AZ 85645, USA
[5] Departamento de Fisica y Astronomia, Facultad de Ciencias, Universidad de Valparaiso, Avda. Gran Bretaña 1111, Valparaiso, Chile
Received 2008 April 15; accepted 2009 October 16; published 2009 November 12

ABSTRACT

We estimate the fraction of mass that is composed of compact objects in gravitational lens galaxies. This study is based on microlensing measurements (obtained from the literature) of a sample of 29 quasar image pairs seen through 20 lens galaxies. We determine the baseline for no microlensing magnification between two images from the ratios of emission line fluxes. Relative to this baseline, the ratio between the continua of the two images gives the difference in microlensing magnification. The histogram of observed microlensing events peaks close to no magnification and is concentrated below 0.6 mag, although two events of high magnification, $\Delta m \sim 1.5$, are also present. We study the likelihood of the microlensing measurements using frequency distributions obtained from simulated microlensing magnification maps for different values of the fraction of mass in compact objects, α. The concentration of microlensing measurements close to $\Delta m \sim 0$ can be explained only by simulations corresponding to very low values of α (10% or less). A maximum likelihood test yields $\alpha = 0.05^{+0.09}_{-0.03}$ (90% confidence interval) for a quasar continuum source of intrinsic size $r_{s_0} \sim 2.6 \times 10^{15}$ cm. This estimate is valid in the 0.1–10 $M_\odot$ range of microlens masses. We study the dependence of the estimate of α with r_{s_0}, and find that $\alpha \lesssim 0.1$ for $r_{s_0} \lesssim 1.3 \times 10^{16}$ cm. High values of α are possible only for source sizes much larger than commonly expected ($r_{s_0} \gg 2.6 \times 10^{16}$ cm). Regarding the current controversy about Milky Way/LMC and M31 microlensing studies, our work supports the hypothesis of a very low content in MACHOS (Massive Compact Halo Objects). In fact, according to our study, quasar microlensing probably arises from the normal star populations of lens galaxies and there is no statistical evidence for MACHOS in the dark halos.

Key words: dark matter – galaxies: halos – gravitational lensing

1. INTRODUCTION

The composition of matter in the halos of galaxies is a central problem in astrophysics. During the last 10 years, several observational projects have used gravitational microlensing (Paczynski 1986) to probe the properties of the halos of the Milky Way (MACHO, Alcock et al. 2000; EROS, Tisserand et al. 2007) and M31 (POINT-AGAPE, Calchi Novati et al. 2005; MEGA, de Jong et al. 2006). These experiments are based on the detection of magnification in the light curve of a source induced by an isolated point-like (or binary) object passing near the observer's line of sight. From the successful detection of a number of microlensing events these collaborations have estimated the fraction of the halo mass that is composed of lensing objects, α. However, the reported results disagree. For the Milky Way's halo the measurements of the MACHO collaboration (Alcock et al. 2000) correspond to a halo fraction of $0.08 < \alpha < 0.50$ while EROS (Tisserand et al. 2007) obtains $\alpha < 0.08$. On the other hand, re-analysis of publicly available MACHO light curves (Belokurov et al. 2004) leads to results similar to those reported by EROS (however, see also the counter-report by Griest & Thomas 2005). For M31 the AGAPE (Calchi Novati et al. 2005) collaboration finds a halo fraction in the range $0.2 < \alpha < 0.9$, while MEGA (de Jong et al. 2006) finds a limit of $\alpha < 0.3$.

The method applied to the Milky Way and M31 can be extended to the extragalactic domain by observing the microlensing induced by compact objects in the lens galaxy halo in images of multiply imaged quasars (quasar microlensing; Chang & Refsdal 1979, see also the review by Wambsganss 2006). Interpreting the light curves of QSO 2237+0305, Webster et al. (1991) suggest that the monitoring of microlensing variability can provide a measure of the optical depth in compact objects and in the smooth mass distribution. Lewis & Irwin (1996) proposed a statistical approach to the determination of the mass density in compact objects based on the comparison between the observed and simulated magnification probability distributions. Microlensing can also be measured from a single-epoch snapshot of the anomalous flux ratios induced by this effect between the images of a lensed quasar (Witt et al. 1995; see also Schechter & Wambsganss 2002). Schechter & Wambsganss (2004) explore the practical application of this idea by using a sample of 11 systems with measured flux anomalies. Other quasar microlensing studies of interest for the present study are aimed at the determination of accretion disk sizes (e.g., the studies based in relatively large samples by Poindexter et al. 2007, Morgan et al. 2007 and references therein).

In practice, the study of extragalactic microlensing meets significant obstacles, in particular (e.g., Kochanek 2004) larger timescales for microlensing variability and lack of a baseline for no magnification needed to detect and to quantify microlensing (see, however, the time variability based studies of several individual systems in Morgan et al. 2008 and references therein). In addition, microlensing by an isolated object is not a valid approximation. Microlensing at high optical depth should be modeled (e.g., by simulating magnification maps; see Schneider et al. 1992).

Table 1
Microlensing Data

Object	Image Pair	$\langle\Delta m\rangle$[a]	$\Delta m^{\rm cont,lines}$ (cont/lines)[b]	Lyα (cont/line)[c]	[Si IV]/[O IV] (cont/line)[c]	C IV (cont/line)[c]	[C III] (cont/line)[c]	Mg II (cont/line)[c]	[O III] (cont/line)[c]
HE 0047−1756[d]	$B-A$	−0.19	1.17/1.36	···	···	···	···	···	···
HE 0435−1223[e]	$B-A$	−0.24	···	···	···	···	···	···	···
	$C-A$	−0.30	···	···	···	···	···	···	···
	$D-A$	0.09	···	···	···	···	···	···	···
HE 0512−3329[f]	$B-A$	-0.40 ± 0.16	···	···	···	···	···	···	···
SDSS 0806+2006[g]	$B-A$	-0.47 ± 0.20	···	···	···	···	0.06/0.33	0.06/0.72	···
SBS 0909+532[h]	$B-A$	-0.60 ± 0.15	···	···	···	···	···	···	···
SDSS J0924+0219[i]	$B-A$	0.00	···	···	···	···	···	···	···
FBQ 0951+2635[j]	$B-A$	-0.69 ± 0.35	···	···	···	···	0.08/1.12	0.13/0.46	···
QSO 0957+561[k]	$B-A$	−0.30	−0.30/0.0	···	···	···	···	···	···
SDSS J1001+5027[l]	$B-A$	0.23 ± 0.04	···	···	···	0.63/0.35	0.38/0.19	···	···
SDSS J1004+4112[m]	$B-A$	0.00	0.50/0.50	···	···	···	···	···	···
	$C-A$	0.45	0.64/0.19	···	···	···	···	···	···
QSO 1017−207[n]	$B-A$	-0.26 ± 0.11	···	−2.21/−2.08	−2.24/−2.06	−2.24/−1.41	−2.15/−1.76	···	···
HE 1104−1805[o]	$B-A$	0.60 ± 0.03	···	···	···	···	1.75/1.12	1.68/1.12	···
PG 1115+080[p]	$A2-A1$	−0.65	−0.65/0.0	···	···	···	···	···	···
RXS J1131−1231[q]	$A-B$	1.39	···	···	···	···	···	···	0.65/−0.74
	$C-B$	1.58	···	···	···	···	···	···	1.27/−0.31
SDSS J1206+4332[r]	$A-B$	-0.56 ± 0.21	···	···	···	···	0.32/1.08	0.54/0.89	···
SDSS J1353+1138[s]	$A-B$	0.00	···	···	···	···	···	···	···
HE 1413+117[t]	$B-A$	0.00 ± 0.04	···	···	0.23/0.19	0.20/0.23	···	···	···
	$C-A$	-0.25 ± 0.10	···	···	−0.03/0.27	−0.07/0.27	···	···	···
	$D-A$	-0.75 ± 0.08	···	···	0.2/−1.07	0.22/−0.85	···	···	···
B J1422+231[u]	$A-B$	0.16	···	0.27/0.11	···	···	···	···	···
	$C-B$	0.02	···	0.75/0.77	···	···	···	···	···
	$D-B$	−0.08	···	3.92/4.00	···	···	···	···	···
SBS 1520+530[v]	$B-A$	-0.39 ± 0.07	···	···	···	−0.04/0.27	0.08/0.54	···	···
WFI J2033−4723[w]	$B-C$	−0.50	···	···	···	−0.09/0.41	···	···	···
	$A2-A1$	0.00	···	···	···	0.32/0.32	···	···	···

Notes.
[a] Average microlensing magnification, $\langle\Delta m\rangle = \langle\Delta m^{\rm cont} - \Delta m^{\rm line}\rangle$.
[b] Magnitude differences between images in the continuum and in the line emission, respectively (when a global value for an spectral region including several lines is given).
[c] Magnitude differences between images in the continuum and in the line emission, respectively (when an individual value for one or more lines is available).
[d] Wisotzki et al. (2004; line flux ratio given by the authors; continuum flux ratio estimated from Figure 3).
[e] Wisotzki et al. (2003; microlensing magnifications taken from Table 3).
[f] Wucknitz et al. (2003; microlensing magnification estimated from Figure 3).
[g] Inada et al. (2006; flux ratios computed from electronically digitized spectra).
[h] Mediavilla et al. (2005; microlensing magnification estimated from Figure 7).
[i] Eigenbrod et al. (2006; see the text).
[j] Schechter et al. (1998; flux ratios computed from electronically digitized spectra).
[k] Goicoechea et al. (2005; line flux ratio given by the authors; continuum ratio estimated from Figure 1).
[l] Oguri et al. (2005; flux ratios computed from electronically digitized spectra).
[m] Gómez-Álvarez et al. (2006; flux ratios estimated from Figures 3 and 4).
[n] Surdej et al. (1997; flux ratios computed from electronically available spectra).
[o] Wisotzki et al. (1993; line flux ratio given by the authors; continuum flux ratios estimated from Figure 3).
[p] Popović & Chartas (2005; line flux ratio given by the authors; continuum flux ratio estimated from Figure 9).
[q] Sluse et al. (2007; flux ratios taken from Table 5).
[r] Oguri et al. (2005; flux ratios computed from electronically digitized spectra).
[s] Inada et al. (2006; see the text).
[t] Popović & Chartas (2005; flux ratios computed from electronically available spectra).
[u] Impey et al. (1996; flux ratios taken from Table 3).
[v] Chavushyan et al. (1997; flux ratios computed from electronically digitized spectra).
[w] Morgan et al. (2004; flux ratios estimated from Figure 9).

We avoid these obstacles by setting the baseline of no microlensing magnification using the narrow emission lines (NELs) in the spectra of lensed quasar images (Schechter & Wambsganss 2004 follow a similar approach but using theoretical models to define the baseline). It is generally expected that the regions where NELs originate are very large (compared with the continuum source) and are not affected by microlensing (this assumption can also be adopted, to some extent, for low ionization broad emission lines; Kaspi et al. 2000; Abajas et al. 2002). If we define the baseline from emission lines measured in the same wavelength regions as the continua affected by microlensing, we can also remove the extinction and isolate the microlensing effects.

"Intrinsic" flux ratios between the images in the absence of microlensing can be determined from the observation of the mid-infrared and radio-emitting regions of quasars that should

Table 2
Comparison Between Emission Line and Mid-IR Flux Ratios

Object	Image Pair	$\Delta m^{\rm lines}$	$\Delta m^{\rm mid-IR}$
SDSS J1004+4112[a]	$B-A$	0.50	0.30
	$C-A$	0.19	0.50
HE 1104−1805[b]	$B-A$	1.12	1.13 ± 0.06
PG 1115+080[c]	$A2-A1$	0.0	0.08 ± 0.06
HE 1413+117[d]	$B-A$	0.21 ± 0.02	0.19 ± 0.07
	$C-A$	0.27 ± 0.00	0.36 ± 0.07
	$D-A$	0.96 ± 0.11	0.99 ± 0.06
B J1422+231[c]	$A-B$	0.11	0.18 ± 0.05
	$C-B$	0.77	0.61 ± 0.06

Notes.
[a] Mid-IR data from Ross et al. (2009).
[b] Mid-IR data from Poindexter et al. (2007).
[c] Mid-IR data from Chiba et al. (2005).
[d] Mid-IR data from MacLeod et al. (2009).

also be large enough to average out the effects of microlensing (see Kochanek 2004 and references therein). However, the extinction at mid-infrared and radio wavelengths is lower than the extinction at the wavelengths in which microlensing is usually detected and measured (optical, near-infrared, and X-ray). Consequently, the difference between the mid-infrared (radio) and the optical (X-ray or near-infrared) continuum fluxes will include not only the effects of microlensing but also the effects of extinction. In addition, note that the availability of data at optical wavelengths is considerably greater than at other wavelengths.

Thus, we will use the NEL and continuum flux ratios among the different images of a lensed QSO to estimate the difference of microlensing magnification between the images at a given epoch with certain restrictions that we detail in the following paragraphs.

The flux (in magnitudes) of an emission line observed at wavelength λ of image i of a multiply imaged quasar is equal to the flux of the source, $m_0^{\rm lin}\left(\frac{\lambda}{1+z_s}\right)$, magnified by the lens galaxy (with a Φ_i magnification factor; $\mu_i = -2.5\log\Phi_i$) and corrected by the extinction of this image caused by the lens galaxy, $A_i\left(\frac{\lambda}{1+z_l}\right)$ (see, e.g., Muñoz et al. 2004),

$$m_i^{\rm lin}(\lambda) = m_0^{\rm lin}\left(\frac{\lambda}{1+z_s}\right) + \mu_i + A_i\left(\frac{\lambda}{1+z_l}\right), \quad (1)$$

where z_s and z_l are the redshifts of the source and the lens, respectively.

In the case of the continuum emission, we must also take into account the intrinsic variability of the source combined with the delay in the arrival of the signal, which is different for each image, Δt_i, and the microlensing magnification, which depends on wavelength and time (with a $\phi_i\left[\frac{\lambda}{1+z_l}, t\right]$ magnification factor; $\Delta\mu_i = -2.5\log\phi_i$),

$$m_i^{\rm con}(\lambda,t) = m_0^{\rm con}\left(\frac{\lambda}{1+z_s}, t-\Delta t_i\right) + \mu_i + A_i\left(\frac{\lambda}{1+z_l}\right) + \Delta\mu_i\left(\frac{\lambda}{1+z_l}, t\right). \quad (2)$$

Thus, the difference between continuum and line fluxes cancels the terms corresponding to intrinsic magnification and extinction ($\mu_i + A_i$):

$$m_i^{\rm con}(\lambda,t) - m_i^{\rm lin}(\lambda) = m_0^{\rm con}\left(\frac{\lambda}{1+z_s}, t-\Delta t_i\right) - m_0^{\rm lin}\left(\frac{\lambda}{1+z_s}\right) + \Delta\mu_i\left(\frac{\lambda}{1+z_l}, t\right). \quad (3)$$

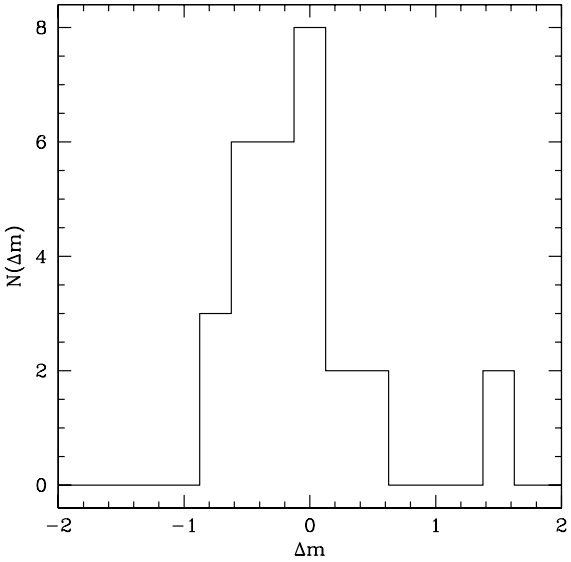

Figure 1. Histogram of microlensing magnifications for the sample of image pairs in Table 3 (bin = 0.25).

If we consider a pair of images, 1 and 2, the continuum ratio relative to the zero point defined by the emission line ratio can be written (in magnitudes) as

$$\begin{aligned}\Delta m(\lambda,t) &= (m_1-m_2)^{\rm con} - (m_1-m_2)^{\rm lin} \\ &= \Delta\mu_1\left(\frac{\lambda}{1+z_l}, t\right) - \Delta\mu_2\left(\frac{\lambda}{1+z_l}, t\right) \\ &\quad + \Delta m_0^{\rm con}\left(\frac{\lambda}{1+z_s}, \Delta t_1 - \Delta t_2\right).\end{aligned} \quad (4)$$

We have referred the equations for the magnification of both images to an arbitrary time, t (note that microlensing-induced variability between a pair of images is uncorrelated).

The first term of Equation (4) is the relative microlensing magnification between images 1 and 2. The significance of the second term, $\Delta m_0^{\rm con}$, which represents the source variability, can be estimated by comparing the intrinsic quasar variability on timescales typical of the time delay between images in gravitational lens systems with the expected distribution of microlensing magnifications. As we shall discuss in Section 4, the intrinsic source variability is not significant for our computations.

In summary, with the proposed method similar information as in the Milky Way MACHO experiments is obtained but with a single-epoch measurement. The objective of this study is to apply this method to published data of quasar microlensing. In Section 2, we collect the data from the literature and fit models to the systems of multiply imaged quasars to derive suitable values of the projected matter density at the image locations. Using these values, probabilistic models for microlensing magnifications are derived in Section 3.1 for a range of fractions of mass in compact objects. Sections 3.2 and 3.3 are devoted to estimate this fraction. Finally, in Section 4 we present and discuss the main conclusions.

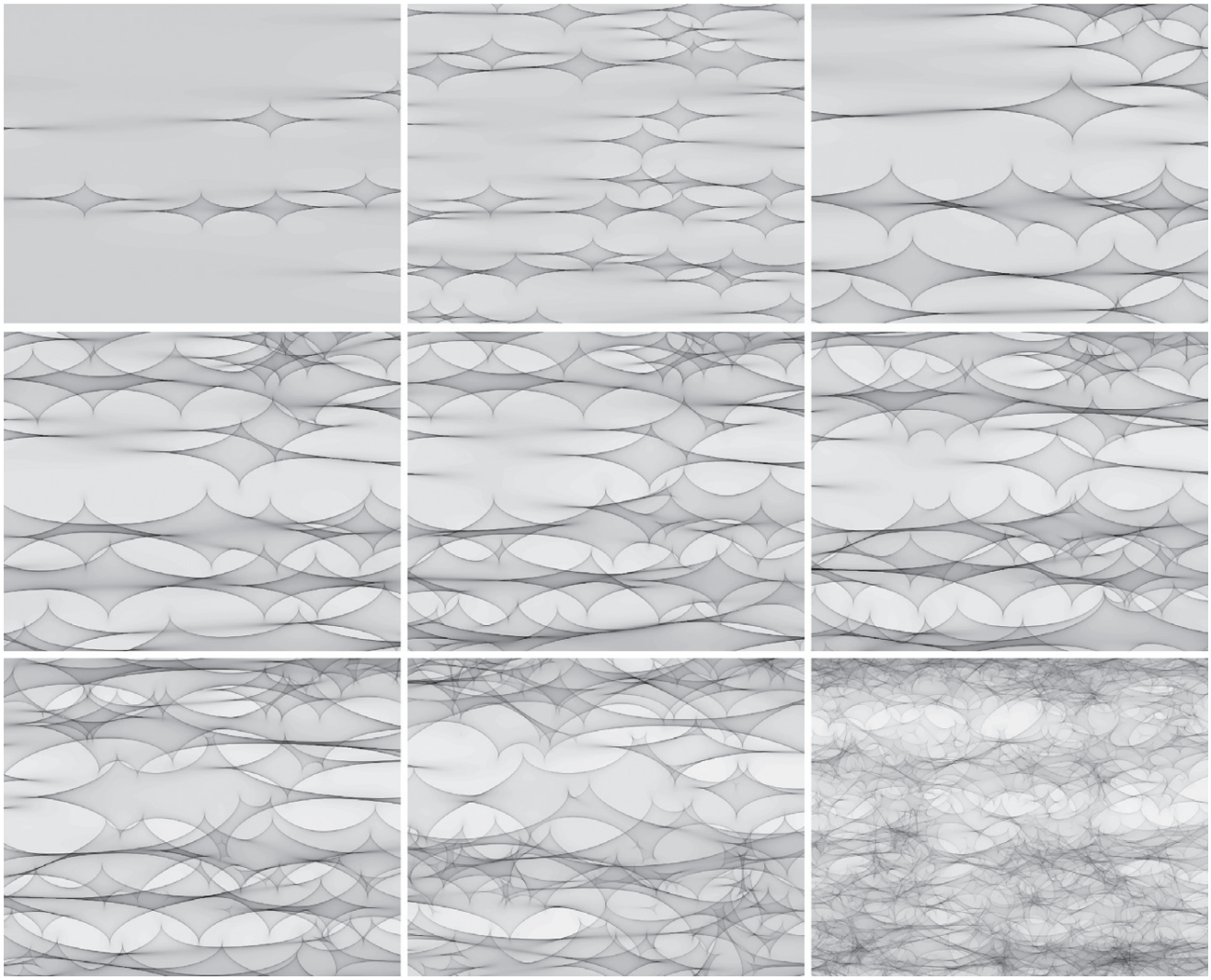

Figure 2. Example of magnification maps for the case $\kappa = \gamma = 0.45$. From top to bottom and from left to right, maps correspond to $\alpha = 0.01$, 0.05, 0.10, 0.15, 0.20, 0.25, 0.30, 0.50, 1.00.

2. OBSERVED MICROLENSING MAGNIFICATIONS AND MACRO-LENS MODELS

We collected the data, Δm (see Equation (4)), examining all the optical spectroscopy[5] found in the literature (see Table 1). In most cases, the microlensing magnification or the scaling of the emission line ratio with respect to the continuum ratio are directly provided by the authors or can be estimated from a figure. For SDSS 0806+2006, FBQ 0951+2635, SDSS J1001+5027, QSO 1017−207, SDSS J1206+4332, HE 1413+117, and SBS 1520+530 we used the electronically available or digitized spectra of the images to estimate the microlensing magnification following the steps described in Mediavilla et al. (2005). In Table 1, we include (when available) the flux ratios for each line and its corresponding continuum. Specific details of the procedure followed to obtain the data are also given.

[6] There are also several X-ray events in the literature that have been explained in terms of microlensing (e.g., Pooley et al. 2007 and references therein). These events probably arise from a tiny inner region, as compared with the optical continuum emitting region, and deserve an analogous but separate study when a sufficiently large sample of X-ray microlensing measurements become available.

For some of the image pairs (∼30% of the sample) there are mid-IR flux ratios available. Except for one system, SDSS J1004+4112 (where image C is probably affected by extinction, Gómez-Álvarez et al. 2006), they are in very good agreement with the emission-line flux ratios (see Table 2). The average difference between mid-IR and emission line flux ratios is only 0.11 mag (0.07 mag if SDSS J1004+4112 is removed). In fact, the agreement is unexpectedly good taking into account the possible influence of extinction and source variability. In any case, this comparison supports the consistency of the basic hypothesis (that the emission line fluxes are not affected by microlensing) and the reliability of the data.

Figure 1 shows the frequency of observed microlensing magnifications, $f_{\rm obs}(\Delta m)$. This histogram exhibits two significant characteristics: the relatively high number of events with low or no microlensing magnification and the concentration (∼80%) of the microlensing events below $|\Delta m| = 0.6$. Any model attempting to describe microlensing magnification should account for these features. At a lower level of significance, the presence of two events of high magnification, $\Delta m \sim 1.5$, should also be noted. The data presented in Table 1 come from many different bibliographic sources with the subsequent lack of information

Table 3
Lens Models

Object	Ratio	Value	$R_{\rm inner}$(kpc)[a]	$R_{\rm outer}$(kpc)[a]	κ_1	κ_2	γ_1	γ_2
HE 0047−1756	Δm_{B-A}	−0.19	$r_B = 3.6$	$r_A = 4.9$	$\kappa_A = 0.43$	$\kappa_B = 0.61$	$\gamma_A = 0.48$	$\gamma_B = 0.65$
HE 0435−1223	Δm_{B-A}	−0.24	$r_B = 7.6$	$r_A = 8.2$	$\kappa_A = 0.46$	$\kappa_B = 0.52$	$\gamma_A = 0.39$	$\gamma_B = 0.59$
	Δm_{C-A}	−0.30	$r_C = 8.2$	$r_A = 8.2$	$\kappa_A = 0.46$	$\kappa_C = 0.46$	$\gamma_A = 0.39$	$\gamma_C = 0.39$
	Δm_{D-A}	0.09	$r_D = 7.0$	$r_A = 8.2$	$\kappa_A = 0.46$	$\kappa_D = 0.56$	$\gamma_A = 0.39$	$\gamma_D = 0.64$
HE 0512−3329	Δm_{B-A}	−0.40	$r_A = 2.2$	$r_B = 3.3$	$\kappa_A = 0.59$	$\kappa_B = 0.41$	$\gamma_A = 0.55$	$\gamma_B = 0.37$
SDSS 0806+2006	Δm_{B-A}	−0.47	$r_A = 7.2$	$r_B = 3.0$	$\kappa_A = 0.34$	$\kappa_B = 0.82$	$\gamma_A = 0.29$	$\gamma_B = 0.77$
SBS 0909+532	Δm_{B-A}	−0.60	$r_A = 3.4$	$r_B = 6.3$	$\kappa_A = 1.00$	$\kappa_B = 0.55$	$\gamma_A = 1.39$	$\gamma_B = 1.19$
SDSS J0924+0219	Δm_{B-A}	0.00	$r_A = 5.2$	$r_B = 5.8$	$\kappa_A = 0.50$	$\kappa_B = 0.45$	$\gamma_A = 0.45$	$\gamma_B = 0.39$
FBQ 0951+2635	Δm_{B-A}	−0.69	$r_A = 3.6$	$r_B = 0.9$	$\kappa_A = 0.28$	$\kappa_B = 1.07$	$\gamma_A = 0.15$	$\gamma_B = 1.02$
QSO 0957+561	Δm_{B-A}	−0.30	$r_B = 5.7$	$r_A = 28.6$	$\kappa_A = 0.20$	$\kappa_B = 1.03$	$\gamma_A = 0.15$	$\gamma_B = 0.91$
SDSS J1001+5027	Δm_{B-A}	0.23	$r_A = 10.6$	$r_B = 5.0$	$\kappa_A = 0.35$	$\kappa_B = 0.74$	$\gamma_A = 0.28$	$\gamma_B = 0.72$
SDSS J1004+4112	Δm_{B-A}	0.00	⋯	⋯	$\kappa_A = 0.48$	$\kappa_B = 0.48$	$\gamma_A = 0.59$	$\gamma_B = 0.48$
	Δm_{C-A}	0.45	⋯	⋯	$\kappa_A = 0.48$	$\kappa_C = 0.38$	$\gamma_A = 0.59$	$\gamma_C = 0.33$
QSO 1017−207	Δm_{B-A}	−0.26	$r_A = 5.4$	$r_B = 1.5$	$\kappa_A = 0.35$	$\kappa_B = 1.23$	$\gamma_A = 0.45$	$\gamma_B = 1.32$
HE 1104−1805	Δm_{B-A}	0.60	$r_A = 8.6$	$r_B = 16.6$	$\kappa_A = 0.64$	$\kappa_B = 0.33$	$\gamma_A = 0.52$	$\gamma_B = 0.21$
PG 1115+080	Δm_{A2-A1}	−0.65	$r_{A1} = 5.8$	$r_{A2} = 5.9$	$\kappa_{A1} = 0.49$	$\kappa_{A2} = 0.51$	$\gamma_{A1} = 0.44$	$\gamma_{A2} = 0.55$
RXS J1131−1231	Δm_{A-B}	1.39	$r_A = 10.1$	$r_B = 10.2$	$\kappa_A = 0.44$	$\kappa_B = 0.43$	$\gamma_A = 0.59$	$\gamma_B = 0.51$
	Δm_{C-B}	1.58	$r_A = 10.1$	$r_C = 10.7$	$\kappa_B = 0.43$	$\kappa_C = 0.42$	$\gamma_B = 0.51$	$\gamma_C = 0.50$
SDSS J1206+4332	Δm_{A-B}	−0.56	$r_B = 10.02$	$r_A = 15.0$	$\kappa_A = 0.43$	$\kappa_B = 0.63$	$\gamma_A = 0.41$	$\gamma_B = 0.72$
SDSS J1353+1138	Δm_{A-B}	0.00	$r_B = 1.6$	$r_A = 5.2$	$\kappa_A = 0.30$	$\kappa_B = 0.96$	$\gamma_A = 0.22$	$\gamma_B = 0.89$
HE 1413+117[b]	Δm_{B-A}	0.00	⋯	⋯	$\kappa_A = 0.53$	$\kappa_B = 0.43$	$\gamma_A = 0.64$	$\gamma_B = 0.34$
	Δm_{C-A}	−0.25	⋯	⋯	$\kappa_A = 0.53$	$\kappa_C = 0.46$	$\gamma_A = 0.64$	$\gamma_C = 0.35$
	Δm_{D-A}	−0.75	⋯	⋯	$\kappa_A = 0.53$	$\kappa_D = 0.58$	$\gamma_A = 0.64$	$\gamma_D = 0.69$
B J1422+231	Δm_{A-B}	0.16	$r_B = 5.2$	$r_A = 5.3$	$\kappa_A = 0.38$	$\kappa_B = 0.39$	$\gamma_A = 0.53$	$\gamma_B = 0.66$
	Δm_{C-B}	0.02	$r_B = 5.2$	$r_C = 5.7$	$\kappa_B = 0.39$	$\kappa_C = 0.36$	$\gamma_B = 0.66$	$\gamma_C = 0.48$
	Δm_{D-B}	−0.08	$r_B = 5.2$	$r_D = 1.3$	$\kappa_D = 1.54$	$\kappa_B = 0.39$	$\gamma_D = 1.81$	$\gamma_B = 0.66$
SBS 1520+530	Δm_{B-A}	−0.39	$r_A = 9.5$	$r_B = 3.0$	$\kappa_A = 0.29$	$\kappa_B = 0.90$	$\gamma_A = 0.15$	$\gamma_B = 0.85$
WFI J2033−4723	Δm_{B-C}	−0.50	$r_C = 6.8$	$r_B = 11.2$	$\kappa_B = 0.38$	$\kappa_C = 0.61$	$\gamma_B = 0.25$	$\gamma_C = 0.73$
	Δm_{A2-A1}	0.00	$r_{A2} = 8.2$	$r_{A1} = 9.3$	$\kappa_{A1} = 0.48$	$\kappa_{A2} = 0.55$	$\gamma_{A1} = 0.39$	$\gamma_{A2} = 0.65$

Notes.
[a] Computed using a concordance cosmology.
[b] Lens redshift unknown.

Table 4
Frequency Distribution of Image Pairs, n_{k_1,k_2}

	$k_2 = 0.35$	$k_2 = 0.45$	$k_2 = 0.55$	$k_2 = 0.75$	$k_2 = 0.85$	$k_2 = 1.05$	$k_2 = 1.15$	$k_2 = 1.25$	$k_2 = 1.55$	$k_2 = 1.75$
$k_1 = 0.35$	2	1	⋯	3	2	3	⋯	1	1	⋯
$k_1 = 0.45$	⋯	4	9	1	⋯	⋯	⋯	⋯	⋯	⋯
$k_1 = 0.55$	⋯	⋯	1	⋯	⋯	1	⋯	⋯	⋯	⋯

about measurement procedures and estimate of uncertainties. However, even with this limitation, the low frequency of high magnification microlensing events in the optical seems to be a reliable observational result.

For each of the gravitational lens systems in Table 3 we have used a singular isothermal sphere plus external shear model (SIS+γ_e) to estimate values of the total projected matter density κ and the shear γ at the locations of the images (see Table 3). The models have been computed with the "lensmodel" code by Keeton (2001) to fit the positions of the images (CASTLES, http://www.cfa.harvard.edu/castles/). For double systems we have used the emission-line flux ratios between images as an additional constraint.

In Table 4, we show n_{κ_1,κ_2} ($\kappa_1 < \kappa_2$), the frequency distribution of image pairs that occur at combined projected matter densities (κ_1, κ_2). The distribution peaks at bin ($\kappa_1 = 0.45$, $\kappa_2 = 0.55$). In many of the image pairs in Table 3 the images are roughly located at similar distances from the lens galaxy center, $r_1 \sim r_2$. In an SIS model the convergence for each of the lensed images is given by $\kappa_1 = 1/2(1+x)$ and $\kappa_2 = 1/2(1-x)$, where x is the position of the source in units of the Einstein radius. The image configuration $r_1 \sim r_2$ is obtained when $x \gtrsim 0$; therefore, the expected values for the convergence are $\kappa_1 \lesssim 0.5$ and $\kappa_2 \gtrsim 0.5$. This is in agreement with Table 4 and in fact this simple reasoning could have been used to estimate, from a statistical point of view, the peak of the distribution of convergence values, n_{κ_1,κ_2}, in our sample.

Observational uncertainties in the flux ratios, differential extinction in the lens galaxy and more complicated mass distributions for modeling the lens galaxy could have an important impact on the estimates of κ and γ. Therefore, the values for κ and γ in Table 3 computed for an SIS+γ_e model should be taken individually only as compatible values with high uncertainties. However, we will assume that the distribution of values in its entirety can be considered as statistically representative for the sample of observed image pairs. Fortunately, the uncertainty in the macro-lens models does not play a crucial role in the conclusions of our study.

3. STATISTICAL ANALYSIS OF THE OBSERVED MICROLENSING MAGNIFICATIONS

To analyze the microlensing magnification data, we need to consider that each Δm measurement results from the flux ratio of two images seen through different locations at the lens galaxy. The microlensing magnification probability of a given image, $f_{\kappa_{*1},\kappa_1,\gamma_1}(m_1)$, depends on the projected matter density in compact objects, κ_{*1}, the total projected mass density, κ_1, and the shear, γ_1. Thus, the probability distribution of the difference in microlensing magnification of a pair of images, $\Delta m = m_1 - m_2$, is given by the integral

$$f_{\kappa_{*1},\kappa_{*2},\kappa_1,\kappa_2,\gamma_1,\gamma_2}(\Delta m) = \int f_{\kappa_{*1},\kappa_1,\gamma_1}(m_1) f_{\kappa_{*2},\kappa_2,\gamma_2} \times (m_1 - \Delta m) dm_1. \quad (5)$$

To simplify the analysis we will suppose that the fraction of matter in compact objects, $\alpha = \kappa_*/\kappa$, is the same everywhere. The probability distribution of the difference in microlensing magnification of a pair of images can then be written as

$$f_{\alpha\kappa_1,\alpha\kappa_2,\kappa_1,\kappa_2,\gamma_1,\gamma_2}(\Delta m) = \int f_{\alpha\kappa_1,\kappa_1,\gamma_1}(m_1) f_{\alpha\kappa_2,\kappa_2,\gamma_2} \times (m_1 - \Delta m) dm_1. \quad (6)$$

From this expression we can evaluate the probability of obtaining a microlensing measurement Δm_i from a pair of images, $f^i_{\alpha\kappa_1^i,\alpha\kappa_2^i,\kappa_1^i,\kappa_2^i,\gamma_1^i,\gamma_2^i}(\Delta m_i)$. Then, to estimate α using all the available information we maximize the likelihood function corresponding to the N measurements collected in Table 1,

$$\log L(\alpha) = \sum_{i=1}^{N} \log f^i_{\alpha\kappa_1^i,\alpha\kappa_2^i,\kappa_1^i,\kappa_2^i,\gamma_1^i,\gamma_2^i}(\Delta m_i). \quad (7)$$

3.1. Probability Distributions of the Difference in Microlensing Magnifications for Image Pairs, $f_{\alpha\kappa_1,\alpha\kappa_2,\kappa_1,\kappa_2,\gamma_1,\gamma_2}$

We first compute the microlensing magnification probability distributions for one image, $f_{\alpha\kappa,\kappa,\gamma}(m)$. The first step is to simulate microlensing magnification maps for the different values of κ and γ in Table 3. We consider several values for the fraction of mass in compact objects[6]: $\alpha = 1$, 0.5, 0.3, 0.25, 0.2, 0.15, 0.10, 0.05, 0.03, and 0.01. The histogram of each magnification map then provides a frequency distribution model of microlensing magnifications.

We obtain square maps 24 Einstein radii on a side with a spatial resolution of 0.012 Einstein radii per pixel. To compute the magnification maps we use the inverse polygon mapping method described in Mediavilla et al. (2006). An example of the maps is shown in Figure 2. The microlensing magnification at a given pixel is then obtained as the ratio of the magnification in the pixel to the average magnification. Histograms of these normalized maps give the relative frequency of microlensing magnifications for a pixel-size source (see some examples in Figure 3). These distributions are in agreement with the results obtained with a different method by Lewis & Irwin (1995).

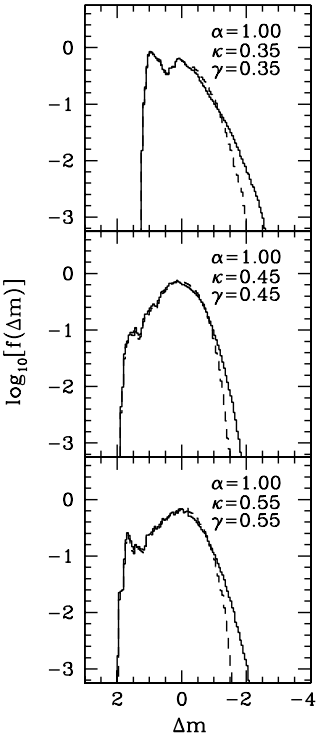

Figure 3. Relative frequency of microlensing magnifications, $f_{\alpha\kappa,\kappa,\gamma}$, for pixel size (solid line) and $r_s = 2.6 \times 10^{15}$ cm (dashed line) sources (see the text). Examples for three different values of κ in the case $\kappa = \gamma$, see the text.

To model the unresolved quasar source we consider a Gaussian with $r_s = 2.6 \times 10^{15}$ cm (1 ld; Shalyapin et al. 2002; Kochanek 2004). The convolution of this Gaussian with the "pixel" maps gives the magnification maps for the quasar. For a system with redshifts $z_l \sim 0.5$ and $z_s \sim 2$ for the lens and the source respectively, the Einstein radius for a compact object of mass M is $\eta_0 \sim 5.2 \times 10^{16} \sqrt{M/M_\odot}$ cm. Thus, for $M = 1\,M_\odot$, $\eta_0 \sim 5.2 \times 10^{16}$ cm, and the size of a pixel is 6.2×10^{14} cm.

Finally, the histograms of the convolved maps give the frequency distributions of microlensing magnifications, $f_{\alpha\kappa,\kappa,\gamma}(m)$, which show differences with respect to the results obtained for a pixel-size source at the high magnification wing (the same effect that can be observed in Lewis & Irwin 1995). From the cross-correlation of pairs of these individual probability functions $f_{\alpha\kappa_1,\kappa_1,\gamma_1}(m_1)$, and $f_{\alpha\kappa_2,\kappa_2,\gamma_2}(m_2)$ (see Equation (6)) we obtain the probability function of the difference in microlensing magnification between two images, $f_{\alpha\kappa_1,\alpha\kappa_2,\kappa_1,\kappa_2,\gamma_1,\gamma_2}(\Delta m = m_1 - m_2)$. In Figures 4–6 the $f_{\alpha\kappa_1,\alpha\kappa_2,\kappa_1,\kappa_2,\gamma_1,\gamma_2}(\Delta m)$ distributions corresponding to the 29 image pairs of Table 3 are plotted.

3.2. Maximum Likelihood Estimate of the Fraction of Mass in Compact Objects, α: Confidence Intervals

In Figure 7, we present $\log L(\alpha)$ (see Equation (7)). Using the $\log L(\alpha \pm n\sigma_\alpha) \sim \log L_{\max} - n^2/2$ criterion we derive $\alpha(\log L_{\max}) = 0.10^{+0.04}_{-0.03}$ (90% confidence interval).

The maximum likelihood method can be affected by errors in the microlensing measurements, $\sigma_{\Delta m_i}$. From Equation (7) we

[6] This sequence of microlensing maps parameterized by $\alpha = \kappa_*/\kappa$ assumes that the overall mass distribution (compact objects and smooth mass distribution) is close to isothermal. However, in many studies (e.g., Dai et al. 2009) the lens galaxy is simulated with a constant mass-to-light (M/L) ratio model representing the galaxy stellar content (typically a de Vaucouleurs profile) embedded in a smooth halo of dark matter with no compact objects (a NFW halo, for instance; Navarro et al. 1996). In this case, the sequence of models is parameterized by $f_{M/L}$, the fraction of mass in the stellar component relative to a constant M/L ratio model with no halo (that is, the model with $f_{M/L} = 1$). Although the meanings of α and $f_{M/L}$ are different, the results of both procedures can be compared obtaining from each $f_{M/L}$ model values of κ and κ_*.

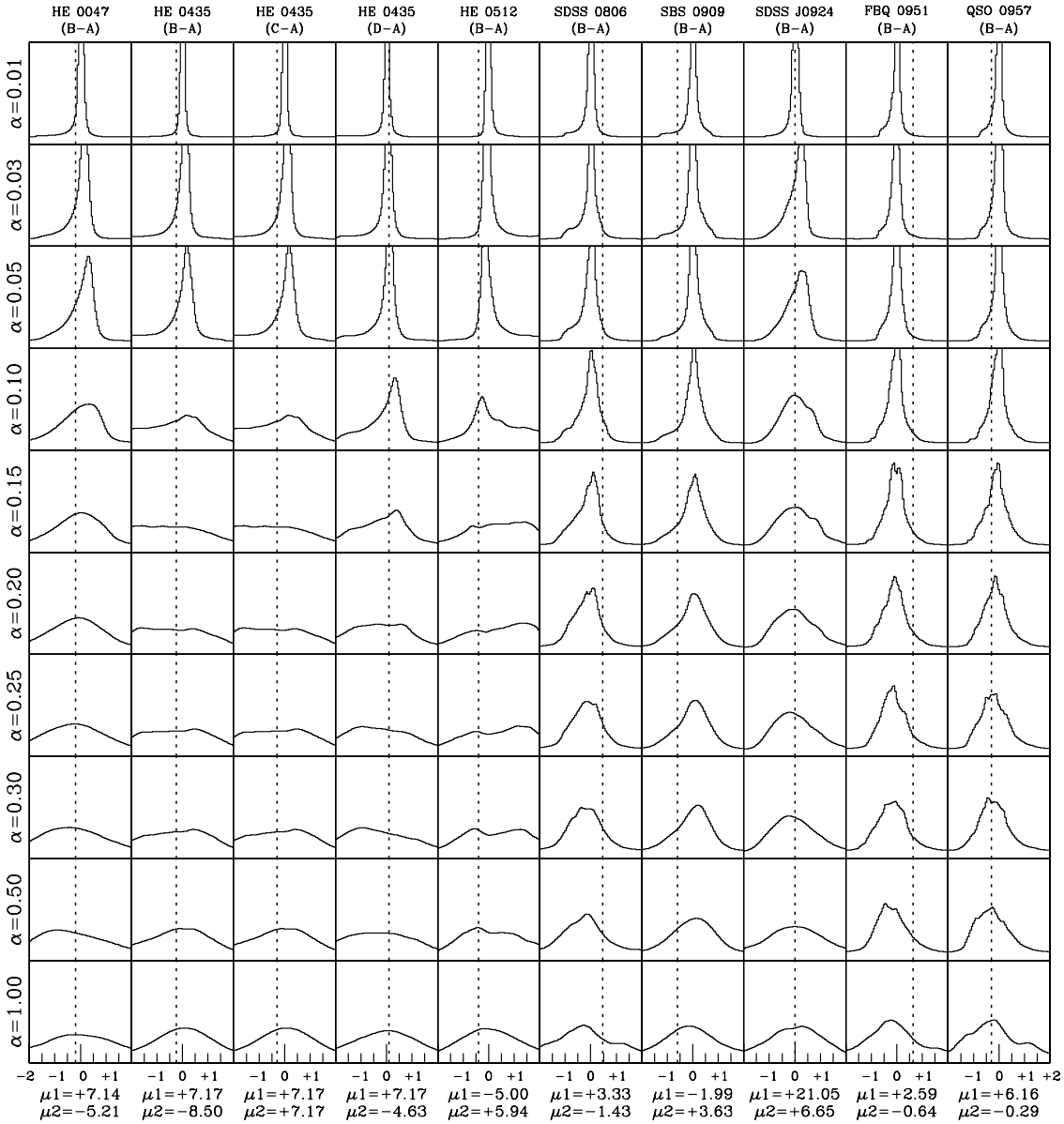

Figure 4. Probability models, $f_{\alpha\kappa_1,\alpha\kappa_2,\kappa_1,\kappa_2,\gamma_1,\gamma_2}(\Delta m = m_1 - m_2)$, corresponding to each image pair in the sample for different values of the fraction of mass in compact objects, α (see the text). μ_1 and μ_2 are the magnifications of the images considered in each pair. The vertical dashed line corresponds to the microlensing measurement value.

obtain

$$\Delta \log L(\alpha) = \sum_{i=1}^{N} \frac{1}{f^i_{\alpha\kappa_1^i,\alpha\kappa_2^i,\kappa_1^i,\kappa_2^i,\gamma_1^i,\gamma_2^i}(\Delta m_i)} \frac{\partial f^i_{\alpha\kappa_1^i,\alpha\kappa_2^i,\kappa_1^i,\kappa_2^i,\gamma_1^i,\gamma_2^i}(\Delta m_i)}{\partial \Delta m_i} \sigma_{\Delta m_i}. \quad (8)$$

According to this last expression, microlensing measurement errors do not significantly affect the likelihood of flat probability distributions (typical of large values of α). On the contrary, the likelihood functions corresponding to low values of α (associated with sharply peaked probability distributions) can be strongly modified by the microlensing measurement errors. Note, moreover, that these changes tend to penalize the low α hypothesis.

To show the impact of $\sigma_{\Delta m_i}$ on the maximum likelihood estimate of α, in Figure 7 we also present $\log L(\alpha)$ (see Equation (7)) with error bars, $\pm\Delta \log L(\alpha)$, estimated considering that each Δm_i is a normally distributed variable with $\sigma_{\Delta m_i} = 0.20$ (a realistic estimate). Using the $\log L(\alpha \pm n\sigma_\alpha) \sim \log L_{\max} - n^2/2$ criterion and taking into account the error bars of $\log L(\alpha)$, we derive $\alpha(\log L_{\max}) = 0.05^{+0.09}_{-0.03}$ (90% confidence interval).

3.3. Influence of the Continuum Source Size, Influence of the Microlenses Mass

Increasing the size parameter of the Gaussian representing the continuum source, r_s, affects the previous results by smoothing the magnification patterns and, consequently, the probability distributions. To study the dependence of the estimate of α on the source size we have computed probability and likelihood functions for several values of this parameter, $r_s = 0.62 \times 10^{15}$, 2.6×10^{15}, 8×10^{15}, and 26×10^{15} cm. To correct r_s from projection effects we have taken into account that the intrinsic and projected source areas are related by a $\cos i$

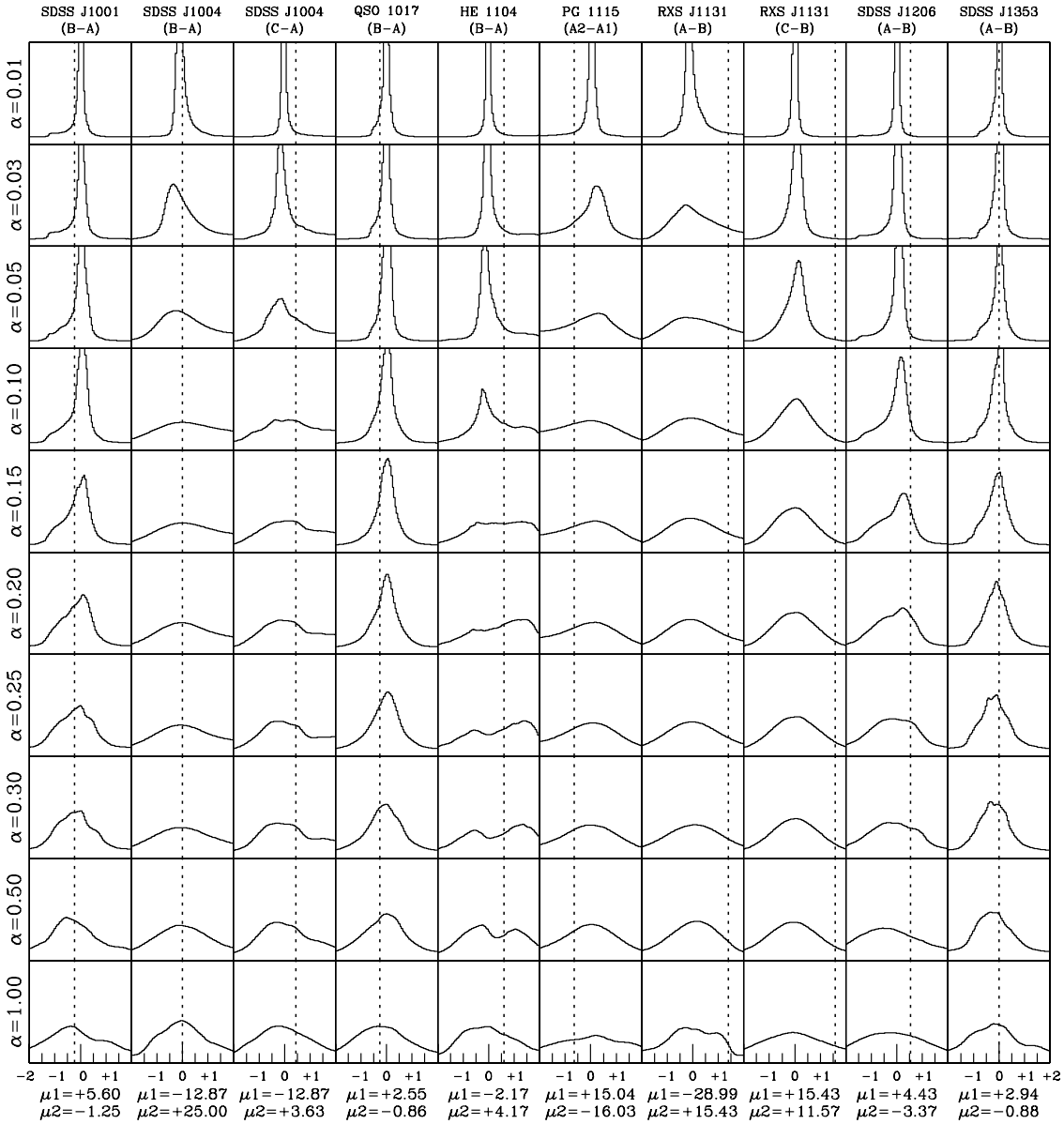

Figure 5. Probability models, $f_{\alpha\kappa_1,\alpha\kappa_2,\kappa_1,\kappa_2,\gamma_1,\gamma_2}(\Delta m = m_1 - m_2)$, corresponding to each image pair in the sample for different values of the fraction of mass in compact objects, α (see the text). μ_1 and μ_2 are the magnifications of the images considered in each pair. The vertical dashed line corresponds to the microlensing measurement value.

factor; that is $r_s \sim \sqrt{\cos i}\, r_{s_0}$. Assuming that the (disk) sources are randomly oriented in space (the probability of finding a disk with inclination, i, proportional to $\sin i$) and averaging on the inclination, we obtain $r_{s_0} \sim 1.5 r_s$. In Figure 8, we present the likelihood functions corresponding to sources of several deprojected size parameters, r_{s_0}. In Figure 9, we plot the maximum likelihood estimate of α versus[7] r_{s_0}. Error bars correspond to 90% confidence intervals. According to this figure, low values of α are expected for continuum source sizes, r_{s_0}, of the order of 10^{16} cm or less. Observing microlensing variability for nine gravitationally lensed quasars Morgan et al. (2007) measure the accretion disk size. The average value of the nine half-light radius determinations is $\langle r_{1/2} \rangle = 6 \times 10^{15}$ cm. For this value we found (see Figure 9) $\alpha = 0.05^{+0.09}_{-0.03}$. Morgan et al. (2007) report a scaling between the accretion disk size and the black hole mass. In the range of black hole masses considered by Morgan et al. (2007) the maximum is $M_{\rm BH} = 2.37 \times 10^9\, M_\odot$, which, using the scaling derived by these authors, corresponds to $r_{1/2} = 2.4 \times 10^{16}$ cm. For this size we obtain (see Figure 9) $\alpha \sim 0.10$. Values $M_{\rm BH} \geqslant 10^{10}\, M_\odot$ ($r_{1/2} \geqslant 3.4 \times 10^{16}$ cm) should be considered to obtain $\alpha \geqslant 0.20$. On the other hand, Pooley et al. (2007) comparing X-ray and optical microlensing in a sample of 10 lensed quasars inferred $r_{1/2} \sim 1.3 \times 10^{16}$ cm. For this size we obtain (see Figure 9) $\alpha = 0.10^{+0.05}_{-0.06}$. Thus, according to these recent size estimates based on the observations of two relatively large samples of gravitational lenses, high values of α are possible only if the continuum source size is substantially larger than expected.

Owing to the scaling of the Einstein radius with mass, $\eta_0 \propto \sqrt{M}$, a change in the mass of microlenses can be

[8] Note that for the considered Gaussian intensity profile the radii enclosing 50% and 90% of the source energy are related to the Gaussian source size parameter, r_{s_0}, according to $r_{1/2} = r(50\%) = 1.18 r_{s_0}$ and $r(90\%) = 2.1 r_{s_0}$.

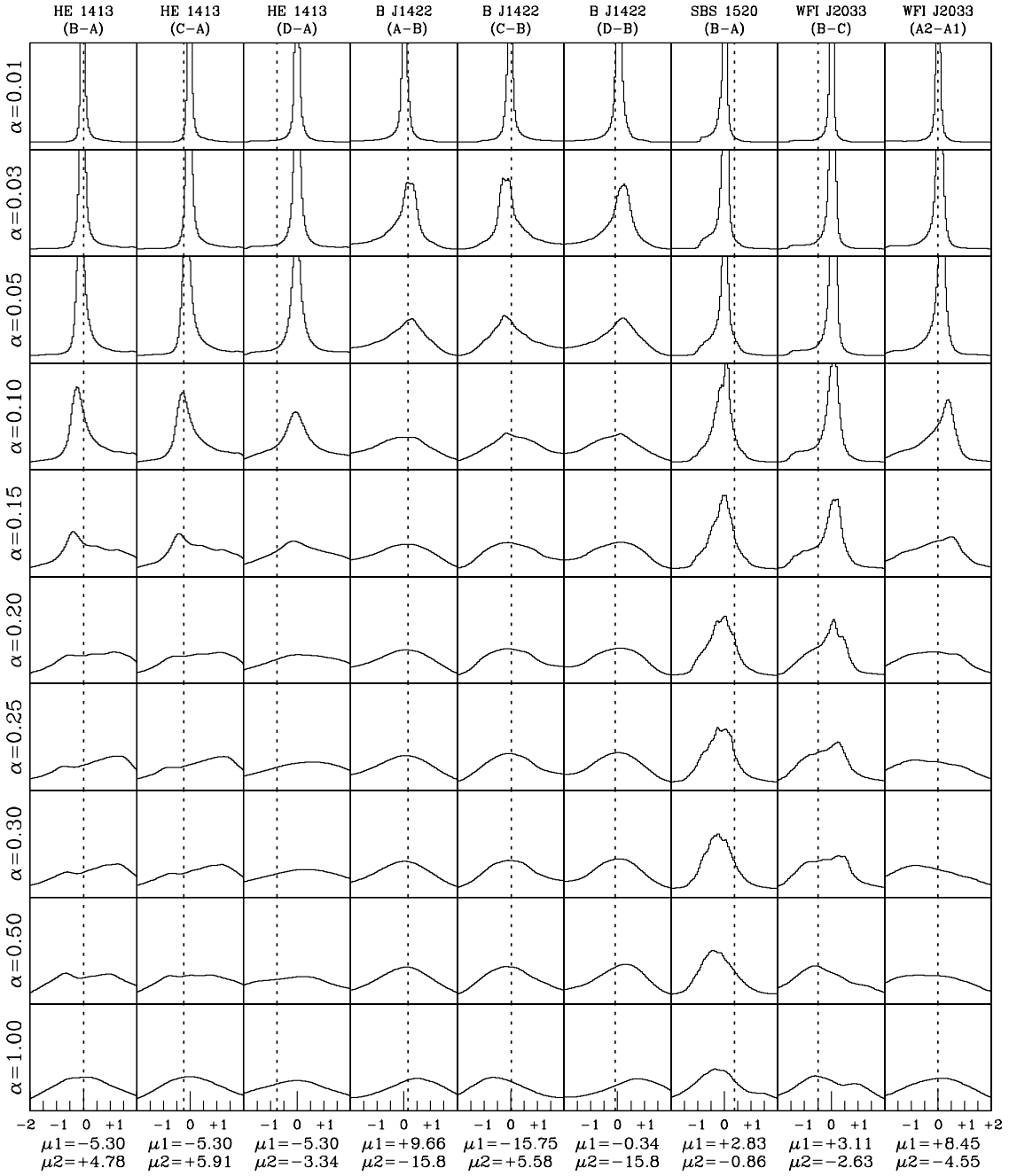

Figure 6. Probability models, $f_{\alpha\kappa_1,\alpha\kappa_2,\kappa_1,\kappa_2,\gamma_1,\gamma_2}(\Delta m = m_1 - m_2)$, corresponding to each image pair in the sample for different values of the fraction of mass in compact objects, α (see text). μ_1 and μ_2 are the magnifications of the images considered in each pair. The vertical dashed line corresponds to the microlensing measurement value.

alternatively seen as a change in the spatial scaling of the magnification pattern that leaves invariant the projected mass density, κ. Thus, multiplying the mass of the microlenses by a factor C (and leaving unaltered the continuum size) is equivalent to multiplying the size of the continuum source by a factor $1/\sqrt{C}$ (leaving unaltered the masses of microlenses). Then the computed models corresponding to sources of sizes $r_s = 0.62 \times 10^{15}$, 2.6×10^{15}, and 8×10^{15} cm (with 1 $M_\odot$ microlenses) are equivalent to models corresponding to microlens masses of 17, 1, and 0.1 $M_\odot$ (with $r_s = 2.6 \times 10^{15}$ cm). This result implies that the probability models do not differ significantly if we change the mass of microlenses between 17 and 0.1 $M_\odot$. Thus, microlensing statistics are insensitive to changes of mass in the expected range of stellar masses.

4. DISCUSSION AND CONCLUSIONS

In the previous sections, we have extended to the extragalactic domain the local (Milky Way, LMC, and M31) use of microlensing to probe the properties of the galaxy halos. Although our primary aim was to explore the practical application of the proposed method, we found that the data available in the literature can be consistently interpreted only under the hypothesis of a very low mass fraction in microlenses; at 90% confidence: $\alpha(\log L_{\max}) = 0.05^{+0.09}_{-0.03}$ (maximum likelihood estimate) for a

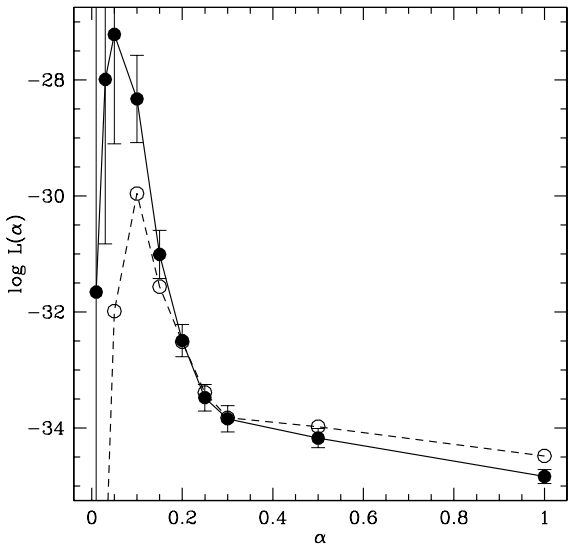

Figure 7. Likelihood function vs. fraction of mass in compact objects. Dashed line (circles): likelihood function supposing that the microlensing measurements are unaffected by errors. Continuous line (filled circles): likelihood function supposing that the microlensing measurements are affected by 0.2 mag errors. See the text for details.

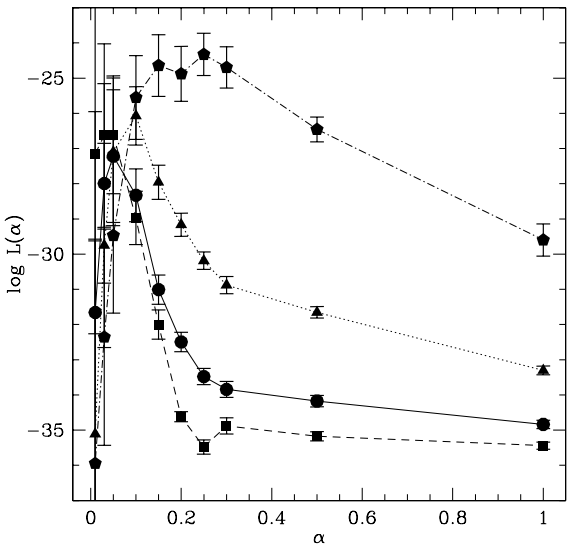

Figure 8. Likelihood functions corresponding to sources of deprojected size parameter, r_{s_0}: 0.8×10^{15} cm(squares; dashed line), 3.9×10^{15} cm (circles; continuous line), 12.4×10^{15} cm (triangles; dotted line), and 40.4×10^{15} cm (pentagons; dot-dashed line).

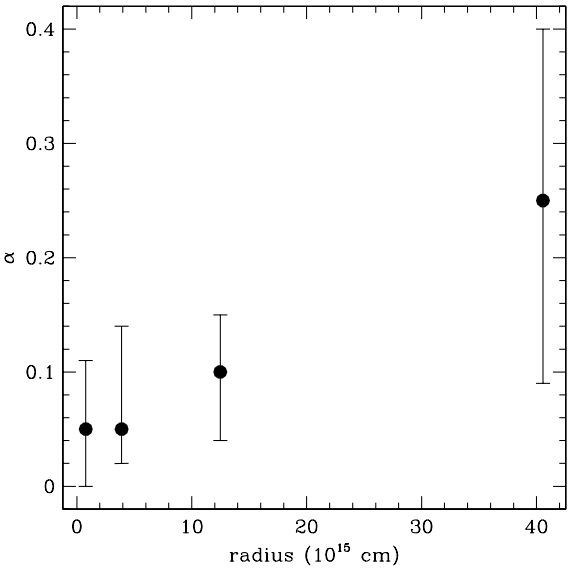

Figure 9. Maximum likelihood estimates of α vs. deprojected source size parameter, r_{s_0}. Error bars correspond to 90% confidence intervals.

quasar continuum source of intrinsic size $r_s = 2.6 \times 10^{15}$ cm. This result arises directly from the shape of the histogram of microlensing magnifications, with a maximum of events close to no magnification and stands for a wide variety of microlensing models statistically representative of the considered image pairs. There is a dependence of the estimate of α on the source size but high values of the mass fraction ($\alpha > 0.2$) are possible only for unexpectedly large source sizes ($r_s > 4 \times 10^{16}$ cm). The low mass fraction is in good agreement with the results of EROS (Tisserand et al. 2007) for the Milky Way, with the estimate of OGLE for the LMC (Wyrzykowski et al. 2009), and with the limit established by MEGA (de Jong et al. 2006) for M31. The agreement is also good with the few microlensing-based estimates available for individual objects. In RXJ 1131−1231, Dai et al. (2009) found $\alpha \sim 0.1$. In PG 1115+080, Morgan et al. (2008) obtained values in the range $\alpha = 0.08$–0.15. For the same system, Pooley et al. (2009) found $\alpha \sim 0.1$ for a source of size $r_s = 1.3 \times 10^{16}$ cm.

On the other hand, our estimate of the fraction of mass in microlenses, $\alpha(\log L_{\max}) = 0.05^{+0.09}_{-0.03}$, approximates the expectations for the fraction of visible matter. Jiang & Kochanek (2007), for instance, comparing the mass inside the Einstein ring in 22 gravitational lens galaxies with the mass needed to produce the observed velocity dispersion, inferred average stellar mass fractions of 0.026 ± 0.006 (neglecting adiabatic compression) and 0.056 ± 0.011 (including adiabatic compression). As discussed in Jiang & Kochanek (2007) these values are also in agreement with other estimates of the stellar mass fraction that relied on stellar population models: ∼0.08 (Lintott et al. 2006), $0.065^{+0.010}_{-0.008}$ (Hoekstra et al. 2005), and $0.03^{+0.02}_{-0.01}$ (Mandelbaum et al. 2006). Thus, we can conclude that microlensing is probably caused by stars in the lens galaxy, and that there is no statistical evidence for MACHOS in the halos of the 20 galaxies of the sample we considered.

How robust are these results? There are several sources of uncertainty to consider. First, we neglected in Equation (4) the term arising from source variability, $\Delta m_0^{\rm con}$. From a group of 17 gravitational lenses with photometric monitoring available in the literature we estimate an average gradient of variability of 0.1 mag year^{-1}. Taking into account that the average delay between images is about three months (a conservative estimate; note that the group of lens systems used includes many doubles, some of them with very large time delays) we can expect an amplitude related to intrinsic source variability of $\Delta m_0^{\rm con} \sim 0.03$, which, according to the histogram of magnifications (Figure 1), is not significant. Moreover, if we assume that the probability of $\Delta m_0^{\rm con}$ is normally distributed, the global effect of source variability is to broaden the histogram of microlensing magnifications, diminishing the peak and enhancing the wing. In other words, source variability leads to an overestimate of α. Thus, the mass fraction should be even lower if significant source variability were hidden in the data. In the same way, other sources of error in the data, such as the difficulty in separating line and continuum or in removing from the narrow emission lines the high ionization broad emission lines that could be

partially affected by microlensing, probably tend to induce additional magnitude differences, Δm, between the images and, hence, to an overestimate of α. On the contrary, cross-contamination between the spectra of a pair of images masks the impact of microlensing and may affect our results. Although most of the bibliographic sources of microlensing measurements analyze this problem concluding that the spatial resolution was sufficient to extract the spectra without contamination, it is clear that high signal-to-noise ratio (S/N) data obtained in subarcsecond seeing conditions will help to control this important issue.

Another point to address is the treatment of some of the quads, where only a subset of the images are used. Are we systematically excluding faint images that might be highly demagnified by microlensing? Let us examine the four incomplete quads in our sample. The fold lens SDSS J1004+4112 has two close images A and B. A is probably a saddle-point image and shows the most anomalous flux (Ota et al. 2006). In contrast, the optical/X-ray flux ratios of C and D are almost the same. Thus, there is no reason to suppose that the image without a useful spectrum (D) has higher microlensing probability than the others. PG 1115+080 is another fold quad. A_1 and A_2 are the two images closest to the critical curve and have a (moderately) anomalous flux ratio and optical variability (Pooley et al. 2007). The two images without available spectra (C and D) show only a small optical variability and are not particularly prone to microlensing. In RXS J1131−1231, the most anomalous flux ratio is B/C and A is a saddle-point image (Sluse et al. 2006). Image D (the one with no available spectrum) also has an anomalous flux but is not more susceptible to microlensing than the other images. Thus, in three of the four incomplete quads there is no reason to suppose that we are biasing the sample toward image pairs with lower microlensing probability. The case of SDSS 0924+0219 is more problematic. There are two sets of data for this object, one by Eigenbrod et al. (2006) based on observations of the low ionization lines [Mg II] and [C III], which, after two epochs of observation, reveals no difference between the line and continuum flux ratios of components A and B. The other set of data (Keeton et al. 2006) is based on Lyα observations (a high ionization emission line supposed to come from a smaller region than the low ionization emission lines) and microlensing is detected not only in the continuum but also in the emission lines. This implies that the baseline for no microlensing magnification cannot be defined and, consequently, we could not consider Keeton et al. (2006) results. Anyway, we have repeated (as a test) the entire maximum likelihood estimate procedure to derive α but now using for SDSS 0924+0219 the microlensing measurements by Keeton et al. (2006). The results are almost identical: $\alpha = 0.05^{+0.10}_{-0.03}$.

The size of the sample also limits the statistical interpretation. An improvement in the S/N of the histogram of microlensing magnifications is very important to ascertain the statistical significance of the low frequency of events at large magnification (only two events of high magnification are detected), which can impose severe constraints on the microlensing models. Another reason to increase the size of the sample is the possibility to define subsamples at different galactocentric distances where different ratios of visible to dark matter are expected. In the same way, it would be possible to define subsamples according to the type of lens galaxy or other interesting properties of lens systems.

In any case, the impact of the main result of our study—absence of MACHOS in the 10–0.1 $M_\odot$ mass range in the halos of lens galaxies—and its future prospects, points to the need to improve the statistical analysis in two ways: increasing the number, quality, and homogeneity of the microlensing magnification measurements from new observations, and reducing the uncertainties in the macro-lens models.

We thank the anonymous referee for valuable comments and suggestions. We are grateful to A. Eigenbrod, P. Green, M. Oguri, L. Wisotzki, and O. Wucknitz for kindly providing spectra. This work was supported by the European Community's Sixth Framework Marie Curie RTN (MRTN-CT-505183 "ANGLES") and by the Ministerio of Educación y Ciencia of Spain with the grants AYA2004-08243-C03-01 and AYA2004-08243-C03-03. V.M. acknowledges support by FONDECYT grant 1071008. J.A.M. is also supported by the Generalitat Valenciana with the grant PROMETEO/2009/64.

REFERENCES

Abajas, C., Mediavilla, E., Muñoz, J. A., Popović, L. Č., & Oscoz, A. 2002, ApJ, 576, 640
Alcock, C., et al. 2000, ApJ, 542, 281
Belokurov, V., Evans, N. W., & Le Du, Y. 2004, MNRAS, 352, 233
Calchi Novati, S., et al. 2005, A&A, 443, 911
Chang, K., & Refsdal, S. 1979, Nature, 282, 561
Chavushyan, V. H., Vlasyuk, V. V., Stepanian, J. A., & Erastova, L. K. 1997, A&A, 318, L67
Chiba, M., Minezaki, T., Kashikawa, N., Kataza, H., & Inoue, K. T. 2005, ApJ, 627, 53
Dai, X., Kochanek, C. S., Chartas, G., Kozlowski, S., Morgan, C. W., Garmire, G., & Agol, E. 2009, arXiv:0906.4342
de Jong, J. T. A., et al. 2006, A&A, 446, 855
Eigenbrod, A., Courbin, F., Dye, S., Meylan, G., Sluse, D., Vuissoz, C., & Magain, P. 2006, A&A, 451, 747
Goicoechea, L. J., Gil-Merino, R., & Ullán, A. 2005, MNRAS, 360, L60
Gómez-Álvarez, P., Mediavilla, E., Muñoz, J. A., Arribas, S., Sánchez, S. F., Oscoz, A., Prada, F., & Serra-Ricart, M. 2006, ApJ, 645, L5
Griest, K., & Thomas, C. L. 2005, MNRAS, 359, 464
Hoekstra, H., Hsieh, B. C., Yee, H. K. C., Lin, H., & Gladders, M. D. 2005, ApJ, 635, 73
Impey, C. D., Foltz, C. B., Petry, C. E., Browne, I. W. A., & Patnaik, A. R. 1996, ApJ, 462, L53
Inada, N., et al. 2006, AJ, 131, 1934
Jiang, G., & Kochanek, C. S. 2007, ApJ, 671, 1568
Kaspi, S., Smith, P. S., Netzer, H., Maoz, D., Jannuzi, B. T., & Giveon, U. 2000, ApJ, 533, 631
Keeton, C. R. 2001, arXiv:astro-ph/0102340
Keeton, C. R., Burles, S., Schechter, P. L., & Wambsganss, J. 2006, ApJ, 639, 1
Kochanek, C. S. 2004, ApJ, 605, 58
Lewis, G. F., & Irwin, M. J. 1995, MNRAS, 276, 103
Lewis, G. F., & Irwin, M. J. 1996, MNRAS, 283, 225
Lintott, C. J., Ferreras, I., & Lahav, O. 2006, ApJ, 648, 826
MacLeod, C. L., Kochanek, C. S., & Agol, E. 2009, ApJ, 699, 1578
Mandelbaum, R., Seljak, U., Kauffmann, G., Hirata, C. M., & Brinkmann, J. 2006, MNRAS, 368, 715
Mediavilla, E., Muñoz, J. A., Kochanek, C. S., Falco, E. E., Arribas, S., & Motta, V. 2005, ApJ, 619, 749
Mediavilla, E., Muñoz, J. A., Lopez, P., Mediavilla, T., Abajas, C., Gonzalez-Morcillo, C., & Gil-Merino, R. 2006, ApJ, 653, 942
Morgan, N. D., Caldwell, J. A. R., Schechter, P. L., Dressler, A., Egami, E., & Rix, H.-W. 2004, AJ, 127, 2617
Morgan, C. W., Kochanek, C. S., Dai, X., Morgan, N. D., & Falco, E. E. 2008, ApJ, 689, 755
Morgan, C. W., Kochanek, C. S., Morgan, N. D., & Falco, E. E. 2007, arXiv:0707.0305
Muñoz, J. A., Falco, E. E., Kochanek, C. S., McLeod, B. A., & Mediavilla, E. 2004, ApJ, 605, 614
Navarro, J. F., Frenk, C. S., & White, S. D. M. 1996, ApJ, 462, 563
Oguri, M., et al. 2005, ApJ, 622, 106
Ota, N., et al. 2006, ApJ, 647, 215
Paczynski, B. 1986, ApJ, 304, 1
Poindexter, S., Morgan, N., Kochanek, C. S., & Falco, E. E. 2007, ApJ, 660, 146

Pooley, D., Blackburne, J. A., Rappaport, S., & Schechter, P. L. 2007, ApJ, 661, 19
Pooley, D., Rappaport, S., Blackburne, J., Schechter, P. L., Schwab, J., & Wambsganss, J. 2009, ApJ, 697, 1892
Popović, L. Č., & Chartas, G. 2005, MNRAS, 357, 135
Ross, N. R., Assef, R. J., Kochanek, C. S., Falco, E., & Poindexter, S. D. 2009, ApJ, 702, 472
Schechter, P. L., Gregg, M. D., Becker, R. H., Helfand, D. J., & White, R. L. 1998, AJ, 115, 1371
Schechter, P. L., & Wambsganss, J. 2002, ApJ, 580, 685
Schechter, P. L., & Wambsganss, J. 2004, in IAU Symp. 220, Dark Matter in Galaxies, ed. S. D. Ryder et al. (San Francisco, CA: ASP), 103
Schneider, P., Ehlers, J., & Falco, E. E. 1992, Gravitational Lenses, Vol. XIV (Berlin: Springer/Astronomy and Astrophysics Library), 560
Shalyapin, V. N., Goicoechea, L. J., Alcalde, D., Mediavilla, E., Muñoz, J. A., & Gil-Merino, R. 2002, ApJ, 579, 127
Sluse, D., Claeskens, J.-F., Hutsemékers, D., & Surdej, J. 2007, A&A, 468, 885
Sluse, D., et al. 2006, A&A, 449, 539
Surdej, J., Claeskens, J.-F., Remy, M., Refsdal, S., Pirenne, B., Prieto, A., & Vanderriest, C. 1997, A&A, 327, L1
Tisserand, P., et al. 2007, A&A, 469, 387
Wambsganss, J. 2006, Gravitational Lensing: Strong, Weak and Micro, Saas-Fee Advanced Courses, Vol. 33 (Berlin: Springer), 453
Webster, R. L., Ferguson, A. M. N., Corrigan, R. T., & Irwin, M. J. 1991, AJ, 102, 1939
Wisotzki, L., Becker, T., Christensen, L., Helms, A., Jahnke, K., Kelz, A., Roth, M. M., & Sanchez, S. F. 2003, A&A, 408, 455
Wisotzki, L., Koehler, T., Kayser, R., & Reimers, D. 1993, A&A, 278, L15
Wisotzki, L., Schechter, P. L., Chen, H.-W., Richstone, D., Jahnke, K., Sánchez, S. F., & Reimers, D. 2004, A&A, 419, L31
Witt, H. J., Mao, S., & Schechter, P. L. 1995, ApJ, 443, 18
Wucknitz, O., Wisotzki, L., Lopez, S., & Gregg, M. D. 2003, A&A, 405, 445
Wyrzykowski, L., et al. 2009, MNRAS, 397, 1228

5

The Structure of the Accretion Disk in the Lensed Quasar SBS 0909+532

5.1 Introduction

The continuum quasar emission arised from the center of the quasar structure. That region is modeled by a thin accretion disk (Shakura & Sunyaev 1973). The potential gravitational energy released by the accreting material is thermalized in the accretion disk and radiated away. When a Plank distribution is assumed for the local radiating spectrum, a radial dependence $T \propto R^{\frac{1}{p}}$ is obtained for the disk, with $p = \frac{3}{4}$. Therefore, the bluer (inner) part must undergo a higher microlensing magnification because of its smaller size.

The quantity to check against the narrow lines flux quotients was the flux quotient of the underlying local continua as in Mediavilla et al. 2009, but here the study was conducted on a single object, SBS 0909+532 for which the available spectra covered a very large wavelength range with a reasonable good Signal to Noise ratio, ideal to study microlensing chromaticity. It was possible to extract differential microlensing measures for 14 different emission lines across a composite spectrum spanning from the UV, well into the NIR, thus mapping a wavelength dependency of the signal.

These 14 measures were averaged in three groups. The likelihood of each of the three values was analyzed separately, departing from simulated magnification maps

convolved with 2-dimensional Gaussian functions to account for different source sizes.

This lead to an estimate of the emitting region size in different wavelengths, that was roughly in agreement with the thin disk theory with a central black hole mass of $2 \times 10^9 M_\odot$.

Note that in lensed quasars in general, the continuum flux ratio alone may or may not present a wavelength dependence. If the line flux ratios follow the same trend (thus resulting in a wavelength-independent microlensing signal) this is merely due to extinction by the lens galaxy halo. Some examples are shown in figure 5.1.

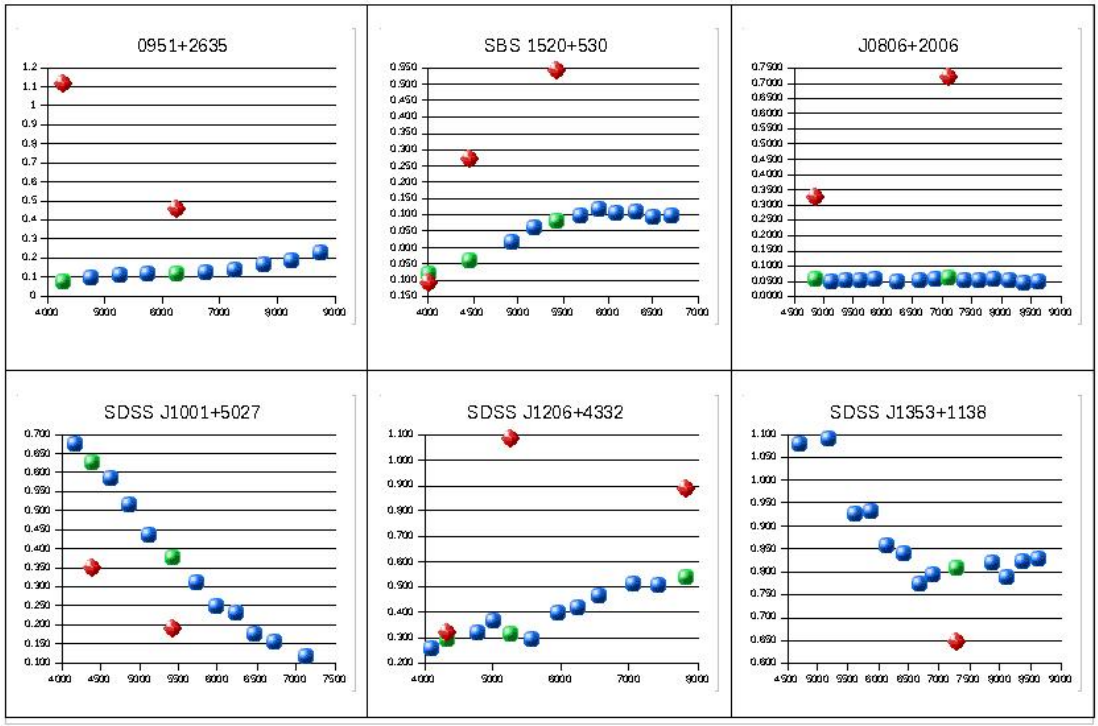

Figure 5.1: Continuum (blue/green) and line (red) flux ratios for several lensed quasars. Note that J1001+5027 has a strong wavelength dependence of the continuum flux quotient, but that does NOT imply chromaticity for the microlensing signal, since the difference between the lines and continuum remains nearly constant. Detecting such chromaticity with a few lines per object leads to noisy results, but with 14 lines measured, much more can be done (*This sample belongs to a preliminary exploration prior to the measures for Mediavilla et al. 2009*).

5. THE STRUCTURE OF THE ACCRETION DISK IN THE LENSED QUASAR SBS 0909+532

5.2 Mediavilla et al. 2011

5. THE STRUCTURE OF THE ACCRETION DISK IN THE LENSED QUASAR SBS 0909+532

The Astrophysical Journal, 730:16 (7pp), 2011 March 20 doi:10.1088/0004-637X/730/1/16

THE STRUCTURE OF THE ACCRETION DISK IN THE LENSED QUASAR SBS 0909+532

E. Mediavilla[1,2], J. A. Muñoz[3], C. S. Kochanek[4], E. Guerras[1,2], J. Acosta-Pulido[1,2], E. Falco[5], V. Motta[6], S. Arribas[7], A. Manchado[1,2], and A. Mosquera[3,4]

[1] Instituto de Astrofísica de Canarias, Vía Láctea S/N, La Laguna 38200, Tenerife, Spain
[2] Departamento de Astrofísica, Universidad de la Laguna, La Laguna 38200, Tenerife, Spain
[3] Departamento de Astronomía y Astrofísica, Universidad de Valencia, 46100 Burjassot, Valencia, Spain
[4] Department of Astronomy and the Center for Cosmology and Astroparticle Physics, The Ohio State University, 4055 McPherson Lab, 140 West 18th Avenue, Columbus, OH 43221, USA
[5] Center for Astrophysics, 60 Garden Street, Cambridge, MA 02138, USA
[6] Universidad de Valparaíso, Avda. Gran Bretaña 1111, Playa Ancha, Valparaíso, Chile
[7] Departamento de Astrofísica, Centro de Astrobiología (CSIC-INTA), Crta. Ajalvir Km. 4, 28850 Torrejon de Ardoz, Madrid, Spain
Received 2010 August 30; accepted 2011 January 14; published 2011 February 24

ABSTRACT

We derive the size and temperature profile of the accretion disk of the lensed quasar SBS 0909+532 by measuring the wavelength dependence (chromaticity) of the microlensing magnification produced by the stars in the lens galaxy. After correcting for extinction using the flux ratios of 14 emission lines, we observe a marked change in the B–A flux ratio with wavelength, varying from -0.67 ± 0.05 mag at (rest frame) ~1460 Å to -0.24 ± 0.07 mag at ~6560 Å. For $\lambda \gtrsim 7000$ Å both effects, extinction and microlensing, look minimal. Simulations indicate that image B rather than A is strongly microlensed. If we model the change in disk size from 1460 Å to 6560 Å using a Gaussian source ($I \propto \exp(-R^2/2r_s^2)$) with a disk size scaling with wavelength as $r_s \propto \lambda^p$, we find $r_s = 7^{+5}_{-3}$ light-days at 1460 Å and $p = 0.9^{+0.6}_{-0.3}$ for uniform priors on r_s and p, and $r_s = 4^{+3}_{-3}$ light-days and $p = 1.0^{+0.6}_{-0.4}$ for a logarithmic prior on r_s. The disk temperature profile $T \propto R^{-1/p}$ is consistent with thin disk theory ($T \propto R^{-3/4}$), given the uncertainties. The estimates of r_s are also in agreement with the size inferred from thin disk theory using the estimated black hole mass ($M_{\rm BH} \simeq 2 \times 10^9\, M_\odot$) but not with the smaller size estimated from thin disk theory and the optical flux. We also use the flux ratios of the unmicrolensed emission lines to determine the extinction curve of the dust in the lens galaxy, finding that it is similar to that of the LMC2 Supershell.

Key words: dust, extinction – gravitational lensing: micro – quasars: individual (SBS 0909+532)

1. INTRODUCTION

The high efficiency with which active galactic nuclei (AGNs) and quasars generate energy leads almost inescapably to the existence of a mechanism for transferring matter into the deep gravitational well of a supermassive black hole (Zel'dovich 1964; Salpeter 1964). A simple, commonly used model based on this hypothesis is the thin accretion disk model (Shakura & Sunyaev 1973), which predicts, among other physical parameters of interest, the size of the disk and the radial dependence of its surface temperature. Observational studies of the accreting region to test these predictions are, unfortunately, very limited due to the small angular size of accretion disks. Until recently, most observational studies relied on indirect evidence based on variability (see, e.g., Sergeev et al. 2005) or models of spectral energy distributions (SEDs; see Bonning et al. 2007 and references therein). The detection of extremely broad FeKα X-ray emission lines in a few AGNs and quasars opened a more direct approach to the study of the inner region of the accreting disk and its potentially exotic physics (Fabian 2005), but the observations are very challenging.

Multiply imaged quasars offer at least two ways to resolve the accretion structure using the microlensing of the disk by the stars in the lens galaxy (quasar microlensing; Chang & Refsdal 1979; see also the review by Wambsganss 2006). The first is through time variability, using the amplitude and rate of the variability to constrain the disk size (Rauch & Blandford 1991; Jaroszynski et al. 1992; Yonehara et al. 1998). With this approach, the challenge is obtaining the necessary monitoring data, but given the data there is a well-established analysis method (Kochanek 2004). Disk size measurements based on variability are now routine (e.g., Morgan et al. 2010) and can even be used to study disk inclinations (Poindexter & Kochanek 2010). The second approach is through the wavelength dependence of the microlensing. If, as predicted by the thin disk model, the size of the emitting region varies with wavelength, then the microlensing magnification should be wavelength dependent. Measuring the SED of the lensed images at a single epoch can reveal this microlensing "chromaticity" and by modeling it both the size and the temperature profile of the source can be constrained. Many recent studies have used this approach (Pooley et al. 2007; Anguita et al. 2008; Agol et al. 2009; Bate et al. 2008; Floyd et al. 2009; Blackburne et al. 2010), although care is required to distinguish between microlensing chromaticity and differential extinction. This can be done relatively easily by using the unmicrolensed emission line flux ratios to determine the extinction and then correct the continuum flux ratios before carrying out the microlensing analysis (see, e.g., Mediavilla et al. 2009). The two approaches can also be combined, as in the studies by Poindexter et al. (2008), Morgan et al. (2008), or Dai et al. (2010).

There are not many studies of microlensing chromaticity based on the measurements of the offsets between the continuum and emission line flux ratios. In HE 1104−1805, Wisotzki et al. (1993, 1995) found that the continuum flux ratio between the two images depended on wavelength but the flux ratios were approximately constant for the emission lines. In HE 0512−3329, Wucknitz et al. (2003) used the emission lines to separate the extinction and microlensing-induced chromaticities. In Q 2237+0305, Mosquera et al. (2009) used narrowband imaging

rather than spectroscopy to separate the emission lines from the continuum and detected chromatic microlensing in image A. In the two-image lens SBS 0909+532 ($z_l = 0.83$, $z_s = 1.38$) we had previously noticed the different flux ratios in the lines and continuum (Motta et al. 2002, also see Oscoz et al. 1997) and in Mediavilla et al. (2005) we found that these differences continued into the ultraviolet (UV). Here we extend these results into the near-IR and combine them to determine both the structure of the accretion disk and the extinction law of the dust in the lens galaxy. The paper is organized as follows. In Section 2 we present the new IR data and derive the magnitude differences (created by microlensing and extinction) as a function of wavelength. In Sections 3.1 and 3.2 we use the effects of microlensing to study the structure of the accretion disk, and in Section 3.3 we determine the extinction curve of the dust in the lens galaxy using the parameterization of Fitzpatrick & Massa (1990). Finally, in Section 4 we summarize the main conclusions.

2. DATA

We obtained near-IR spectra using the LIRIS instrument mounted on the 4.2 m William Herschel Telescope (WHT) at the Observatorio del Roque de los Muchachos on the nights of 2004 March 5 and 2005 January 22, as part of the LIRIS Guaranteed Time program. LIRIS is an infrared camera/spectrograph built at the Instituto de Astrofisica de Canarias (Manchado et al. 2004). In 2004 March we obtained a spectrum using the ZJ grism (0.9–1.5 μm and R 500), a slit width of 1.″0, and a total exposure time of 2000 s split into four exposures of 500 s each. In 2005 January we obtained a spectrum using the HK grism (1.5–2.4 μm and R 650), a slit width of 0.″75, and a total exposure time of 1800 s split into six exposures of 300 s each. Both observations were performed using an ABBA telescope nodding pattern and with the slit oriented at the position angle (PA) defined by the two quasar images. The measurements were taken using multiple correlated readout mode, including four readouts before and after the integration to reduce the readout noise. The nearby A2 star HD 784888 was observed with the same configuration to make the telluric corrections and for flux calibration.

The data were reduced and calibrated using the package "lirisdr," developed by the LIRIS team within the IRAF environment. Consecutive pairs of AB frames were subtracted to remove the sky background, then the resulting images were wavelength calibrated and flat-fielded. All resulting frames were registered and co-added to provide the final combined spectrum. Then, the one-dimensional spectra of the two quasar images were extracted and divided by a composite spectrum to remove telluric absorption. This composite spectrum was generated from the observed spectra of the calibration star, divided by a stellar model of the same spectral type that was smoothed to our spectral resolution.

We merged these near-IR spectra with the UV and optical spectra from our earlier studies. The optical spectrum was obtained with the fiber system *INTEGRAL* (Arribas et al. 1998) at the WHT on 2001 January 18 (Motta et al. 2002) and the UV spectrum was obtained with Space Telescope Imaging Spectrograph (STIS) on the *Hubble Space Telescope* (*HST*) on 2003 March 7 (Mediavilla et al. 2005). We merged the previously joined optical/UV composite spectrum to the new Z/J-band spectra using the overlap at 8958–9245 Å. The normalization factors were 1.00 ± 0.02 and 0.91 ± 0.02 for the A and B components, respectively. There is no direct overlap of the H/K spectra with the other data, so we fit a power law

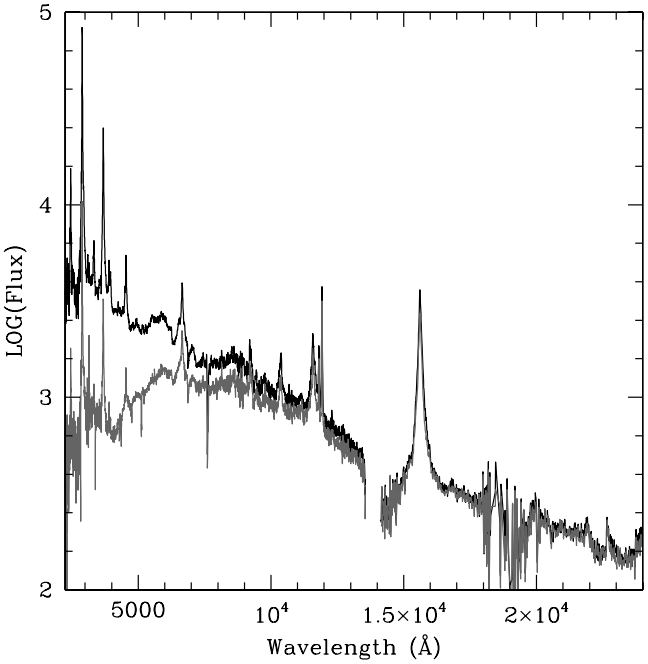

Figure 1. STIS+INTEGRAL+LIRIS spectra corresponding to A (black) and B (gray) images of SBS 0909+532. The flux scale is in arbitrary units.

to the A spectrum in the wavelength range ~8000–12900 Å, and used its extrapolation to match the H/K spectrum in the wavelength range ~18200–22900 Å. The merged spectrum is shown in Figure 1. Note the prominent Hα + [N II] blend in the H band.

Figure 2 shows the flux ratio between the spectra of the two quasar images as a magnitude difference, where we have smoothed the spectrum with a Gaussian filter of $\sigma = 1.5$ Å to reduce the noise fluctuations. We clearly see significant differences between the continuum and emission line regions, particularly in the UV. To separate the two emission components we subtracted a linear model for the continuum from each emission line, determined by fits to the continuum regions adjacent to each emission line, and measured an average line flux ratio. Away from the lines we smoothed the continuum in intervals of roughly 400 Å, to estimate the continuum flux ratios. These line and continuum flux ratios are also shown in Figure 2, and we clearly see the significant offsets between the continuum and emission lines created by microlensing, as we had previously noted in Motta et al. (2002) and Mediavilla et al. (2005), and that the offset steadily decreases as we approach the near-IR.

For comparison we show the B, V, R, I, and H broadband magnitude differences from Kochanek et al. (1997) and Lehár et al. (2000). The general agreement of these flux ratios with the spectroscopic results despite the significant time separations suggests that we need worry little about the time variability created by microlensing in merging the optical, UV, and near-IR spectra. We also note that the time delay in SBS 0909+532 should be short enough (Lehár et al. 2000) that we need not be concerned about intrinsic variability modulated by the time delay contaminating the flux ratios. Unfortunately, we have no tests for these effects at the shortest wavelengths.

To isolate the microlensing effects we measure the offsets between the continuum and line flux ratios, $\Delta m = (m_B - m_A)_{con} - (m_B - m_A)_{lin}$. This is based on the assumption

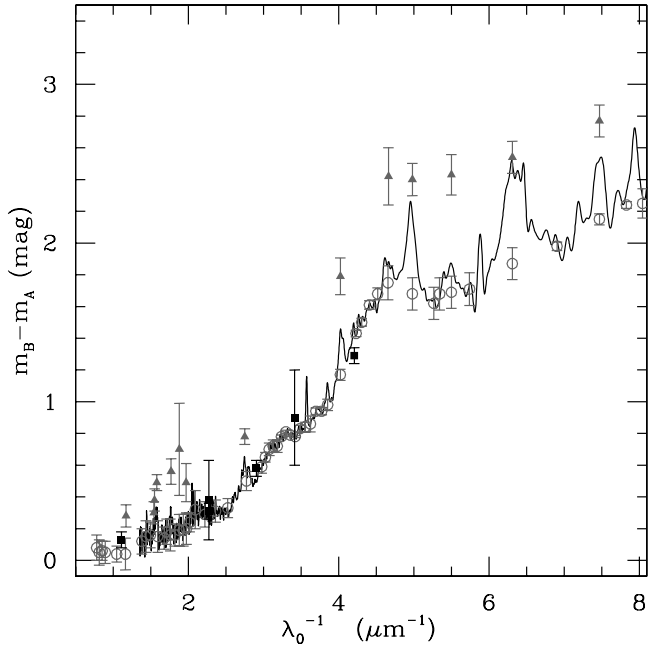

Figure 2. Continuous curve shows the magnitude difference of the merged STIS+INTEGRAL+LIRIS spectra. Gray circles (continuum) and triangles (emission line) correspond to integrated magnitude differences (see the text). Black squares correspond to broadband photometry from the literature (see the text).

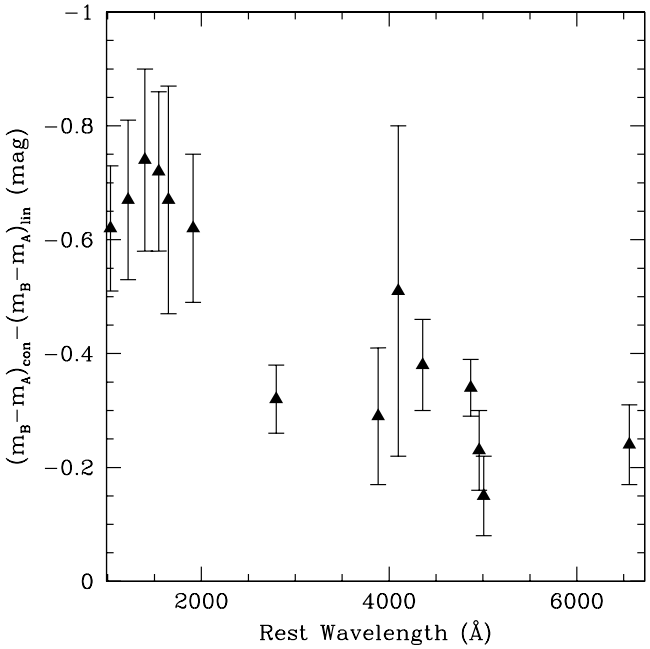

Figure 3. Wavelength dependence of the difference between the continuum and emission line flux ratios for the (from blue to red) Lyβ, Lyα, Si IV + O IV], C IV, He II + O III], C III], Mg II, He I, Hδ, Hγ, Hβ, [O III]λ4959, [O III]λ5007, and Hα + [N II] emission lines.

that the emission line regions are much larger than the regions that can be significantly microlensed.[8] Figure 3 shows the estimates of Δm associated with each of the emission lines (Lyβ, Lyα, Si IV + O IV], C IV, He II + O III], C III], Mg II, He I, Hδ, Hγ, Hβ, [O III]λ4959, [O III]λ5007, and Hα + [N II]; from blue to red). We see that Δm shifts with wavelength. B is considerably brighter in the UV but becomes comparable to A in the optical/near-IR, with a chromatic change of $\sim$0.5 magnitudes between the amplitude at 6600 Å and 1500 Å. Note that the offset remains even at the wavelength of Hα.

In principle, we may use the 14 data points in Figure 3 in our posterior simulations. However, this would imply a huge computational effort that is not justified by the uncertainties. To quantify the dependence of the microlensing amplitude on wavelength, we will take an average value from the six bluest emission lines,

$$\Delta m_1^{\rm obs}(\lambda_1 \sim 1459 \pm 314\ \text{Å}) = -0.67 \pm 0.05, \quad (1)$$

an intermediate value corresponding to the average of the microlensing amplitudes associated with the seven intermediate wavelength emission lines,

$$\Delta m_2^{\rm obs}(\lambda_2 \sim 4281 \pm 789\ \text{Å}) = -0.30 \pm 0.10, \quad (2)$$

and the value associated with the reddest emission line:

$$\Delta m_3^{\rm obs}(\lambda_3 \sim 6559\ \text{Å}) = -0.24 \pm 0.07. \quad (3)$$

The uncertainties in the averaged wavelengths are the rms dispersions.

[8] No significant microlensing magnification is expected for the narrow emission lines and for the low ionization broad emission lines, especially if the lensed source is a bright quasar. However, microlensing could affect the high ionization broad lines of low-luminosity AGNs (Abajas et al. 2002).

3. DISCUSSION

3.1. Microlensing and the Structure of the Accretion Disk

We model the accretion disk as a Gaussian intensity profile $I(R) \propto \exp(-R^2/2r_s^2)$ characterized by a wavelength-dependent size r_s. By randomly placing such a source on microlensing magnification maps corresponding to the A and B images of SBS 0909+532, we can estimate the probability of reproducing the flux ratios measured in Section 2 ($\Delta m_l^{\rm obs}(\lambda_l)$, $l = 1, 2, 3$). The model depends on seven parameters: the convergence and shear corresponding to each image (κ_A, γ_A, κ_B, γ_B), the mass fraction in microlenses (α), the accretion disk size at 1459 Å (r_s), and the power-law index (p) relating the disk sizes at different wavelengths ($r_s(\lambda) \propto \lambda^p$).

The four macrolens parameters (κ_A, γ_A, κ_B, γ_B) are fixed by a simple, standard model of the lens system. We used a singular isothermal sphere (SIS) in an external shear field to fit the relative separations of the two lensed images and the lens galaxy, using the CASTLES[9] *HST* astrometry. In general, it is risky to constrain models with flux ratios because of the combined effects of microlensing, substructure, and extinction (Kochanek 2006), but here with our large wavelength coverage (Figures 1 and 2) these effects are minimal for (rest-frame) wavelengths $\lambda \gtrsim 7000$ Å, so averaging in this region the continuum magnitudes difference we adopt a flux ratio constraint of $m_B - m_A = 0.05 \pm 0.05$ mag. The resulting values for the convergence and shear at the locations of the images are $(\kappa_A, \gamma_A) = (0.66, 0.70)$ and $(\kappa_B, \gamma_B) = (0.36, 0.25)$. We then considered models in which a fraction $\alpha = 2^{-i}$ with $i = 0, \ldots, 6$ of the surface density is comprised of stars and the remainder is smoothly distributed dark matter. All stars were given a common mass of $M = M_\odot$. From the source $z_s = 1.38$ and lens $z_l = 0.83$ redshifts the source plane Einstein radius is

[9] Cfa-Arizona Space Telescope LEns Survey (www.cfa.harvard.edu/castles/).

$R_E = 3.3 \times 10^{16}(M/M_\odot)^{1/2}$ cm (=12.6$(M/M_\odot)^{1/2}$ light-days) for an $\Omega_0 = 0.3, \Lambda_0 = 0.7, h = 0.7$ flat cosmological model. For each value of α_i we compute magnification maps of $80 \times 80\ R_E^2$ (2000×2000 pixels^2) for both images using the Inverse Polygon Method (Mediavilla et al. 2006). We convolved the maps with the Gaussians representing the disk structure. For r_s we consider both a linear grid $r_{sj}(1459\ \text{Å}) = 1, 2, \ldots, 30$ light-days and a logarithmic grid $\log r_{sj}(1459\ \text{Å}) = ((\log 30)/29) \cdot (j-1)$ light-days ($j = 1, 2, \ldots, 30$) better suited for the use of a logarithmic prior. For p we consider the linear grid $p_k = 0.0, 0.1, \ldots, 2.1$. Thus, the size at λ_l is $r_{sjk}(\lambda_l) = r_{sj}(1459\ \text{Å})(\lambda_l/1459\ \text{Å})^{p_k}$. After convolution we normalized each $\mu_{ijklA,B}$ magnification map by its mean value so that the difference magnification maps (expressed in magnitudes)

$$\Delta\mu_{ijkl} = \mu_{ijklA} - \mu_{ijklB} \tag{4}$$

determine the relative microlensing magnifications of images A and B. For each case, we randomly sample the patterns to build a histogram of events $N_{ijk}(\Delta m_1, \Delta m_2, \Delta m_3)$. We calculate 4620 histograms with 10^8 events in each. The probability of the data given the model is then

$$p\left(\Delta m_1^{\rm obs}, \Delta m_2^{\rm obs}, \Delta m_3^{\rm obs} \middle| \alpha_i, r_{sj}, p_k\right) \propto \int d\Delta m_1 \int d\Delta m_2 \int d\Delta m_3 N_{ijk} e^{-\frac{1}{2}\chi^2}, \tag{5}$$

where

$$\chi^2 = \sum_{l=1}^{3} \frac{\left(\Delta m_l - \Delta m_l^{\rm obs}\right)^2}{\sigma^2_{\Delta m_l^{\rm obs}}}. \tag{6}$$

We find many cases with statistically acceptable values for χ^2, and the results do not change significantly if we restrict the calculations in Equation (5) to cases with $\chi^2 < 3$.

Using Bayes' theorem, the probability of the parameters given the data is then

$$p\left(\alpha_i, r_{sj}, p_k \middle| \Delta m_1^{\rm obs}, \Delta m_2^{\rm obs}, \Delta m_3^{\rm obs}\right) \propto p\left(\Delta m_1^{\rm obs}, \Delta m_2^{\rm obs}, \Delta m_3^{\rm obs} \middle| \alpha_i, r_{sj}, p_k\right) p(\alpha_i, r_{sj}, p_k), \tag{7}$$

where $p(\alpha_i, r_{sj}, p_k)$ represents the priors on the model parameters and the overall normalization is such that $\sum_{ijk} p(\alpha_i, r_{sj}, p_k | \Delta m_1^{\rm obs}, \Delta m_2^{\rm obs}, \Delta m_3^{\rm obs}) \equiv 1$.

The present data do not constrain the stellar mass fraction, α. Fortunately, the estimates of the disk structure are little affected by this for reasonable values of $\alpha \lesssim 0.3$. In any case, we used as a prior for α the likelihood function $L(\alpha)$ derived by Mediavilla et al. (2009) from a statistical survey of microlensing in quasars, which favors low stellar mass fractions, $0.02 \lesssim \alpha \lesssim 0.14$, as might be expected in the region near the lensed images. To analyze the sensitivity of our study to the treatment of the size prior (see Morgan et al. 2010), we have considered two priors, linear and logarithmic, for r_s.

Summing on α_i we obtain the marginalized probability density function for r_s and p,

$$p\left(r_{sj}, p_k \middle| \Delta m_1^{\rm obs}, \Delta m_2^{\rm obs}, \Delta m_3^{\rm obs}\right) = \sum_i p\left(\alpha_i, r_{sj}, p_k \middle| \Delta m_1^{\rm obs}, \Delta m_2^{\rm obs}, \Delta m_3^{\rm obs}\right). \tag{8}$$

In Figure 4, we show this marginalized probability density function for both linear and logarithmic grids in r_s. There is an (anti-)covariance (more marked in the plot with a logarithmic grid in r_s) between r_s and p. Note that the computation of an expected value or confidence interval integrating on dr_s ($d \log r_s$) will be equivalent to the use of a linear (logarithmic) prior. We obtain estimates for the source parameters of $r_s(1459\ \text{Å}) = 8^{+5}_{-4}$ light-days, $p = 0.9^{+0.6}_{-0.3}$ and $r_s(1459\ \text{Å}) = 5^{+4}_{-3}$ light-days, $p = 1.0^{+0.6}_{-0.4}$ for the linear and logarithmic priors, respectively. As far as there are not a priori reasons to prefer one or other prior, the difference between the two estimates for r_s should be regarded as a test of the sensitivity of the method to the prior.

Microlensing magnification patterns can be qualitatively described by a series of complex high magnification ridges of caustics separated by relatively smooth valleys of demagnification. If we examine the origin of the chromaticity in detail for the case $\alpha = 0.125$, $p = 0.8$, and $r_s = 8$ light-days, we find that they are generally (90%) due to image B lying close to a caustic with A in a relatively smooth region of the magnification patterns rather than the reverse or having both images lying either in ridges or valleys.

3.2. Comparison with the Standard Thin Disk Model

The radial dependence of the surface temperature in the accretion disk is obtained equating the local radiation energy flux to the gravitational energy release (Shakura & Sunyaev 1973). When the local spectrum of the thermal radiation is a Planck distribution, a $T \propto R^{-\beta}$ law with $\beta = 3/4$ is obtained. Defining the radius at which the disk temperature matches the wavelength, R_λ, from $kT(R_\lambda) = hc/\lambda$, a size scaling $R_\lambda \propto \lambda^p$ with $p = 1/\beta = 4/3$ is derived. From our microlensing data we derive a compatible estimate, $p = 0.9^{+0.6}_{-0.3}$. Excepting Floyd et al. (2009; see also Blackburne et al. 2010), other microlensing estimates based on multi-band observations (Eigenbrod et al. 2008; Poindexter et al. 2008; Anguita et al. 2008; Bate et al. 2008; Mosquera et al. 2009) are also compatible with the $T \propto R^{-3/4}$ law within their uncertainties (see Floyd et al. 2009; Morgan et al. 2010).

The energy condition locally equating blackbody radiation and gravitational energy release provides an estimate of R_λ (Shakura & Sunyaev 1973),

$$R_\lambda = 9.7 \times 10^{15} \left(\frac{\lambda}{\mu\text{m}}\right)^{4/3} \left(\frac{M_{\rm BH}}{10^9\ M_\odot}\right)^{2/3} \left(\frac{L}{\eta L_E}\right)^{1/3} \text{cm}, \tag{9}$$

where η is the radiative efficiency, $L = \eta \dot{M} c^2$ is the luminosity, and L_E is the Eddington luminosity. In our case, $\lambda_{\rm rest} = 1500$ Å. Based on the Mg II line, Peng et al. (2006) estimated a black hole mass of $M_{\rm BH} \simeq 10^{9.59}\ M_\odot$ while based on the C IV, Hβ, and Hα lines, Assef et al. (2010) estimate masses of $10^{8.51}$, $10^{9.29}$, and $10^{9.15}\ M_\odot$, respectively. The difference between the C IV and Hβ estimates is largely explained by the correlation of the mass differences with the UV/optical spectral slope discovered in that paper. Adopting the Hβ mass estimate, $L/L_E \sim 1$ and $\eta \sim 0.1$, the estimated radius enclosing half of the luminosity is $R_{1/2} = 2.44 R_\lambda = 2.4$ light-days. This result assumes $\beta = 3/4$ ($p = 4/3$). We lack an alternative disk model with $p \sim 1$, so we cannot generalize Equation (9) to this case. If we fix $p = 4/3$ in our simulations, we find sizes of $R_{1/2} = 1.18 r_s = 6^{+4}_{-2}$ light-days (linear prior) and $R_{1/2} = 4^{+3}_{-2}$ light-days (logarithmic prior) in agreement with the estimate derived from Equation (9) given the uncertainties.

On the other hand, we can also estimate R_λ from the observed flux at some wavelength, F_ν. The luminosity of the accretion disk at wavelength λ can be obtained integrating the local

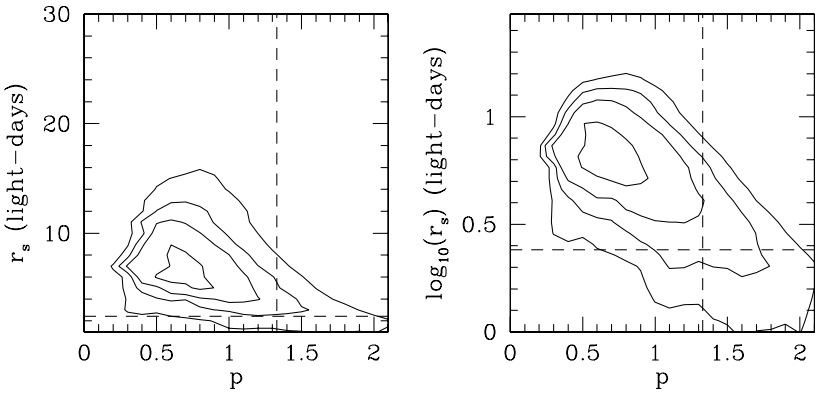

Figure 4. Probability density functions for the linear (left) and logarithmic (right) size priors. Contours correspond to 15%, 47%, 68%, and 90% of enclosed probability. Vertical dashed lines correspond to the thin disk theoretical value for the scaling index ($p = 1/\beta = 4/3$). Horizontal dashed lines correspond to the size inferred from thin disk theory using the estimated black hole mass (see the text).

spectrum of the radiation, $f_\nu(T(R))$, over radius,

$$L_\nu = \int_0^\infty f_\nu(T(R))2\pi R(\cos i)dR, \tag{10}$$

where i is the disk inclination. When f_ν is the Planck spectrum and $T \propto R^{-3/4}$, we obtain

$$R_\lambda = \sqrt{\frac{3/4}{\Gamma(\frac{8}{3})\zeta(\frac{8}{3})}}\sqrt{\frac{1}{hc}}\sqrt{\frac{1}{\cos i}}D_{\rm OS}\lambda_{\rm obs}^{3/2}\sqrt{F_\nu}, \tag{11}$$

where Γ and ζ are the Gamma and Riemann ζ functions and $D_{\rm OS}$ is the angular distance between observer and source. For the I band this implies

$$R_\lambda = 2.83\times10^{15}\sqrt{\frac{1}{\cos i}}\frac{D_{\rm OS}}{r_H}\left(\frac{\lambda_{\rm obs}}{\mu{\rm m}}\right)^{3/2}10^{-0.2(I_0-19)}h^{-1}\,{\rm cm} \tag{12}$$

(Morgan et al. 2008; Dai et al. 2010), where r_H is the Hubble radius ($r_H = c/H_0$), $\lambda_{\rm obs}$ is the observed wavelength (0.814 μm for the I filter), and I_0 is the intrinsic flux (in magnitudes) at $\lambda_{\rm obs}$. Here we must estimate the source flux, I_0, in the presence of high extinction and microlensing. For a double lens like SBS 0909+532, two equations can be written to derive I_0,

$$I_0 = I_{\rm A} - \mu_{\rm A} - A_{\rm A} - \Delta\mu_{\rm A} \tag{13}$$

and

$$I_0 = I_{\rm B} - \mu_{\rm B} - A_{\rm B} - \Delta\mu_{\rm B}, \tag{14}$$

where $I_{\rm A,B}$, $\mu_{\rm A,B}$, $A_{\rm A,B}$, and $\Delta\mu_{\rm A,B}$ are the observed fluxes (in magnitudes), the macrolens magnifications, the extinctions, and the microlensing magnifications for each image of the quasar. From CASTLES we obtain $I_{\rm A} = 16.23$ and $I_{\rm B} = 16.61$. The macrolens magnifications inferred from our SIS+γ model are $\mu_{\rm A} = \mu_{\rm B} = -1.14$. From the emission line ratio at 0.814 μm (see Figure 2) we infer $A_{\rm B} - A_{\rm A} = 0.8$. Finally, from the difference between the emission line and continuum ratios at 0.814 μm (Figure 3) we obtain $\Delta\mu_{\rm B} - \Delta\mu_{\rm A} = -0.4$. If we assume (see Figure 1) that there is extinction only for image B ($A_{\rm B} \gg A_{\rm A} \sim 0$) and that B is significantly magnified by microlensing while A suffers little demagnification ($\Delta\mu_{\rm B} \ll \Delta\mu_{\rm A} \sim 0$), then from Equations (13) and (14) we find $I_0 \sim 16.97$ and $I_0 \sim 16.95$ for images A and B, respectively.

Using $I_0 = 16.96$ and $\cos i = 1/2$ in Equation (12), we derive $R_{1/2} = 2.44R_\lambda = 2.9$ light-days for $\lambda_{\rm rest} = 0.342\,\mu$m. If we scale to other wavelengths assuming $p = 4/3$, we find $R_{1/2} = 0.95$ light-days at $\lambda_{\rm rest} = 0.150\,\mu$m. This value is smaller by a factor of ~ 3 than the size based on the black hole mass, $R_{1/2} = 2.4$ light-days (Equation (9)) and smaller than the microlensing size estimates obtained for $p = 4/3$: $R_{1/2} = 6^{+4}_{-2}$ light-days (linear prior) and $R_{1/2} = 4^{+3}_{-2}$ light-days (logarithmic prior). This discrepancy is similar to that found by Pooley et al. (2007), Morgan et al. (2010), and Blackburne et al. (2010). The discrepancies can be reduced by making p substantially larger than 4/3 corresponding to a shallower temperature profile (Poindexter et al. 2008; Morgan et al. 2010). A value $p = 1/\beta \geqslant 2$ is needed to bring the different sizes into agreement within uncertainties. However, the available microlensing estimates (Floyd et al. 2009; Morgan et al. 2010; Blackburne et al. 2010) predict $p \leqslant 1.65$, with an average value (Morgan et al. 2010 and the present work) of $\langle p\rangle = 1.2 \pm 0.3$. In the framework of the thin disk model, the value $\beta = 1/2$ corresponds to the limiting case where local energy generation from accretion plays no role in the heating at a given radius (Gaskell 2008). Although contamination from larger physical scales due to scattering or emission lines could also help to alleviate the flux size problem (Morgan et al. 2010), it is clear that more complex disk models should also be explored. For example, changes from a thermal radiation spectrum would, in general, imply $p \neq 1/\beta$, so $p \sim 1$ would not necessarily imply a temperature profile steeper than 4/3.

3.3. NIR–Optical–FUV Extinction Curve

With the new near-IR spectra, we can also study the NIR–Optical–FUV extragalactic extinction curve with unprecedented wavelength coverage. We do so using the differential extinction between the two images created by their different paths through the lens galaxy (Nadeau et al. 1991). The problem is that microlensing also modifies the continuum slopes. In principle, we could simply fit the differential magnitude curve defined by the emission lines since these are not affected by microlensing. However, the UV bump is poorly constrained because there are few lines in the 2175 Å region. It is preferable to estimate the bump parameters from the continuum data assuming that the impact of the microlensing on this determination is negligible. Thus, we modeled the line and continuum simultaneously, where for the lines (see, e.g., Falco et al. 1999; Muñoz et al. 2004),

$$\Delta m(\lambda_i) = a_0 + \Delta E(B-V)R_{\lambda_i}, \tag{15}$$

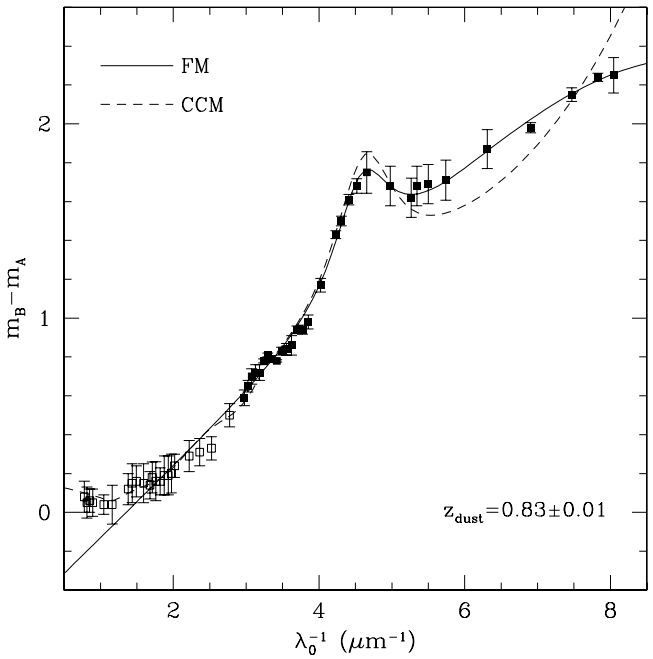

Figure 5. Fitzpatrick & Massa (1990, FM, solid line) and Cardelli et al. (1989, CCM, dashed line) model fits without considering microlensing chromaticity ($b_1 \equiv b_2 \equiv 0$; see the text) to the continuum flux ratios (squares). We have not considered the near-IR data (open squares) to fit the FM model (for it is simply $\propto \lambda^{-1}$ in this region).

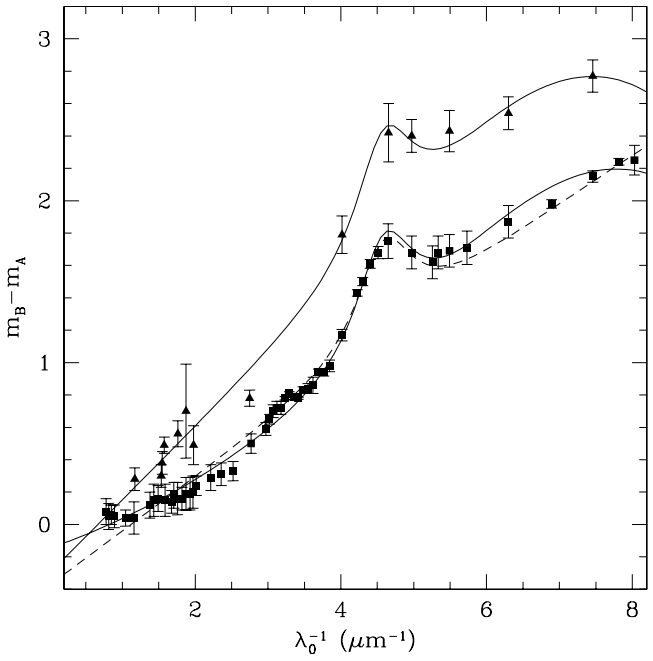

Figure 6. Solid lines: Fitzpatrick & Massa (1990, FM) combined fit to the continuum (squares) and emission lines (triangles) flux ratios using a second order polynomial in λ^{-1} to model the continuum chromaticity induced by microlensing (see the text). A fit using the same model but considering exclusively the continuum data is included for comparison (dashed line).

while for the continuum,

$$\Delta m(\lambda) = b_0 + b_1\lambda^{-1} + b_2\lambda^{-2} + \Delta E(B-V)R_{\lambda_i}, \qquad (16)$$

where the higher order polynomial coefficients b_1 and b_2 should model the observed microlensing chromaticity. We fit the data using the Cardelli et al. (1989, hereafter CCM) and Fitzpatrick & Massa (1990, hereafter FM) multi-parametric models for R_λ.

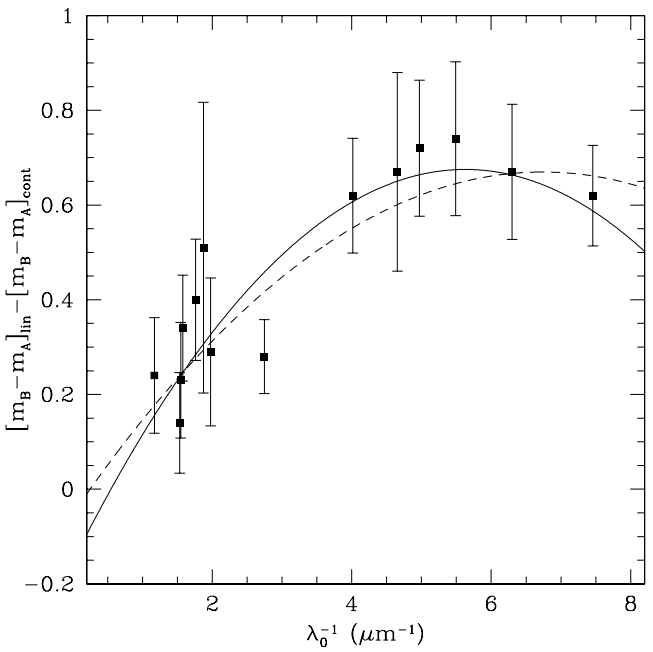

Figure 7. Squares: microlensing magnification data inferred from the ratios between continuum and emission line fluxes. Solid line: ratio between the fits based on the Fitzpatrick & Massa (1990) models with and without microlensing chromaticity (see the text). Dashed line: second order in λ^{-1} polynomial fit to the microlensing magnification data.

The latter model is able to account for the extinction observed in a broader range of environments (see Gordon et al. 2003). Figure 5 shows the results with no chromaticity ($b_1 \equiv b_2 \equiv 0$) and Figure 6 shows the results corresponding to the FM model when the continuum chromaticity is a quadratic function of λ^{-1}. In each case we did the fits both for the dust at the lens redshift ($z_d = z_l = 0.83$) and allowing it to vary. In all the fits the 2175 Å feature is clearly required and the dust redshift estimate $z_d = 0.83 \pm 0.01$ is consistent with the spectroscopic redshift. We find that the CCM model (Figure 5) fails to fit the bump well. As previously noted by Mediavilla et al. (2005), the preferred model is similar to the dust in the LMC2 Supershell. Note, however, that the CCM model is a better fit in the near-IR because in the FM parameterization the extinction is simply λ^{-1} in this region. In Figure 7 we show how the difference between the fits, with and without microlensing chromaticity, follows the microlensing magnification data (a second order polynomial directly fitted to the microlensing data is included in this figure to show the consistency of the procedure).

4. CONCLUSIONS

We have clearly detected chromatic microlensing in SBS 0909+532 by comparing the B/A flux ratios of 14 emission lines and of their underlying continua over a spectral region ranging from the near-IR to the far-UV. The microlensing magnification is highest in the UV (-0.67 ± 0.05 at ~1500 Å) and smoothly diminishes toward the IR (-0.24 ± 0.07 at ~6600 Å). To explain this large chromaticity, image B should be in a region of high magnification, likely crossing or very close to a caustic. This is the case in 90% of our simulations. However, comparison with optical and near-IR (but not UV) broadband data from the literature taken at two different epochs separated by ~9 and ~6 years from our observations shows no significant time variability.

Using a Bayesian analysis we have estimated the disk size, modeled as a Gaussian of dispersion r_s, and the power-law index, p, relating the disk sizes at different wavelengths, $r_s \propto \lambda^p$, needed to explain the observed chromaticity. The estimated half-light radius of 4–8 light-days at $\lambda_{\rm rest} \sim 1500$ Å, depending on the priors, is in reasonable agreement with the size estimated using thin disk theory and the black hole mass estimated from the emission line widths ($R_{1/2} \sim 2.4$ light-days), but not with the smaller size estimated from the optical flux ($R_{1/2} \sim 1$ light-days). The estimate of the size scaling index, $p = 0.9^{+0.6}_{-0.3}$, is compatible with the temperature profile of a thin disk model ($T \propto R^{-3/4} \propto R^{-1/p}$, that is, $p = 4/3$).

The separation of extinction and microlensing effects using the emission line flux ratios is straightforward and consistent and, in any case, microlensing chromaticity does not significantly affect the determination of the dust redshift or the characterization of the 2175 Å bump parameters from the magnitude difference curves. We have used the Fitzpatrick & Massa analytical model to fit the extinction law curve confirming the differences noted by Mediavilla et al. (2005) between the extinction law in the lens galaxy of SBS 0909+532 and that of the Milky Way. The best-fitting extinction curve is similar to that of the LMC2 Supershell.

Based on observations with the NASA/ESA *Hubble Space Telescope*, which is operated by the Association of Universities for Research in Astronomy, Inc., under NASA contract NAS 5-26555. This research was supported by the European Community's Sixth Framework Marie Curie Research Training Network Programme, Contract No. MRTN-CT-2004-505183 "ANGLES," and by the Spanish Ministerio de Educación y Ciencias (grants AYA2004-08243-C03-01/03 and AYA2007-67342-C03-01/03). J.A.M. is also supported by the Generalitat Valenciana with the grant PROMETEO/2009/64. C.S.K. is supported by NSF grants AST-0708082 and AST-1009756. V.M. acknowledges the partial support of grant FONDECYT 1090673. J.A.A.P. and A.M.T. are partially supported by the Spanish MICINN grant AYA2004-03136. A.M.M. acknowledges the support of Generalitat Valenciana, grant APOSTD/2010/030.

REFERENCES

Abajas, C., Mediavilla, E., Muñoz, J. A., Popović, L. Č., & Oscoz, A. 2002, ApJ, 576, 640
Agol, E., Gogarten, S. M., Gorjian, V., & Kimball, A. 2009, ApJ, 697, 1010
Anguita, T., Schmidt, R. W., Turner, E. L., Wambsganss, J., Webster, R. L., Loomis, K. A., Long, D., & McMillan, R. 2008, A&A, 480, 327
Arribas, S., et al. 1998, Proc. SPIE, 3355, 821
Assef, R. J., et al. 2010, ApJ, 713, 970
Bate, N. F., Floyd, D. J. E., Webster, R. L., & Wyithe, J. S. B. 2008, MNRAS, 391, 1955
Blackburne, J. A., Pooley, D., Rappaport, S., & Schechter, P. L. 2010, arXiv:1007.1665
Bonning, E. W., Cheng, L., Shields, G. A., Salviander, S., & Gebhardt, K. 2007, ApJ, 659, 211
Cardelli, J. A., Clayton, G. C., & Mathis, J. S. 1989, ApJ, 345, 245
Chang, K., & Refsdal, S. 1979, Nature, 282, 561
Dai, X., Kochanek, C. S., Chartas, G., Kozłowski, S., Morgan, C. W., Garmire, G., & Agol, E. 2010, ApJ, 709, 278
Eigenbrod, A., Courbin, F., Meylan, G., Agol, E., Anguita, T., Schmidt, R. W., & Wambsganss, J. 2008, A&A, 490, 933
Fabian, A. C. 2005, Ap&SS, 300, 97
Falco, E. E., et al. 1999, ApJ, 523, 617
Fitzpatrick, E. L., & Massa, D. 1990, ApJS, 72, 163
Floyd, D. J. E., Bate, N. F., & Webster, R. L. 2009, MNRAS, 398, 233
Gaskell, C. M. 2008, Rev. Mex. Astron. Astrofis. Conf. Ser., 32, 1
Gordon, K. D., Clayton, G. C., Misselt, K. A., Landolt, A. U., & Wolff, M. J. 2003, ApJ, 594, 279
Jaroszynski, M., Wambsganss, J., & Paczynski, B. 1992, ApJ, 396, L65
Kochanek, C. S. 2004, ApJ, 605, 58
Kochanek, C. S. 2006, in Gravitational Lensing: Strong, Weak and Micro, Saas-Fee Advanced Courses, Vol. 33, ed. G. Meylan, P. Jetzer, & P. North (Berlin: Springer), 91
Kochanek, C. S., Falco, E. E., Schild, R., Dobrzycki, A., Engels, D., & Hagen, H.-J. 1997, ApJ, 479, 678
Lehár, J., et al. 2000, ApJ, 536, 584
Manchado, A., et al. 2004, Proc. SPIE, 5492, 1094
Mediavilla, E., Muñoz, J. A., Kochanek, C. S., Falco, E. E., Arribas, S., & Motta, V. 2005, ApJ, 619, 749
Mediavilla, E., Muñoz, J. A., Lopez, P., Mediavilla, T., Abajas, C., Gonzalez-Morcillo, C., & Gil-Merino, R. 2006, ApJ, 653, 942
Mediavilla, E., et al. 2009, ApJ, 706, 1451
Morgan, C. W., Kochanek, C. S., Dai, X., Morgan, N. D., & Falco, E. E. 2008, ApJ, 689, 755
Morgan, C. W., Kochanek, C. S., Morgan, N. D., & Falco, E. E. 2010, ApJ, 712, 1129
Mosquera, A. M., Muñoz, J. A., & Mediavilla, E. 2009, ApJ, 691, 1292
Motta, V., et al. 2002, ApJ, 574, 719
Muñoz, J. A., Falco, E. E., Kochanek, C. S., McLeod, B. A., & Mediavilla, E. 2004, ApJ, 605, 614
Nadeau, D., Yee, H. K. C., Forrest, W. J., Garnett, J. D., Ninkov, Z., & Pipher, J. L. 1991, ApJ, 376, 430
Oscoz, A., Serra-Ricart, M., Mediavilla, E., Buitrago, J., & Goicoechea, L. J. 1997, ApJ, 491, L7
Peng, C. Y., Impey, C. D., Rix, H.-W., Kochanek, C. S., Keeton, C. R., Falco, E. E., Lehár, J., & McLeod, B. A. 2006, ApJ, 649, 616
Poindexter, S., & Kochanek, C. S. 2010, ApJ, 712, 668
Poindexter, S., Morgan, N., & Kochanek, C. S. 2008, ApJ, 673, 34
Pooley, D., Blackburne, J. A., Rappaport, S., & Schechter, P. L. 2007, ApJ, 661, 19
Rauch, K. P., & Blandford, R. D. 1991, ApJ, 381, L39
Salpeter, E. E. 1964, ApJ, 140, 796
Sergeev, S. G., Doroshenko, V. T., Golubinskiy, Y. V., Merkulova, N. I., & Sergeeva, E. A. 2005, ApJ, 622, 129
Shakura, N. I., & Sunyaev, R. A. 1973, A&A, 24, 337
Wambsganss, J. 2006, in Gravitational Lensing: Strong, Weak and Micro, Saas-Fee Advanced Courses, Vol. 33, ed. G. Meylan, P. Jetzer, & P. North (Berlin: Springer), 453
Wisotzki, L., Koehler, T., Ikonomou, M., & Reimers, D. 1995, A&A, 297, L59
Wisotzki, L., Koehler, T., Kayser, R., & Reimers, D. 1993, A&A, 278, L15
Wucknitz, O., Wisotzki, L., Lopez, S., & Gregg, M. D. 2003, A&A, 405, 445
Yonehara, A., Mineshige, S., Manmoto, T., Fukue, J., Umemura, M., & Turner, E. L. 1998, ApJ, 501, L41
Zel'Dovich, Y. B. 1964, Sov. Phys. Dokl., 9, 195

5. THE STRUCTURE OF THE ACCRETION DISK IN THE LENSED QUASAR SBS 0909+532

6

Constraints on the Broad Line Region Size from Lensed Quasar Spectra

6.1 Introduction

Most of the huge power output of quasars is believed to have its origin in a small region, an accretion disk around a supermassive black hole, surrounded by a bunch of quickly orbiting hot clouds, the *Broad Line Region* (BLR). A much bigger region with slow moving gas (*Narrow Line Region* or NLR) as well as an obscuring torus and the jet are other structures of the standard model. Each of this structures leaves its trace in the spectra of the quasar (see section 1.3).

The time it takes for the central engine flux changes to propagate to the line emitting regions, is the tool reverberation mapping estimates of the BLR size are based upon. But, when the quasar is part of a gravitational lens, there are other ways to extract information about the system. The key is the inverse sensitivity with respect to source size of the microlensing amplification. The outer wings of the emission lines are thought to arise mainly from Doppler broadening of the orbiting BLR clouds emission, a region whose size has been estimated in the order of ~ 100 light-days across by reverberation mapping, thus such broad lines may show signs of microlensing.

To explore this phenomenon qualitatively, we scaled and overimposed each couple of lines after local continuum subtraction. Some of them matched nearly perfectly.

However, some pairs showed notable differences, being SDSS J1004-4112 the object with the most interesting anomaly: all the three lines Ly$_\alpha$ λ1216, Si IV λ1400 and C IV λ1549 present exactly the same enhancement in the blue wings of the brightest component, whereas this feature is absent in the redder C III] λ1909 and Mg II λ2798 lines (see Figure 6.2). This strongly suggest that

- there is substructure in the BLR, so that there may be different regions giving rise to separate sets of lines that will be differently affected by microlensing,
- the BLR is spatially extended enough, so that one part can be crossing a caustic (in this case, the side of the rotating set of clouds that is approaching the observer) while the rest is far enough as to be weakly affected by microlensing.

For our estimation of BLR microlensing, we assume the narrow core of each line to arise mostly from the outer BLR and NLR. Since this region is spatially much more extended than the region contributing to the wings, we set its flux quotient as the baseline value of no microlensing, thus building our estimate for each of the lines as:

$$\Delta M_{BLR} = \Delta M_{wings} - \Delta M_{core} \tag{6.1}$$

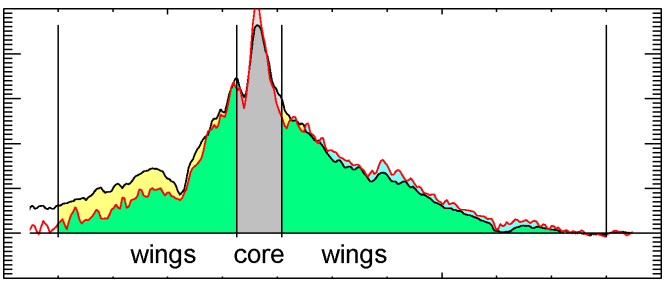

Figure 6.1: After continuum subtraction, the central part of the line and the wings fluxes are measured separately.

Small but significant non-zero values were found for BLR microlensing in nearly all cases. In the samples, 5 out of 18 lensed pairs showed significant differences between microlensing of the high and low ionization and lines (HIL and LIL respectively). HIL are more affected by microlensing. This may be consistent with a more compact origin region for the HIL emission region inside the BLR.

Using the core emission as a baseline of no-microlensing (which is an approximation, since there is some contamination from zero line-of-sight projected velocity BLR clouds - see Figure 6.1), we did a maximum likelihood comparison with sets of computer-generated histograms, following a similar procedure as in Mediavilla et al. 2009 . We obtained estimates for the size of the Broad Line Region, that are compatible with the previous results from reverberation mapping studies.

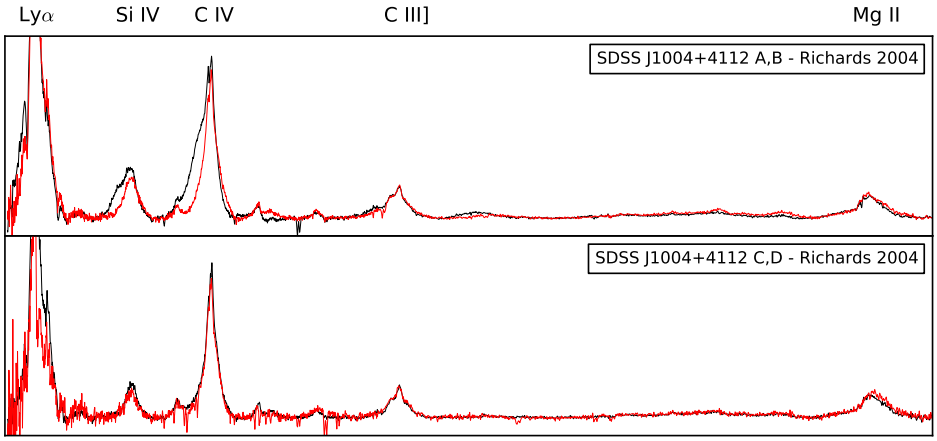

Figure 6.2: SDSS J1004-4112 is a notable case of BLR microlensing. The blue wing of Ly_{α}, CIII] and CIV are enhanced differently between components (while for the other lines this does not happen), suggesting both a common origin for these lines, and the existence of substructure in the BLR. Present data do not allow the study of this phenomenon with detail, but it remains an open possibility for future research.

6. CONSTRAINTS ON THE BROAD LINE REGION SIZE FROM LENSED QUASAR SPECTRA

6.2 Guerras et al. 2013a

6. CONSTRAINTS ON THE BROAD LINE REGION SIZE FROM LENSED QUASAR SPECTRA

The Astrophysical Journal, 764:160 (9pp), 2013 February 20 doi:10.1088/0004-637X/764/2/160

MICROLENSING OF QUASAR BROAD EMISSION LINES: CONSTRAINTS ON BROAD LINE REGION SIZE

E. Guerras[1,2], E. Mediavilla[1,2], J. Jimenez-Vicente[3,4], C. S. Kochanek[5], J. A. Muñoz[6], E. Falco[7], and V. Motta[8]
[1] Instituto de Astrofísica de Canarias, Vía Láctea S/N, La Laguna E-38200, Tenerife, Spain
[2] Departamento de Astrofísica, Universidad de la Laguna, La Laguna E-38200, Tenerife, Spain
[3] Departamento de Física Teórica y del Cosmos, Universidad de Granada, Campus de Fuentenueva, E-18071 Granada, Spain
[4] Instituto Carlos I de Física Teórica y Computacional, Universidad de Granada, E-18071 Granada, Spain
[5] Department of Astronomy and the Center for Cosmology and Astroparticle Physics, The Ohio State University, 4055 McPherson Lab, 140 West 18th Avenue, Columbus, OH 43221, USA
[6] Departamento de Astronomía y Astrofísica, Universidad de Valencia, E-46100 Burjassot, Valencia, Spain
[7] Center for Astrophysics, 60 Garden Street, Cambridge, MA 02138, USA
[8] Departamento de Física y Astronomía, Universidad de Valparaíso, Avda. Gran Bretaña 1111, Valparaíso, Chile
Received 2012 July 6; accepted 2012 December 27; published 2013 February 4

ABSTRACT

We measure the differential microlensing of the broad emission lines between 18 quasar image pairs in 16 gravitational lenses. We find that the broad emission lines are in general weakly microlensed. The results show, at a modest level of confidence (1.8σ), that high ionization lines such as C IV are more strongly microlensed than low ionization lines such as Hβ, indicating that the high ionization line emission regions are more compact. If we statistically model the distribution of microlensing magnifications, we obtain estimates for the broad line region size of $r_s = 24^{+22}_{-15}$ and $r_s = 55^{+150}_{-35}$ lt-day (90% confidence) for the high and low ionization lines, respectively. When the samples are divided into higher and lower luminosity quasars, we find that the line emission regions of more luminous quasars are larger, with a slope consistent with the expected scaling from photoionization models. Our estimates also agree well with the results from local reveberation mapping studies.

Key words: gravitational lensing: micro – quasars: emission lines

1. INTRODUCTION

Strong, broad emission lines are characteristic of many active galactic nuclei (AGNs), and their physical origins are important by virtue of their proximity to the central engine and their potential use as probes of the gas flows either fueling the AGN or feeding mass and energy back into the host galaxy. To date, the primary probe of the geometry and kinematics of the broad line regions has been reverberation mapping, where the delayed response of the emission line flux to changes in the photoionizing continuum is used to estimate the distance of the line emitting material from the central engine (see, e.g., the reviews by Peterson 1993, 2006). Reverberation mapping studies have shown that the global structure of the broad line region is consistent with photoionization models, with the radius increasing with the (roughly) square root of the continuum luminosity (e.g., Bentz et al. 2009) and high ionization lines (e.g., C IV) originating at smaller radii than low ionization lines (e.g., Hβ). Recent studies have increasingly focused on measuring the delays as a function of line velocity in order to understand the kinematics of the broad line region (Denney et al. 2009, 2010; Bentz et al. 2010; Brewer et al. 2011; Doroshenko et al. 2012; Pancoast et al. 2012). The results to date suggest that there is no common kinematic structure, with differing sources showing signs of inward, outward, and disk-like velocity structures.

While very successful, reverberation mapping suffers from several limitations. First, the studies are largely limited to relatively nearby, lower luminosity AGNs because the delay timescales for distant, luminous quasars are longer than existing monitoring programs can be sustained. Not only do the higher luminosities increase the intrinsic length of the delay (which is then further lengthened by the cosmological redshift), but the higher luminosity quasars also have lower variability amplitudes (see, e.g., MacLeod et al. 2010). Second, one of the most important applications of the results of reverberation mapping at present is as a calibrator for estimating black hole masses from single epoch spectra (Wandel et al. 1999). These calibrations are all virtually for the Hα and Hβ lines, while the easiest lines to measure for high-redshift quasars are the Mg II and C IV lines because the Balmer lines now lie in the infrared. Without direct calibrations, there is a contentious debate about the reliability of Mg II (e.g., McLure & Jarvis 2002; Kollmeier et al. 2006; Shen et al. 2008; Onken & Kollmeier 2008) and C IV (e.g., Vestergaard & Peterson 2006; Netzer et al. 2007; Fine et al. 2010; Assef et al. 2011) black hole mass estimates.

An alternative means of studying the structure of the broad line region is to examine how it is microlensed in gravitationally lensed quasars. In microlensing, the stars in the lens galaxy differentially magnify components of the quasar emission regions, leading to time- and wavelength-dependent changes in the flux ratios of the images (see the review by Wambsganss 2006). The amplitude of the magnification is controlled by the size of the emission region, with smaller source regions showing larger magnifications. The broad line region was initially considered to be too large to be affected by microlensing (Nemiroff 1988; Schneider & Wambsganss 1990), but for sizes consistent with the reverberation mapping results the broad line regions should show microlensing variability (see Mosquera & Kochanek 2011) as explored in theoretical studies by Abajas et al. (2002, 2007), Lewis & Ibata (2004), and Garsden et al. (2011). Observational evidence for microlensing in the broad line region has been discussed for Q2237+0305 (Lewis et al. 1998; Metcalf et al. 2004; Wayth et al. 2005; Eigenbrod et al. 2008; O'Dowd et al. 2011; Sluse et al. 2011), SDSS J1004+4112 (Richards et al. 2004; Gómez-Álvarez et al. 2006; Lamer et al. 2006; Abajas et al. 2007), and SDSS J0924+0219 (Keeton et al. 2006), as well as in broader surveys by Sluse et al. (2012) and Motta et al. (2012). For example, in their detailed study of Q2237+0305, Sluse et al. (2011) demonstrated the power of

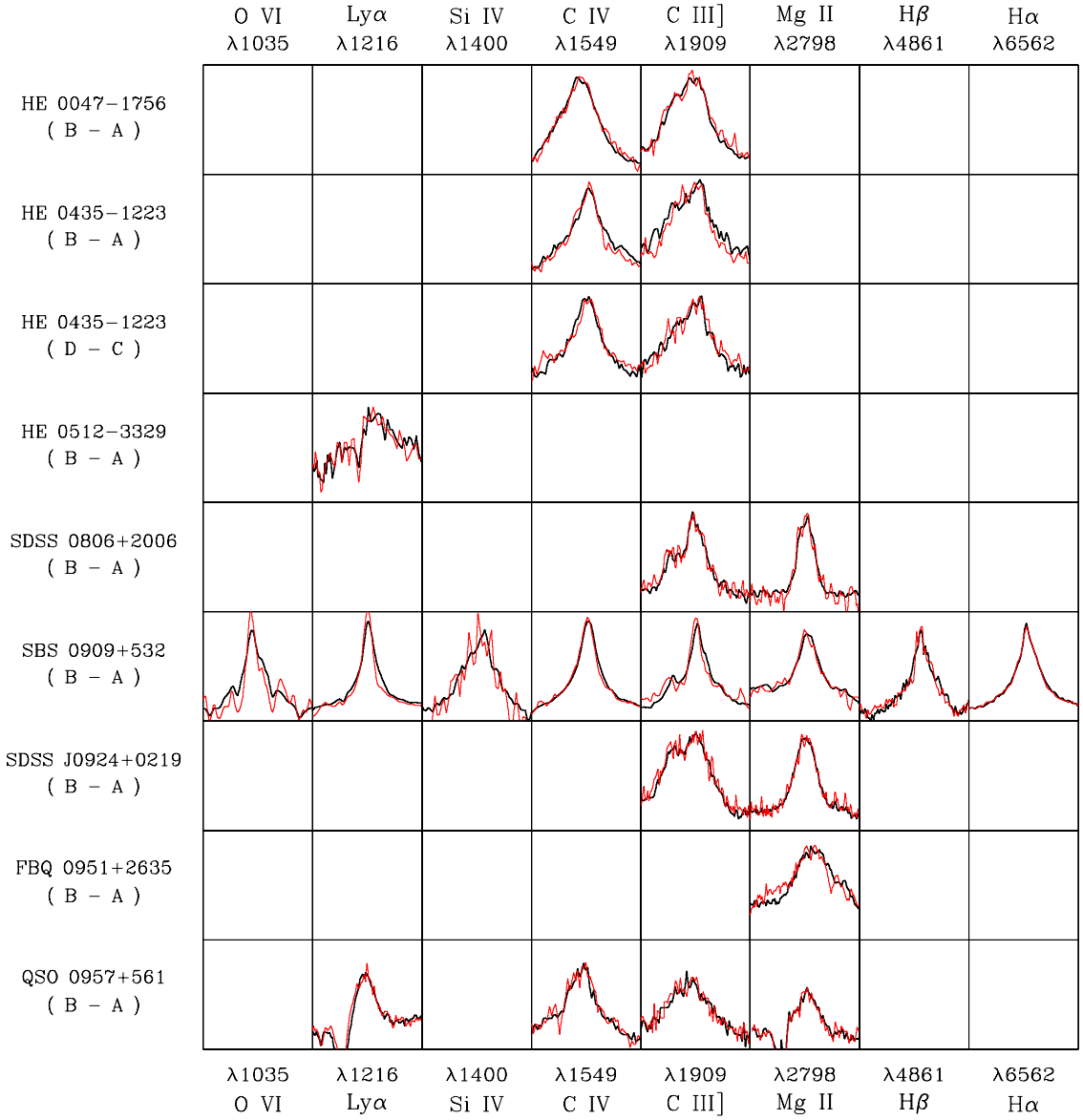

Figure 1. Panels showing superpositions of emission line profiles for image pairs of several lens systems. Continuum subtracted spectra have been scaled to match the lines. Each emission line is plotted in the (-6000 km s^{-1}, 6000 km s^{-1}) range.

microlensing, obtaining estimates of the BLR size for both C III] ($r_{\rm C\,III]} \sim 49^{+103}_{-35}$ lt-day) and C IV ($r_{\rm C\,IV} \sim 66^{+110}_{-46}$ lt-day) emission lines. Like reverberation mapping, the microlensing size estimates can also be made as a function of velocity, and the two methods can even be combined to provide even more detailed constraints (see Garsden et al. 2011).

Here we survey microlensing of the broad emission lines in a sample of 18 pairs of lensed quasar images compiled by Mediavilla et al. (2009). In Section 2, we describe the data and show that the line core and higher velocity wings are differentially microlensed. In Section 3, we use these differences to derive constraints on the size of the line emitting regions and we summarize the results in Section 4.

2. DATA ANALYSIS

In Mediavilla et al. (2009), we collected (from the literature) the UV, optical, and near-IR spectra shown in Figure 1 and summarized them in Tables 1 and 2. After excluding some of the noisier spectra used in Mediavilla et al. (2009), we are left with a sample of 18 pairs of lensed quasar images. We have divided the emission lines into two groups: low ionization lines[9] (C III] λ1909, Mg II λ2798, Hβ λ4861 and Hα λ6562) and high ionization lines[10] (O VI] λ1035, Lyα+N V λ1216, Si IV+O IV λ1400 and C IV λ1549). There is generally a very good match in the emission line profiles between images. However, there are several cases where there are obvious differences in the line profiles (see, e.g., C IV in HE0435−1223DC, Lyα+N V in SBS 0909+532, and Lyα+N V, Si IV+O IV] and C IV]

[9] In the context of our study, we have included C III] in the low ionization group because this emission line follows the behavior of the other low ionization lines in microlensing observations (e.g., Richards et al. 2004), reverberation mapping size estimates (e.g., Wandel et al. 1999), and line profile decompositions (Marziani et al. 2010).

[10] We have included Lyα+N V in the high ionization group, since it is observed to have a reverberation lag similar to C IV (Clavel et al. 1991). The Lyα flux could arise mainly from recombination in optically thin clouds where most of the high ionization metal lines arise (Allen et al. 1982).

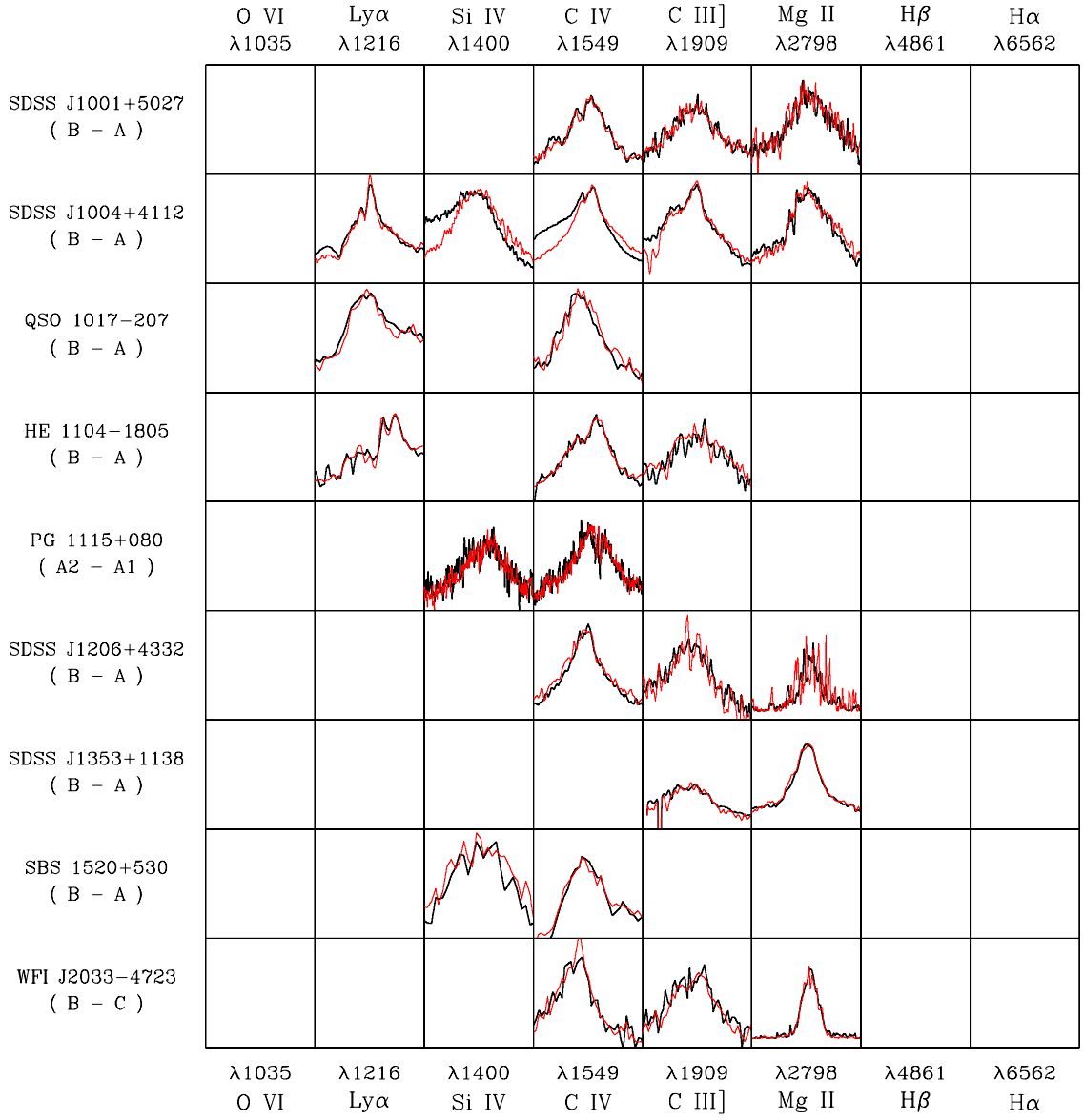

Figure 1. (Continued)

in SDSS 1004+4112BA). SDSS J1004+4112 is a well-known example (Richards et al. 2004; Gómez-Álvarez et al. 2006; Lamer et al. 2006; Abajas et al. 2007; Motta et al. 2012), where a blue bump appears in several high-ionization emission lines, as illustrated by the more detailed view of the Si IV λ1400 line in Figure 2.

In order to quantify the effects of microlensing on the broad line region, we want to isolate the effects of microlensing from those due to the large-scale macro magnification, millilensing (e.g., Dalal & Kochanek 2002), and extinction (e.g., Motta et al. 2002; Mediavilla et al. 2005). We attempt this by looking at differential flux ratios between the cores and wings of the emission lines observed in two images

$$\Delta m = (m_1 - m_2)_{\rm wings} - (m_1 - m_2)_{\rm core}. \quad (1)$$

These magnitudes are constructed from the line fluxes found after subtracting a linear model for the continuum emission underneath the line profile. Since the line emission regions are relatively compact and the wavelength differences are small, this estimator certainly removes the effects of the macro magnification, millilensing, and extinction. To see this explicitly for the macro magnification and extinction we can write the flux in magnitudes of the core (wings) of a given emission line of any of the images in a pair, $(m_{1,2})_{\rm core,wings}$, as the intrinsic flux of the source, $(m_0)_{\rm core,wings}$, magnified by the lens galaxy by an amount $\mu_{1,2}$, microlensed by an amount $(\Delta\mu_{1,2})_{\rm core,wings}$, and corrected by the extinction of this image caused by the lens galaxy, $A_{1,2}$,

$$(m_{1,2})_{\rm core,wings} = (m_0)_{\rm core,wings} + \mu_{1,2} + A_{1,2} + (\Delta\mu_{1,2})_{\rm core,wings}. \quad (2)$$

Thus, the difference between the wings and core fluxes cancels out the terms corresponding to intrinsic magnification and extinction, $(\mu{+}A)_{1,2}$, and the difference between images cancels out the intrinsic flux ratio, $(m_0)_{\rm wings} - (m_0)_{\rm core}$, leaving only the differential microlensing term,

$$\begin{aligned}\Delta m &= (m_1 - m_2)_{\rm wings} - (m_1 - m_2)_{\rm core} \\ &= (\Delta\mu_1 - \Delta\mu_2)_{\rm wings} - (\Delta\mu_1 - \Delta\mu_2)_{\rm core}. \end{aligned} \quad (3)$$

Table 1
Lensed Quasars Sample

Object (Pair)	z	Observation Date	Rest Wavelength Range[a]	Luminosity[b]	Reference
HE 0047-1756 A, B	1.67	2002 Sep 4	(1461–2547)	2.58×10^4	Wisotzki et al. 2004
HE 0435-1223 A, B	1.689	2002 Sep 2–7	(1413–2529)	9.69×10^3	Wisotzki et al. 2003
HE 0435-1223 C, D	1.689	2002 Sep 2–7	(1413–2529)	9.69×10^3	Wisotzki et al. 2003
HE 0512-3329 A, B	1.58	2001 Aug 13	(0775–2171)	5.10×10^4	Wucknitz et al. 2003
SDSS 0806+2006 A, B	1.54	2005 Apr 12	(1575–3504)	1.09×10^4	Inada et al. 2006
SBS 0909+532 A, B[c]	1.38	2005 Jan 22	(0957–2378)	2.79×10^5	Mediavilla et al. 2011a
		2004 Mar 5			
		2003 Mar 7			
		2001 Jan 18			
SDSS J0924+0219 A, B[d]	1.524	2005 Jan 14	(1783–3170)	5.65×10^3	Eigenbrod et al. 2006
		2005 Feb 1			
FBQ 0951+2635 A, B	1.24	1997 Feb 14	(1786–4018)	2.02×10^5	Schechter et al. 1998
QSO 0957+561 A	1.41	1999 Apr 15	(0913–4149)	9.16×10^3	Goicoechea et al. 2005
QSO 0957+561 B	1.41	2000 Jun 2–3	(0913–4149)	9.16×10^3	Goicoechea et al. 2005
SDSS J1001+5027 A, B	1.838	2003 Nov 20	(1409–3136)	4.13×10^4	Oguri et al. 2005
SDSS J1004+4112 A, B	1.732	2004 Jan 19	(1318–2928)	8.17×10^3	Gómez-Álvarez et al. 2006
QSO 1017-207 A, B	2.545	1996 Oct 28	(1016–1975)	1.27×10^5	Surdej et al. 1997
HE 1104-1805 A, B	2.32	1993 May 11	(1211–2846)	1.60×10^5	Wisotzki et al. 1995
PG 1115+080 A1	1.72	1996 Jan 21	(0846–1213)	2.41×10^4	Popović & Chartas 2005
PG 1115+080 A2	1.72	1996 Jan 24	(0846–1213)	2.41×10^4	Popović & Chartas 2005
SDSS J1206+4332 A, B	1.789	2004 Jun 21	(1362–3048)	8.55×10^3	Oguri et al. 2005
SDSS J1353+1138 A, B	1.629	2005 Apr 12	(1521–3385)	1.27×10^5	Inada et al. 2006
SBS 1520+530 A, B	1.855	1996 Jun 12	(1331–2452)	4.86×10^4	Chavushyan et al. 1997
WFI J2033-4723 B, C	1.66	2003 Sep 15	(1429–3008)	8.30×10^3	Morgan et al. 2004

Notes.
[a] Wavelength in Å.
[b] Luminosity corresponds to $\lambda L_\lambda(5100\,\text{Å})$ in units of 10^{40} erg.
[c] Optical, UV, and near-IR spectra were obtained at different epochs.
[d] The spectra from the two epochs were averaged.

Table 2
Differential Microlensing, $\Delta m_{\rm core} - \Delta m_{\rm wings}$, of the High (HIL) and Low (LIL) Ionization Emission Lines

Object (Pair)	λ1035	λ1216	λ1400	λ1549	⟨HIL⟩	λ1909	λ2798	λ4861	λ6562	⟨LIL⟩
HE 0047–1756 (B-A)	...	...	...	+0.03	+0.03	+0.03	...	...	...	+0.03
HE 0435–1223 (B-A)	...	...	...	−0.21	−0.21	−0.19	...	...	...	−0.19
HE 0435–1223 (D-C)	...	...	...	+0.19	+0.19	+0.07	...	...	...	+0.07
HE 0512–3329 (B-A)	...	+0.04	...	...	+0.04	...	...	...	...	...
SDSS 0806+2006 (B-A)	...	...	...	...	...	+0.09	−0.26	...	...	−0.09
SBS 0909+532 (B-A)	−0.43	−0.23	...	−0.04	−0.18	−0.01	−0.02	−0.14	+0.00	−0.04
SDSS J0924+0219 (B-A)	...	...	...	...	...	+0.09	+0.09	...	...	+0.09
FBQ 0951+2635 (B-A)	...	...	...	...	...	...	+0.04	...	...	+0.04
QSO 0957+561 (B-A)	...	+0.03	...	+0.03	+0.03	+0.08	−0.13	...	...	−0.03
SDSS J1001+5027 (B-A)	...	...	...	−0.04	−0.04	+0.01	+0.04	...	...	+0.02
SDSS J1004+4112 (B-A)	...	−0.07	−0.29	−0.23	−0.20	−0.06	+0.02	...	...	−0.02
QSO 1017–207 (B-A)	...	−0.08	...	+0.15	+0.03	...	...	...	...	...
HE 1104–1805 (B-A)	...	+0.03	...	+0.02	+0.02	+0.03	...	...	...	+0.03
PG 1115+080 (A2-A1)	...	...	−0.10	−0.04	−0.07	...	...	...	...	...
SDSS J1206+4332 (A-B)	...	...	...	+0.17	+0.17	−0.12	+0.15	...	...	+0.01
SDSS J1353+1138 (A-B)	...	...	...	...	...	−0.16	+0.05	...	...	−0.06
SBS 1520+530 (B-A)	...	...	+0.19	+0.16	+0.18	...	...	...	...	...
WFI J2033–4723 (B-C)	...	...	...	−0.05	−0.05	−0.18	−0.14	...	...	−0.16

We are going to assume that the line core, centered at the peak of the line and defined by the velocity range $|\Delta v| < 850\,\text{km s}^{-1}$, is little affected by microlensing compared to the wings, $\Delta m \sim (\Delta\mu_1 - \Delta\mu_2)_{\rm wings}$. Existing velocity-resolved reverberation maps (Denney et al. 2009, 2010; Bentz et al. 2010; Barth et al. 2011; Pancoast et al. 2012) all find longer reverberation time delays in this velocity range, indicating that the material in the line core generally lies at larger distances from the central engine. Sluse et al. (2011) also found this in their microlensing analysis of Q2237+0305. Essentially, high-velocity material must be close to the central engine to have the observed Doppler shifts, while the low-velocity material is a mixture of material close to the black hole but moving perpendicular to the line of sight and material far from the black hole with intrinsically low velocities. As a result, the line core should generically be produced by material spread over a broader area and hence be significantly less microlensed than the line wings.

The microlensing effects will be little contaminated by intrinsic variability modulated by the lens time delays. The expected continuum variability on such timescales is only of

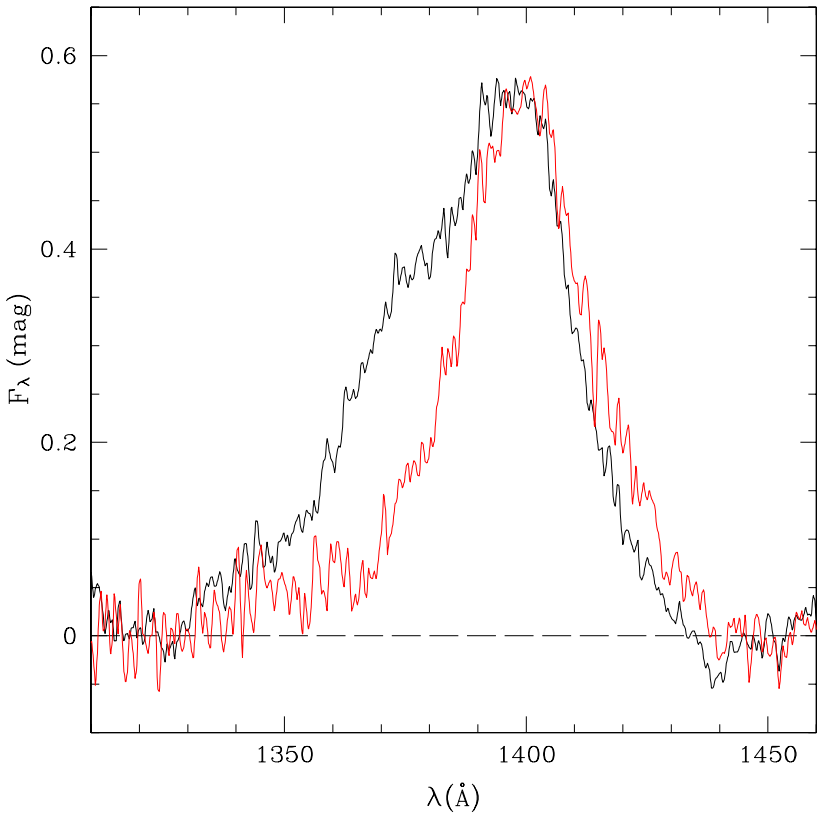

Figure 2. Detailed view of the differences in the Si IV λ1400 line profiles corresponding to the A and B images of SDSS J1004+4112 from Richards et al. (2004).

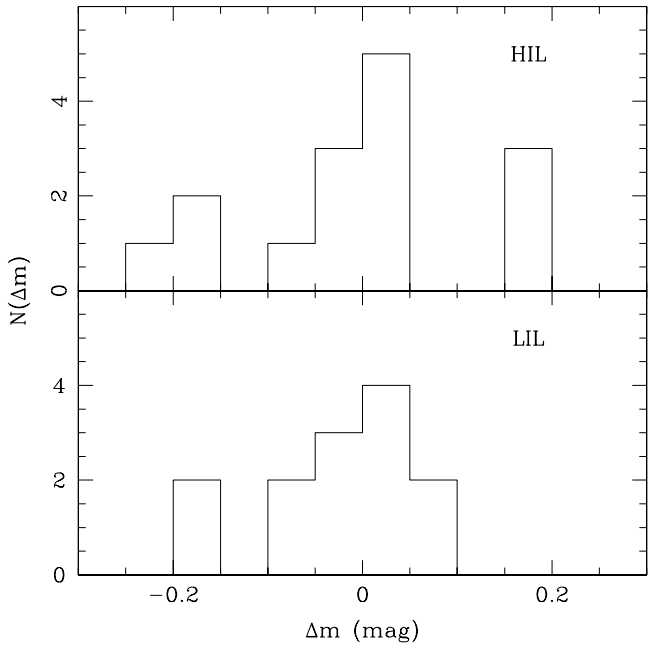

Figure 3. Histograms of the microlensing magnifications, Δm, observed for the high (upper) and low (lower) ionization lines.

order 0.1 mag (MacLeod et al. 2010, generally, or Yonehara et al. 2008, in the context of lenses). The global line variability is then only 20%–30% of the continuum variability because it is a smoothed response to the continuum, so differential (wings/core) line variability effects should be small. Thus, we expect these effects to represent only a modest contribution to the apparent noise.

Figure 3 shows histograms of Δm for the low and high ionization lines, and the values are reported in Table 2. The first point to note is that even the largest microlensing effects are relatively small, with $|\Delta m| < 0.2$ mag. The second point to note is that more HIL (6 of 15) than LIL (2 of 13) show significantly non-zero magnifications, $|\Delta m| \gtrsim 0.15$, given the typical (0.05 mag) uncertainties (here we are counting only image pairs showing the anomalies, not the numbers of lines showing anomalies, so a system like SDSSJ 1004+4112 with multiple high-ionization anomalies is counted only once). A binomial distribution predicts a low probability (6%) of reproducing the HIL fraction of $|\Delta m| \gtrsim 0.15$ given the LIL fraction. Qualitatively, both high and low ionization lines are weakly microlensed but the LIL in our sample seem to be less affected by microlensing than the HIL at a $\sim 2\sigma$ level of confidence. Although the confirmation of this last result would benefit from a larger and more homogeneous sample with simultaneous observations of the HIL and LIL, there is no obvious bias in the data that would yield this result. Moreover, five of the six image pairs that show significant microlensing of the HIL ($|\Delta m| \gtrsim 0.15$) were also observed in the LIL. The exclusion of the remaining case does not significantly affect the results of Section 3.

3. CONSTRAINING THE SIZE OF THE BROAD LINE REGION

Given these estimates of the differential effects of microlensing on the core and wings of the emission lines, we can use standard microlensing Monte Carlo methods to estimate the size of the emission regions. For simplicity in a first calculation we assume that the line core emission regions are large enough that they are effectively not microlensed and simply model the

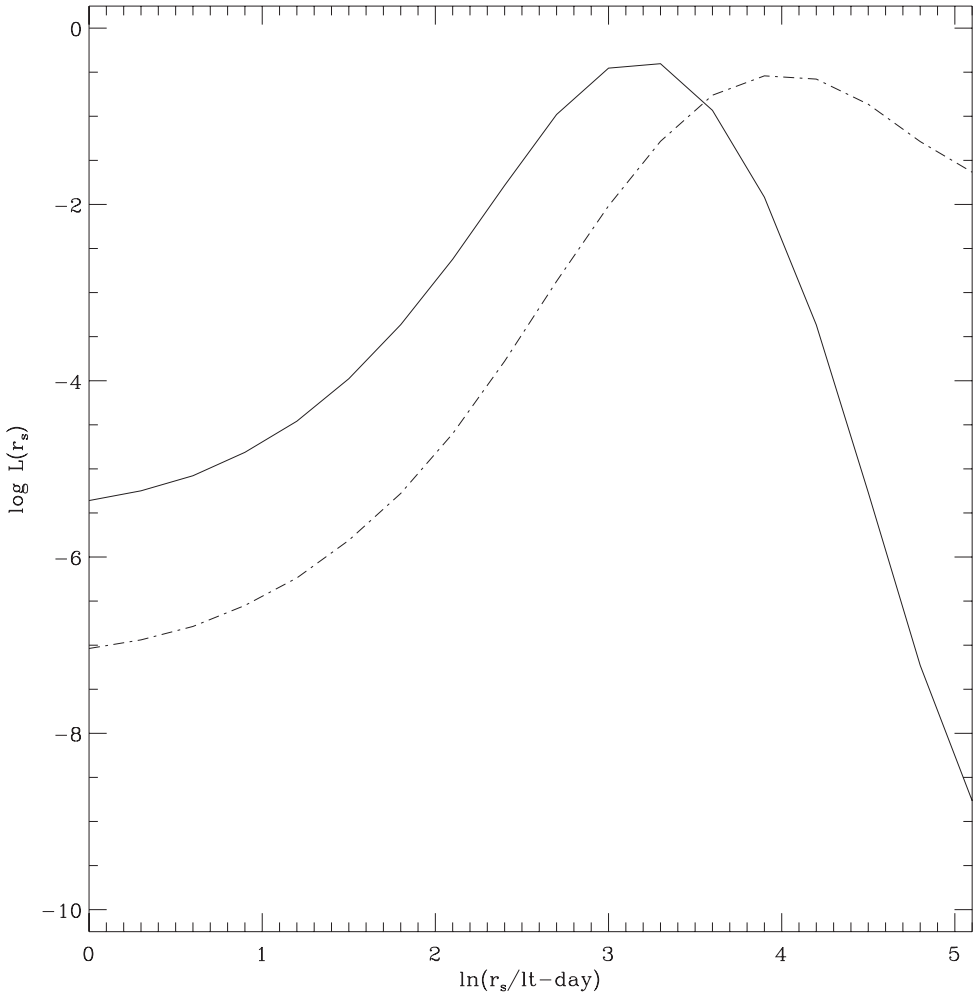

Figure 4. Maximum likelihood curves for the size of the regions of high (solid) and low (dashed) ionization lines, respectively.

luminosity profile of the region emitting the wings as a Gaussian. Mortonson et al. (2005) have shown that the effects of microlensing are largely controlled by the projected half-light area of the source, and even with full microlensing light curves it is difficult to estimate the shape of the emission regions (see Poindexter & Kochanek 2010; Blackburne et al. 2011).

We use the estimates of the dimensionless surface density κ and shear γ of the lens for each image from Mediavilla et al. (2009) or the updated values for SBS 0909+532 from Mediavilla et al. (2011b). We assume that the fraction of the mass in stars is 5% (see, e.g., Mediavilla et al. 2009; Pooley et al. 2009, 2012). For a stellar mass of $M = 1\,M_{\odot}$, we generated square magnification patterns for each image which were 1000 lt-day across and had a 0.5 lt-day pixel scale using the inverse polygon mapping algorithm (Mediavilla et al. 2006, 2011a). The magnifications experienced by a Gaussian source of size r_s ($I \propto \exp(-R^2/2r_s^2)$) are then found by convolving the magnification pattern with the Gaussian. We used a logarithmic grid of source sizes, $\ln r_s = 0.3 \times i$ for $i = 0, \ldots, 17$, where r_s is in units of light-days. The source sizes can be scaled to a different mean stellar mass, M, as[11] $r_s \propto (M/M_{\odot})^{1/2}$. We will follow a procedure similar to that used to estimate the average size of quasar accretion disks by Jiménez-Vicente et al. (2012).

For any pair of images, we can generate the expected magnitude differences for a given source size by randomly drawing magnifications m_1 and m_2 from the convolved magnification pattern for the two images and taking the difference $\Delta m = m_1 - m_2$. The probability of observing a magnitude difference $\Delta m_{\mathrm{obs},k} \pm \sigma_k$ for image pair k (averaged over the LIL or HIL; see Table 2) given a source size r_s is then

$$p_k(r_s) \propto \sum_{l=1}^{N} \exp\left(-\frac{1}{2}\left(\frac{\Delta m_l - \Delta m_{\mathrm{obs},k}}{\sigma_k}\right)^2\right) \qquad (4)$$

for $N = 10^8$ random trials at each source size. We can then estimate an average size for either the high or low ionization lines by combining the likelihoods

$$L(r_s) = \prod p_k(r_s) \qquad (5)$$

for the individual image pairs. Implicitly we are also drawing magnifications for the core but assuming they are close enough to unity to be ignored.

Figure 4 shows the resulting likelihood functions for the high and low ionization lines. Simply using maximum likelihood estimation, we find 90% confidence estimates for the average

[11] Lensing by stars of mass $M_{\odot}$ can be described in an invariant form using a characteristic length scale (Einstein radius) $\xi_0 \propto M_{\odot}^{1/2}$. A transformation of the mass of the stars, $M_{\odot} \rightarrow M$, will result in a scale change $\xi_0 \rightarrow \xi_0(M/M_{\odot})^{1/2}$ that leaves invariant the dimensionless surface density, $\kappa \propto M/\xi_0^2$.

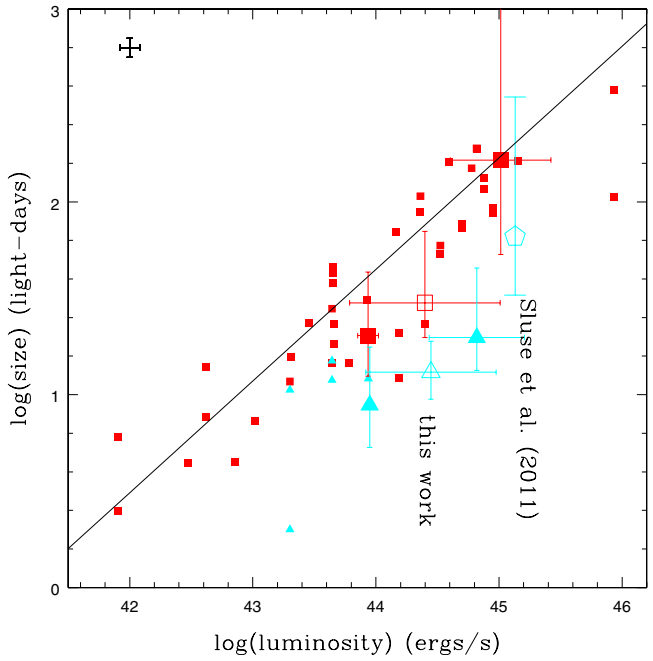

Figure 5. Estimates of high (red) and low (blue) ionization broad line region sizes (scaled to $\langle M\rangle = 0.3\,M_\odot$ for the mean mass and using $\pm 1\sigma$ error bars) as a function of quasar luminosity. The present results (large triangles and squares) and the result by Sluse et al. (2011) for Q2237+0305 (large open pentagon) are shown using the magnification-corrected luminosity estimates of Mosquera & Kochanek (2011). The three large blue triangles (red squares) from the present work correspond to the low, total (open symbol), and high luminosity subsamples defined in our data for the high (low) ionization lines (see the text). The results from local reverberation mapping studies are shown by the small triangles (high ionization lines) and squares (low ionization lines), using the uniform estimates of the lags by Zu et al. (2011) and the host-corrected luminosities from Bentz et al. (2009). The line is the best-fit correlation found by Zu et al. (2011). The cross in the upper left corner shows the average uncertainty of the reverberation mapping lag and the variance in the source luminosity during the mapping campaign.

sizes of the high and low ionization lines of $r_s = 24^{+22}_{-15}\sqrt{M/M_\odot}$ and $r_s = 55^{+150}_{-35}\sqrt{M/M_\odot}$ lt-day, respectively (the upper limit for the LIL was obtained using a linear extrapolation of the likelihood function). At 68% confidence we find $r_s = 24^{+9}_{-8}\sqrt{M/M_\odot}$ lt-day (HIL) and $r_s = 55^{+47}_{-23}\sqrt{M/M_\odot}$ lt-day (LIL). Here, we include the scaling of the inferred size with the mass of the microlenses, $\sqrt{M/M_\odot}$. From the likelihood functions (Figure 4), the hypothesis that the LIL and HIL have the same size is excluded at 1.8σ.

We can make a rough estimate of the consequences of ignoring microlensing of the line core by raising (lowering) the magnifications to represent anti-correlated (correlated) changes in the core relative to the line. The effects of uncorrelated changes will be intermediate to these limits (more complex models explicitly including the kinematics of the emitters are explored in Appendix). For changes of 20% in microlensing amplitude (from $0.8\Delta m$ to $1.2\Delta m$), the central sizes shift from $r_s = 20$ to 37 lt-day for the high ionization lines and from $r_s = 37$ to 120 lt-day for the low ionization lines.

We also calculated the sizes for low ($L < 2\times10^{44}$ erg s^{-1}) and high ($L > 2\times10^{44}$ erg s^{-1}) luminosity sub-samples based on the magnification-corrected luminosity estimates at 5100 Å (rest frame) from Mosquera & Kochanek (2011). For the low-luminosity sub-sample we find (68% confidence) $r_s = 16^{+11}_{-8}\sqrt{M/M_\odot}$ and $37^{+28}_{-18}\sqrt{M/M_\odot}$ lt-day for the high and low ionization lines, while for the high-luminosity sub-sample we find (68% confidence) $r_s = 36^{+30}_{-14}\sqrt{M/M_\odot}$ and $r_s = 299^{+\text{indet.}}_{-103}\sqrt{M/M_\odot}$ lt-day. Here we extended the grid in r_s up to 400 lt-day for the high-luminosity, LIL case. While the uncertainties are too large to accurately estimate the scaling of the size with luminosity, the changes are consistent with the $L^{1/2}$ scaling expected from simple photoionization models.

Figure 5 compares these estimates to the results from the reverberation mapping of local AGNs using the uniform lag estimates by Zu et al. (2011) and the host galaxy-corrected luminosities of Bentz et al. (2009). In this figure we have scaled our estimates of r_s for microlenses of $\langle M\rangle = 0.3\,M_\odot$.[12] While the uncertainties in our microlensing estimates are relatively large, the agreement with the reveberation mapping results is striking. This is clearest for the low ionization lines which are the ones most easily measured in ground-based reverberation mapping campaigns, but the offset we find between the high and low ionization lines agrees with the offsets seen for the limited number of reverberation mapping results for high ionization lines. We also show the estimated size of the C IV emission region for Q2237+030 by Sluse et al. (2011) which shows a similar level of agreement. Because we are measuring the size of the higher velocity line components rather than the full line, our results should be somewhat smaller than the reverberation mapping estimates for the full line.

4. CONCLUSIONS

Consistent with other recent studies (e.g., Sluse et al. 2011, 2012; Motta et al. 2012) we have found that the broad emission lines of gravitationally lensed quasars are, in general, weakly microlensed. At a 1.8σ level of confidence high and low ionization lines appear to be microlensed differently, with higher magnifications observed for the higher ionization lines. This indicates that the emission regions associated with the high ionization lines are probably more compact, as would be expected from photoionization models. If we then make simple models of the microlensing effects, we obtain size estimates (90% confidence) of $r_s = 24^{+22}_{-15}\sqrt{M/M_\odot}$ and $r_s = 55^{+150}_{-35}\sqrt{M/M_\odot}$ lt-day for the high and low ionization lines. We have also calculated the sizes for low- and high-luminosity sub-samples, finding that the dependence of size with luminosity is consistent with the $L^{1/2}$ scaling expected from simple photoionization models. Our estimates also agree well with the measurements from local reveberation mapping studies. These results strongly suggest that the lensed quasars can provide an independent check of reverberation mapping results and extend them to far more distant quasars relatively economically. Microlensing should also be able to address the controversies about lines like C IV which have few direct reverberation mapping measurements but are crucial tools for studying the evolution of black holes at higher redshifts.

With nearly 100 lensed quasars (see Mosquera & Kochanek 2011) it is relatively easy to expand the sample and to begin making estimates of the size as a function of luminosity or other variables. Accurate estimates for individual quasars will probably require spectrophotometric monitoring, as done by Sluse et al. (2011). Since the broad line emission regions are relatively large, the timescale for the variability is relatively long. A significant constraint can be gained for most of these lenses simply by obtaining one additional spectrum to search

[12] This mean value is expected in typical stellar mass functions (see, e.g., Pooley et al. 2009).

for changes over the years that have elapsed since many of the archival spectra we have used here were taken. The lenses may also be some of the better targets for reverberation studies at higher redshifts because the time delays of the images provide early warning of continuum flux changes and better temporal sampling of both the line and continuum for the same investment of observing resources.

The authors thank the anonymous referee for valuable comments and suggestions. The authors are grateful to B. M. Peterson and A. Mosquera for their comments and for kindly providing data. This research was supported by the Spanish Ministerio de Educación y Ciencia with the grants C-CONSOLIDER AYA2007-67625-C02-02, AYA2007-67342-C03-01/03, and AYA2010-21741-C03-01/02. J.J.V. is also supported by the Junta de Andalucía through the FQM-108 project. J.A.M. is also supported by the Generalitat Valenciana with the grant PROMETEO/2009/64. C.S.K. is supported by NSF grant AST-1009756. V.M. gratefully acknowledges support from FONDECYT through grant 1120741.

APPENDIX

EXPLORING KINEMATIC MODELS

The problem for analyzing more complex models including the kinematics of the emitters is that there is no simple, generally accepted structural model for the broad line region, and the initial results of the velocity-resolved reverberation mapping experiments (Denney et al. 2009, 2010; Bentz et al. 2010; Brewer et al. 2011; Doroshenko et al. 2012; Pancoast et al. 2012) suggest that there may be no such common structure. As an experiment, we constructed a model consisting of an inner rotating disk and an outer spherical shell which dominates the core emission. We set the inner edge of the disk to $r_{\rm disk,in} = 5$ lt-day and left the outer edge $r_{\rm disk,out}$ as the adjustable parameter. For simplicity we used a constant emissivity for the disk and a Keplerian rotation profile with an inner edge velocity of 10^4 km s^{-1}. The disk has an inclination of 45°. For the spherical shell we adopted fixed inner and outer radii of $r_{\rm sphere,in} = 60$ and $r_{\rm sphere,out} = 160$ lt-day, respectively. For the shell we used a $v \propto 1/r^2$ velocity profile with a velocity of 5000 km s^{-1} at the inner edge. We normalized the models so that the disk contributes 20% of the flux at zero velocity, which also results in a single-peaked line profile that resembles typical broad line profiles. We only carried out the calculations for a representative set of lens parameters ($\kappa_1 = \gamma_1 = 0.45$ and $\kappa_2 = \gamma_2 = 0.55$; see Mediavilla et al. 2009), but we now calculate Δm to correctly include the differential microlensing of the core and the wing. The final results for the outer radius of the disk component which dominates the wings of the line profile are (68% confidence): $r_{\rm disk,out} = 50^{+40}_{-20}$ and $r_{\rm disk,out} = 70 \pm 30$ lt-day for the high and low ionization lines, respectively. The corresponding radii enclosing half of the total disk luminosity are $r_{1/2} = r_{\rm disk,out}/\sqrt{2} = 30^{+28}_{-14}$ lt-day (HIL) and 49 ± 21 lt-day (LIL). These values are in reasonable agreement with the results obtained in Section 3 without taking into account kinematics, $r_{1/2} = 1.18 r_s = 28^{+11}_{-9}$ lt-day (HIL) and 65^{+55}_{-27} lt-day (LIL). While the model is somewhat arbitrary, the similarity of the results to the simpler analysis of Section 3 shows that it is possible to find kinematical models (probably many) that can explain the measured microlensing consistently with the hypothesis that the line core mainly arises from a region insensitive to microlensing.

REFERENCES

Abajas, C., Mediavilla, E., Muñoz, J. A., Gómez-Álvarez, P., & Gil-Merino, R. 2007, ApJ, 658, 748
Abajas, C., Mediavilla, E., Muñoz, J. A., Popović, L. Č., & Oscoz, A. 2002, ApJ, 576, 640
Allen, D. A., Barton, J. R., Gillingham, P. R., & Carswell, R. F. 1982, MNRAS, 200, 271
Assef, R. J., Denney, K. D., Kochanek, C. S., et al. 2011, ApJ, 742, 93
Barth, A. J., Nguyen, M. L., Malkan, M. A., et al. 2011, ApJ, 732, 121
Bentz, M. C., Horne, K., Barth, A. J., et al. 2010, ApJL, 720, L46
Bentz, M. C., Peterson, B. M., Netzer, H., Pogge, R. W., & Vestergaard, M. 2009, ApJ, 697, 160
Blackburne, J. A., Kochanek, C. S., Chen, B., Dai, X., & Chartas, G. 2011, arXiv:1112.0027
Brewer, B. J., Treu, T., Pancoast, A., et al. 2011, ApJL, 733, L33
Chavushyan, V. H., Vlasyuk, V. V., Stepanian, J. A., & Erastova, L. K. 1997, A&A, 318, L67
Clavel, J., Reichert, G. A., Alloin, D., et al. 1991, ApJ, 366, 64
Dalal, N., & Kochanek, C. S. 2002, ApJ, 572, 25
Denney, K. D., Peterson, B. M., Pogge, R. W., et al. 2009, ApJL, 704, L80
Denney, K. D., Peterson, B. M., Pogge, R. W., et al. 2010, ApJ, 721, 715
Doroshenko, V. T., Sergeev, S. G., Klimanov, S. A., Pronik, V. I., & Efimov, Y. S. 2012, MNRAS, 426, 416
Eigenbrod, A., Courbin, F., Dye, S., et al. 2006, A&A, 451, 747
Eigenbrod, A., Courbin, F., Sluse, D., Meylan, G., & Agol, E. 2008, A&A, 480, 647
Fine, S., Croom, S. M., Bland-Hawthorn, J., et al. 2010, MNRAS, 409, 591
Garsden, H., Bate, N. F., & Lewis, G. F. 2011, MNRAS, 418, 1012
Goicoechea, L. J., Gil-Merino, R., & Ullán, A. 2005, MNRAS, 360, L60
Gómez-Álvarez, P., Mediavilla, E., Muñoz, J. A., et al. 2006, ApJL, 645, L5
Inada, N., Oguri, M., Becker, R. H., et al. 2006, AJ, 131, 1934
Jiménez-Vicente, J., Mediavilla, E., Muñoz, J. A., & Kochanek, C. S. 2012, ApJ, 751, 106
Keeton, C. R., Burles, S., Schechter, P. L., & Wambsganss, J. 2006, ApJ, 639, 1
Kollmeier, J. A., Onken, C. A., Kochanek, C. S., et al. 2006, ApJ, 648, 128
Lamer, G., Schwope, A., Wisotzki, L., & Christensen, L. 2006, A&A, 454, 493
Lewis, G. F., & Ibata, R. A. 2004, MNRAS, 348, 24
Lewis, G. F., Irwin, M. J., Hewett, P. C., & Foltz, C. B. 1998, MNRAS, 295, 573
MacLeod, C. L., Ivezić, Ž., Kochanek, C. S., et al. 2010, ApJ, 721, 1014
Marziani, P., Sulentic, J. W., Negrete, C. A., et al. 2010, MNRAS, 409, 1033
McLure, R. J., & Jarvis, M. J. 2002, MNRAS, 337, 109
Mediavilla, E., Mediavilla, T., Muñoz, J. A., et al. 2011a, ApJ, 741, 42
Mediavilla, E., Muñoz, J. A., Falco, E., et al. 2009, ApJ, 706, 1451
Mediavilla, E., Muñoz, J. A., Kochanek, C. S., et al. 2005, ApJ, 619, 749
Mediavilla, E., Muñoz, J. A., Kochanek, C. S., et al. 2011b, ApJ, 730, 16
Mediavilla, E., Muñoz, J. A., Lopez, P., et al. 2006, ApJ, 653, 942
Metcalf, R. B., Moustakas, L. A., Bunker, A. J., & Parry, I. R. 2004, ApJ, 607, 43
Morgan, N. D., Caldwell, J. A. R., Schechter, P. L., et al. 2004, AJ, 127, 2617
Mortonson, M. J., Schechter, P. L., & Wambsganss, J. 2005, ApJ, 628, 594
Mosquera, A. M., & Kochanek, C. S. 2011, ApJ, 738, 96
Motta, V., Mediavilla, E., Falco, E., & Munoz, J. A. 2012, ApJ, 755, 82
Motta, V., Mediavilla, E., Muñoz, J. A., et al. 2002, ApJ, 574, 719
Nemiroff, R. J. 1988, ApJ, 335, 593
Netzer, H., Lira, P., Trakhtenbrot, B., Shemmer, O., & Cury, I. 2007, ApJ, 671, 1256
O'Dowd, M., Bate, N. F., Webster, R. L., Wayth, R., & Labrie, K. 2011, MNRAS, 415, 1985
Oguri, M., Inada, N., Hennawi, J. F., et al. 2005, ApJ, 622, 106
Onken, C. A., & Kollmeier, J. A. 2008, ApJL, 689, L13
Pancoast, A., Brewer, B. J., Treu, T., et al. 2012, ApJ, 754, 49
Peterson, B. M. 1993, PASP, 105, 247
Peterson, B. M. 2006, in ASP Conf. Ser. 360, AGN Variability from X-rays to Radio Waves, ed. C. M. Gaskell, I. M. McHardy, B. M. Peterson, & S. G. Sergeev (San Francisco, CA: ASP), 191
Poindexter, S., & Kochanek, C. S. 2010, ApJ, 712, 668
Pooley, D., Rappaport, S., Blackburne, J. A., Schechter, P. L., & Wambsganss, J. 2012, ApJ, 744, 111
Pooley, D., Rappaport, S., Blackburne, J., et al. 2009, ApJ, 697, 1892
Popović, L. Č., & Chartas, G. 2005, MNRAS, 357, 135
Richards, G. T., Keeton, C. R., Pindor, B., et al. 2004, ApJ, 610, 679
Schechter, P. L., Gregg, M. D., Becker, R. H., Helfand, D. J., & White, R. L. 1998, AJ, 115, 1371
Schneider, P., & Wambsganss, J. 1990, A&A, 237, 42

Shen, Y., Greene, J. E., Strauss, M. A., Richards, G. T., & Schneider, D. P. 2008, ApJ, 680, 169
Sluse, D., Hutsemékers, D., Courbin, F., Meylan, G., & Wambsganss, J. 2012, A&A, 544, A62
Sluse, D., Schmidt, R., Courbin, F., et al. 2011, A&A, 528, A100
Surdej, J., Claeskens, J.-F., Remy, M., et al. 1997, A&A, 327, L1
Vestergaard, M., & Peterson, B. M. 2006, ApJ, 641, 689
Wambsganss, J. 2006, in Saas-Fee Advanced Course 33: Gravitational Lensing: Strong, Weak and Micro, ed. G. Meylan, P. Jetzer, & P. North (Berlin: Springer), 453
Wandel, A., Peterson, B. M., & Malkan, M. A. 1999, ApJ, 526, 579
Wayth, R. B., O'Dowd, M., & Webster, R. L. 2005, MNRAS, 359, 561
Wisotzki, L., Becker, T., Christensen, L., et al. 2003, A&A, 408, 455
Wisotzki, L., Koehler, T., Ikonomou, M., & Reimers, D. 1995, A&A, 297, L59
Wisotzki, L., Schechter, P. L., Chen, H.-W., et al. 2004, A&A, 419, L31
Wucknitz, O., Wisotzki, L., Lopez, S., & Gregg, M. D. 2003, A&A, 405, 445
Yonehara, A., Hirashita, H., & Richter, P. 2008, A&A, 478, 95
Zu, Y., Kochanek, C. S., & Peterson, B. M. 2011, ApJ, 735, 80

6. CONSTRAINTS ON THE BROAD LINE REGION SIZE FROM LENSED QUASAR SPECTRA

7

Microlensing of Quasar UV Iron Emission

7.1 Introduction

Iron has the largest binding energy per nucleon, making it both quite a stable nucleus in extreme conditions and an abundant end product of nucleosynthesis processes. But, while lighter elements produce a relatively small number of well known emission lines, iron emission consists on a large and complex set of electronic levels giving rise to many superposed lines, resulting in several blended bands across quasar spectra.

Both the mechanism generating this emission and the spatial scale of the region where it is emitted are poorly understood. Recent attempts based on reverberation mapping (Barth et al. 2013) suggest that the emission comes from the BLR. However, an older study on the Seyfert galaxy NGC 5548 (Maoz & Netzer 1993) placed the origin in an inner region. Until now, no systematic microlensing study had been used to clarify this question.

Here we will use the dependency of the microlensing amplification with the size of the emitting region, attempting to give a clue on the origin of the UV Fe II and Fe III blended bands, both in the UV region. Superposing a sample of spectra, we find that some of the objects, once subtracted the continuum emission, show remarkable differences in the intensity of the iron blends, while the rest of the spectra nicely match on top of each other. This suggests that the emission can be strongly amplified by microlensing, thus it may arise from a very small region.

7. MICROLENSING OF QUASAR UV IRON EMISSION

Using the narrow Mg II λ2798 emission line as baseline, we apply a Bayesian Montecarlo analysis based upon a set of magnification maps tailored for each object. We repeat the study, using CIII] λ1909 as baseline. In both cases, our results suggest that the iron lines may arise from the nucleus of the quasar engine, in a region of less than 10 light-days in size, more in accordance with the 1993 findings of Maoz in NGC 5548.

7.2 Guerras et al. 2013b

The Astrophysical Journal, 778:123 (6pp), 2013 December 1 doi:10.1088/0004-637X/778/2/123

MICROLENSING OF QUASAR ULTRAVIOLET IRON EMISSION

E. Guerras[1,2], E. Mediavilla[1,2], J. Jimenez-Vicente[3,4], C. S. Kochanek[5], J. A. Muñoz[6], E. Falco[7], V. Motta[8], and K. Rojas[8]
[1] Instituto de Astrofísica de Canarias, Vía Láctea S/N, La Laguna 38200, Tenerife, Spain
[2] Departamento de Astrofísica, Universidad de la Laguna, La Laguna 38200, Tenerife, Spain
[3] Departamento de Física Teórica y del Cosmos, Universidad de Granada, Campus de Fuentenueva, 18071 Granada, Spain
[4] Instituto Carlos I de Física Teórica y Computacional, Universidad de Granada, 18071 Granada, Spain
[5] Department of Astronomy and the Center for Cosmology and Astroparticle Physics, The Ohio State University, 4055 McPherson Lab, 140 West 18th Avenue, Columbus, OH 43221, USA
[6] Departamento de Astronomía y Astrofísica, Universidad de Valencia, 46100 Burjassot, Valencia, Spain
[7] Center for Astrophysics, 60 Garden Street, Cambridge, MA 02138, USA
[8] Departamento de Física y Astronomía, Universidad de Valparaíso, Avda. Gran Bretaña 1111, Valparaíso, Chile
Received 2013 September 10; accepted 2013 October 8; published 2013 November 11

ABSTRACT

We measure the differential microlensing of the UV Fe II and Fe III emission line blends between 14 quasar image pairs in 13 gravitational lenses. We find that the UV iron emission is strongly microlensed in four cases with amplitudes comparable to that of the continuum. Statistically modeling the magnifications, we infer a typical size of $r_s \sim 4\sqrt{M/M_\odot}$ light-days for the Fe line-emitting regions, which is comparable to the size of the region generating the UV continuum (∼3–7 light-days). This may indicate that a significant part of the UV Fe II and Fe III emission originates in the quasar accretion disk.

Key words: gravitational lensing: micro – quasars: emission lines

Online-only material: color figures

1. INTRODUCTION

Iron, the stable end product of nucleosynthesis, has a large number of energy levels, generating thousands of emission-line transitions distributed throughout the UV and optical bands that likely make Fe II the main emission-line contributor to the overall spectra of quasars and active galactic nuclei (AGNs). Statistical studies of quasar spectra find that variations between them are dominated by the relative strength of the Fe II emission (Boroson & Green 1992). In spite of the relevance of the iron lines to understanding the physics of AGNs, both the mechanism generating the Fe II emission (Ferland et al. 2009) and the spatial scale of the region where it is emitted (Barth et al. 2013) are poorly understood. Two bands of Fe II emission are usually studied (see, e.g., Baldwin et al. 2004): the UV pseudo-continuum between C III] λ1909 and Mg II λ2798, and the optical blends in the Hγ-Hβ region. The few reverberation mapping studies of Fe II indicate that the region emitting the UV Fe II lines (Maoz et al. 1993) is considerably smaller than the region emitting the optical Fe II lines (Kuehn et al. 2008; Barth et al. 2013).

The size of the region generating the broad emission lines (BELs) in quasars can be also inferred from the impact of microlensing on the BELs. In a multiply imaged quasar, the magnification of each image of the quasar varies with time due to lensing by the stars in the lens galaxy (see the review by Wambsganss 2006). The dependence of the microlensing magnification on the size of the emission region has been used to estimate the size of different quasar regions, including the accretion disk (see, e.g., Pooley et al. 2007; Morgan et al. 2010; Blackburne et al. 2011; Jiménez-Vicente et al. 2012), the broad-line region (BLR; Abajas et al. 2007; Sluse et al. 2012; Motta et al. 2012; Guerras et al. 2013), and the non-thermal X-ray emission region (Pooley et al. 2007; Morgan et al. 2008, 2012; Chartas et al. 2009; Dai et al. 2010; Blackburne et al. 2011; Mosquera et al. 2013). In the particular case of the iron emission lines, Sluse et al. (2007) analyzed spectra of RXS J1131−1231 and found that a large fraction of the optical Fe II emission arises in the outer parts of the BLR, although they also found evidence of a very compact region associated with Fe II. Evidence of significant microlensing of the UV Fe II emission was also found in Q2237+0305 (Sluse et al. 2011).

Here we study the microlensing of the UV iron emission in a sample of 14 pairs of lensed quasar images, combining the spectra compiled by Mediavilla et al. (2009) with new observations. In Section 2, we describe the data and the procedure used to isolate the Fe II and Fe III line emission from the continuum and then to measure its microlensing. In Section 3, we use the measured microlensing amplitudes to derive constraints on the size of the UV iron emitting region, and we discuss and summarize the results in Section 4.

2. DATA ANALYSIS

We started with the sample compiled by Mediavilla et al. (2009) and then added unpublished archival spectra taken with the VLT or the MMT, as summarized in Table 1. We focus on the wavelength region between the C III] λ1909 and Mg II λ2798 emission lines, and we will use these lines to define a flux ratio baseline that is only weakly affected by microlensing (Mediavilla et al. 2009, 2011b; Guerras et al. 2013). Table 2 defines the wavelength regions we consider. We loosely follow the definition of the Fe II wavelength windows by Francis et al. (1991). The primary modification is that we do not include the regions around C III] λ1909 to avoid modeling the blended emission. Iron emission is split into two windows designated Fe(1), dominated by Fe III, and Fe(2), dominated by Fe II (Vestergaard & Wilkes 2001), each bracketed by line-free continuum regions (Kuraszkiewicz et al. 2002; Francis et al. 1991; Brotherton et al. 2001). Fe(1) corresponds to 2050–2115 Å, and Fe(2) corresponds to three regions: 2250–2320 Å, 2333–2445 Å, and 2470–2625 Å.

Table 1
Summary of Data

Object (pair)	z	Observation Date	Rest Wavelength (Å)	Reference
HE 0047−1756 A, B	1.67	2002 Sep 4	(1461–2547)	Wisotzki et al. 2004
HE 0435−1223 A, B	1.689	2008 Jan 12	(1210–3030)	Motta, V., unpublished data
HE 0435−1223 B, D	1.689	2004 Oct 12	(1638–2996)	Motta, V., unpublished data
SDSS 0806+2006 A, B	1.54	2005 Apr 12	(1575–3504)	Inada et al. 2006
SBS 0909+532 A, B	1.38	2003 Mar 7	(0750–5695)	Mediavilla et al. 2005
SDSS J0924+0219 A, B	1.524	2005 Jan 14	(1783–3170)	Eigenbrod et al. 2006
FBQ 0951+2635 A, B	1.24	1997 Feb 14	(1786–4018)	Schechter et al. 1998
QSO 0957+561 A	1.41	1999 Apr 15	(0913–4149)	Goicoechea et al. 2005
QSO 0957+561 B	1.41	2000 Jun 2–3	(0913–4149)	Goicoechea et al. 2005
QSO 0957+561 A, B	1.41	2008 Jan 13	(1330–3380)	Motta et al. 2012
SDSS J1001+5027 A, B	1.838	2003 Nov 20	(1409–3136)	Oguri et al. 2005
HE 1104−1805 A, B	2.32	2008 Apr 7	(1310–2909)	Motta et al. 2012
SDSS J1206+4332 A, B	1.789	2004 Jun 21	(1362–3048)	Oguri et al. 2005
SDSS J1353+1138 A, B	1.629	2005 Apr 12	(1521–3385)	Inada et al. 2006
WFI J2033−4723 B, C	1.66	2008 Apr 14	(1620–3625)	Motta, V., unpublished data
HE 2149−2745 A, B	2.033	2000 Nov 19	(1430–3174)	Motta, V., unpublished data

Table 2
Wavelength Regions

Feature	Wavelength Intervals (Å)	Description
Fe(1)	(λ2050[a], λ2115)	
Fe(2)	(λ2250, λ2320) ∪ (λ2333, λ2445) ∪ (λ2470, λ2625)	
Continuum	(λ2000, λ2020)[b]	Blueward of Fe(1)
Continuum	(λ2160, λ2180)[c]	Redward of Fe(1)
Continuum	(λ2225, λ2250)[c]	Blueward of Fe(2)
Continuum	(λ2640, λ2650)[d]	Redward of Fe(2)
Mg II λ2798	(λ2776, λ2820)	Line core
C III] λ1909	(λ1893, λ1925)	Line core

Notes.
[a] Originally taken at λ1942 in Vestergaard & Wilkes (2001).
[b] Contaminated with the wing of the C III] λ1909 line (Kuraszkiewicz et al. 2002).
[c] Pure continuum window according to Kuraszkiewicz et al. (2002).
[d] As suggested in Francis et al. (1991). This continuum window is defined out of the Mg II λ2798 wings (Brotherton et al. 2001) and of the iron blend Fe(2).

We first fit four straight lines to the continuum regions bracketing the Fe emission windows (plus a continuum region blueward of the C III] λ1909 line and another redward of the Mg II λ2798 line) and subtract them from the spectrum. Then, for each image-pair we normalize the continuum-subtracted spectra to match the core of the Mg II λ2798 emission lines defined by the total flux within ± FWHM/2 of the line center. Provided that these low-ionization lines are only weakly affected by microlensing, as we found in Guerras et al. (2013), the normalization constant (that is, the ratio between the Mg II λ2798 emission lines) gives us the intrinsic macrolens magnification between the images. The flux ratio of the continuum as compared to that of the Mg II λ2798 emission lines then gives us an estimate of the continuum microlensing magnification:

$$\Delta m_{\rm cont} = (m_1 - m_2)_{\rm cont} - (m_1 - m_2)_{\rm Mg\,II\,\lambda2798}. \quad (1)$$

In Figure 1, the superposition of the continuum-subtracted and normalized (to the Mg II λ2798 emission line) spectra is shown for each image-pair. The average Sloan Digital Sky Survey (SDSS) quasar spectrum (Vanden Berk et al. 2001), continuum-subtracted following the same procedures, is shown for comparison. In all cases (except SBS 0909+532 and SDSS J1353+1138) the Mg II λ2798 based normalization also matched the C III] λ1909 emission lines well, which shows that the continuum subtraction procedure has worked well and that there are no significant effects due to differential atmospheric refraction or slit misalignments. The exceptions were SBS 0909+532, which is strongly affected by differential extinction in the lens galaxy (Motta et al. 2002; Mediavilla et al. 2005, 2011b), and, at a lower level, SDSS J1353+1138. Assuming that the differences in normalization between the C III] λ1909 and the Mg II λ2798 emission lines in these two objects arise from extinction, we have applied a linear extinction correction to match both emission lines simultaneously.

Examining Figure 1, we see significant differences between the spectra in the region between C III] λ1909 and Mg II λ2798 in four cases: SDSS J0806+2006AB, FBQS J0951+2635AB, QSO 0957+561AB, and SDSS J1353+1138. For each pair of images, 1 and 2, we can estimate the microlensing in the two Fe regions by comparing the differential flux ratios between the iron blends and the Mg II λ2798 line that sets the baseline for no microlensing magnification. For example, we define

$$\Delta m_{\rm Fe(1)} = (m_1 - m_2)_{\rm Fe(1)} - (m_1 - m_2)_{\rm Mg\,II\lambda2798} \quad (2)$$

for region Fe(1) and similarly $\Delta m_{\rm Fe(2)}$ for region Fe(2). The same analysis can be performed using C III] λ1909 as the unmicrolensed baseline. For C III] λ1909, the definition of the continuum below the line is not as well defined as Mg II λ2798,

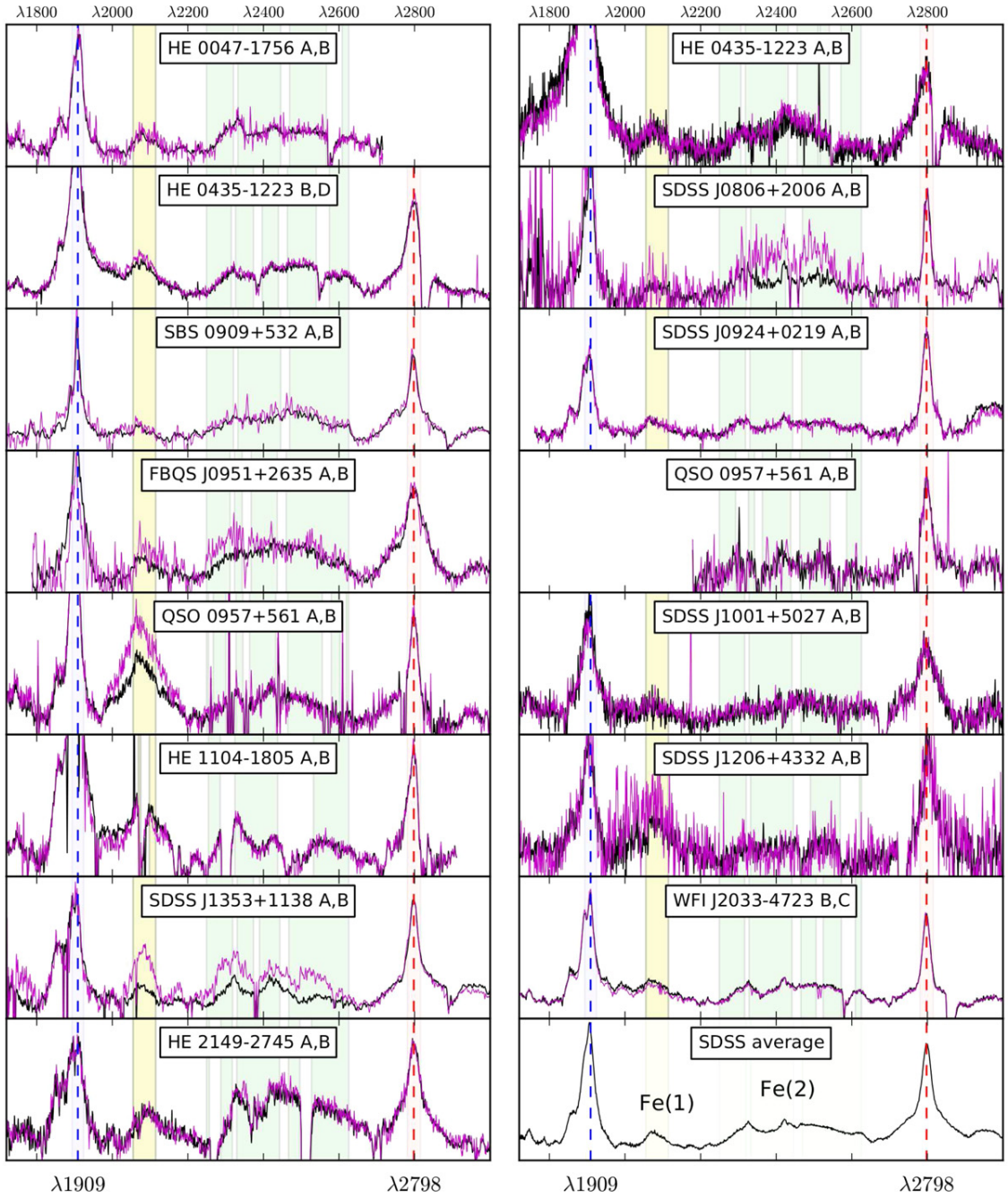

Figure 1. Panels showing superpositions of the paired spectra after continuum subtraction. The shaded regions show the wavelength intervals used for the C III] λ1909 line core, the Fe(1) blend, the Fe(2) blend, and the Mg II λ2798 line core, respectively (see Table 2). In the cases of SBS 0909+532 and SDSS J1353+1138 a linear model was used to correct for differential extinction between the images.

(A color version of this figure is available in the online journal.)

so these results should be treated with more caution. Using the C III] λ1909 line, we can then define estimates of the microlensing amplitudes $\Delta m'_{\rm cont}$, $\Delta m'_{\rm Fe(1)}$, and $\Delta m'_{\rm Fe(2)}$. All the resulting microlensing estimates are presented in Tables 3 and 4.

In Figure 2 we compare the microlensing magnification estimates for the continuum underlying each line or blend, C III] λ1909, Mg II λ2798, Fe(1), and Fe(2), finding very good linear covariances. The Pearson correlation coefficients are above 0.92 in all cases, with one-tailed p-values well under 0.01. In the same figures we also compare the microlensing measured in the Fe(1) and Fe(2) line regions with the microlensing of the continuum regions adjacent to the C III] λ1909 and Mg II λ2798 emission lines. We find that the Fe(1) line region has a low degree of correlation with the continuum, while the Fe(2) line region is uncorrelated.

3. CONSTRAINING THE SIZE OF THE UV IRON EMISSION LINE REGION

We follow the procedure we used in Guerras et al. (2013) to estimate the size of the emission regions corresponding to Fe(1), Fe(2), and the continuum regions adjacent to the Mg II λ2798 and C III] λ1909 emission lines. We start by computing microlensing magnification maps using the inverse

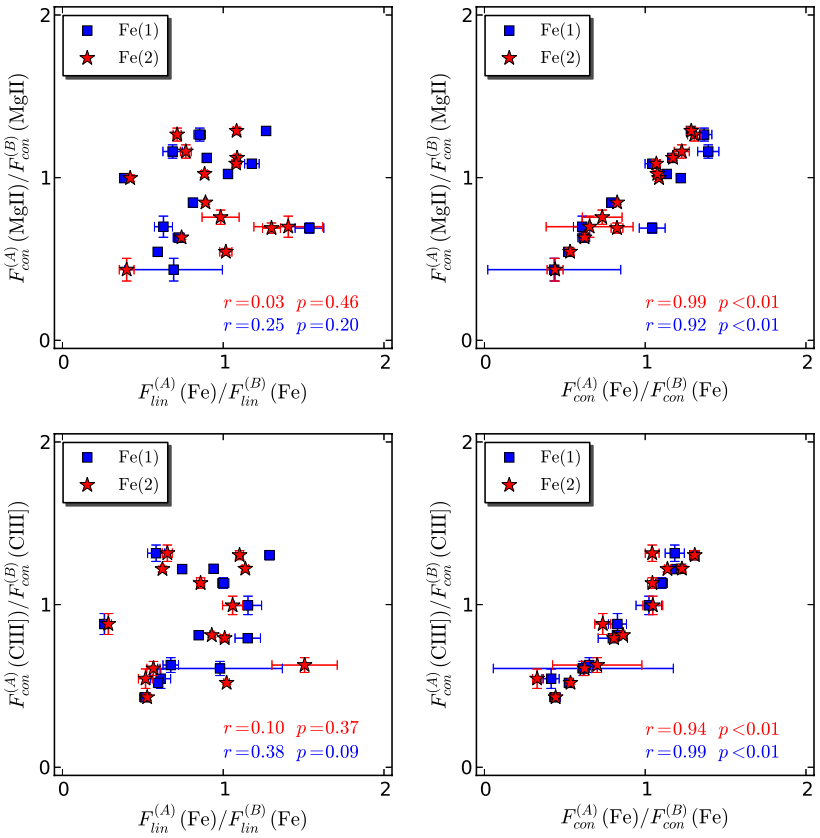

Figure 2. Comparison of Fe(1) and Fe(2) emission line and continuum flux ratios with the Mg II λ2798 (top) and C III] λ1909 continuum ratios (bottom). Blue squares correspond to Fe(1), and red stars correspond to Fe(2).

(A color version of this figure is available in the online journal.)

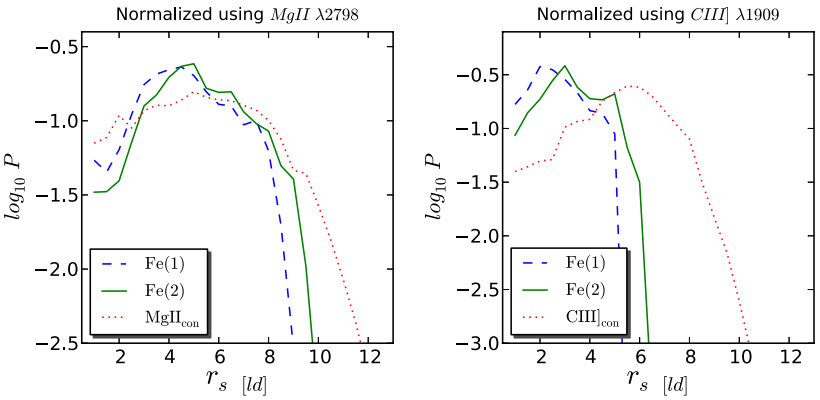

Figure 3. Posterior probabilities for a uniform prior on r_s. In the left (right) panel, the baseline for no microlensing magnification was set using the Mg II λ2798 (C III] λ1909) emission line. The dashed, solid, and dotted curves correspond to Fe(1), Fe(2), and the continuum region associated with the normalizing line, Mg II λ2798 (left) or C III] λ1909 (right).

(A color version of this figure is available in the online journal.)

polygon mapping technique (Mediavilla et al. 2006, 2011a). We take the dimensionless surface density, κ, and shear, γ, for each image from the lens models by Mediavilla et al. (2009) and Mediavilla et al. (2011b). We assume a mass fraction in stars of 5% (Abajas et al. 2007; Mediavilla et al. 2006; Pooley et al. 2009, 2012) and a stellar mass of $M = 1\,M_{\odot}$. We generate microlensing magnification maps with an outer scale of 1100 light-days and with a pixel scale of 0.04 Einstein radii (equal to 0.6 light-days in the worst case). Each magnification map is unit normalized and convolved with a Gaussian of size r_s, $I \propto \exp(-R^2/2r_s^2)$ to model the source. We consider a linear (logarithmic) grid of sizes from $r_s = 1.5$ to 13 light-days with steps $\Delta r_s = 0.5$ light-days ($\Delta \log_{10} r_s = 0.0408$). The probability of observing a magnitude difference $\Delta m_{\mathrm{obs},k}$ for image pair k ($k = 1, \ldots, 14$) given a source size r_s is then

$$p_k(\Delta m_{\mathrm{obs},k}|r_s) \propto \int f_{r_s,k,1}(m_1) f_{r_s,k,2}(m_1 - \Delta m_{\mathrm{obs},k}) dm_1, \quad (3)$$

where $f_{r_s,k,1}(m)$ and $f_{r_s,k,2}(m)$ are the frequency histograms obtained from the convolved magnification maps for images 1 and

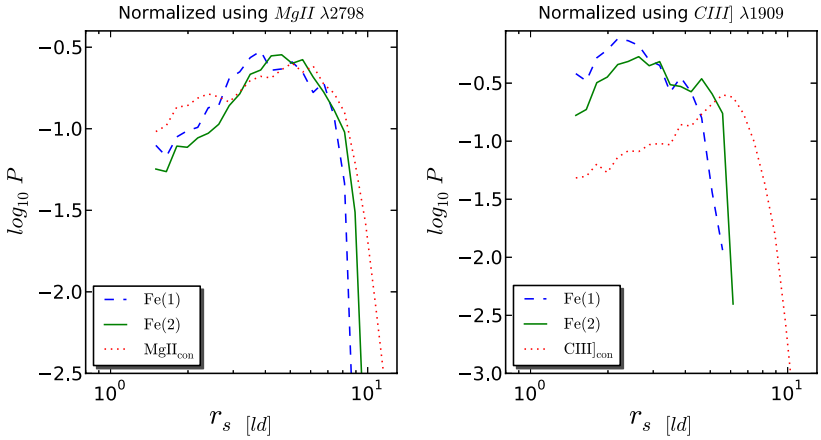

Figure 4. Same as Figure 3 but with a logarithmic prior on r_s.
(A color version of this figure is available in the online journal.)

Table 3
Differential Microlensing Using Mg II λ2798 as Reference

Object (pair)	Fe(1) Region	Fe(2) Region	λ2798 Continuum
HE 0435−1223 (B-A)	$+0.17^{+0.05}_{-0.04}$	$+0.37^{+0.04}_{-0.04}$	$-0.26^{+0.03}_{-0.03}$
HE 0435−1223 (D-B)	$+0.23^{+0.01}_{-0.01}$	$+0.13^{+0.01}_{-0.01}$	$+0.18^{+0.01}_{-0.01}$
SDSS J0806+2006 (B-A)	$+0.40^{+0.63}_{-0.39}$	$+1.00^{+0.13}_{-0.12}$	$+0.91^{+0.19}_{-0.16}$
SBS 0909+532 (B-A)	$-0.47^{+0.07}_{-0.06}$	$-0.29^{+0.05}_{-0.05}$	$+0.40^{+0.05}_{-0.05}$
SDSS J0924+0219 (B-A)	$+0.12^{+0.02}_{-0.02}$	$-0.09^{+0.02}_{-0.02}$	$-0.12^{+0.02}_{-0.02}$
FBQS J0951+2635 (B-A)	$+0.35^{+0.05}_{-0.05}$	$+0.33^{+0.02}_{-0.02}$	$+0.50^{+0.02}_{-0.02}$
QSO 0957+561 (B-A)	...	$+0.02^{+0.14}_{-0.12}$	$+0.30^{+0.06}_{-0.06}$
QSO 0957+561 (B-A)	$+0.57^{+0.04}_{-0.04}$	$-0.02^{+0.04}_{-0.04}$	$+0.66^{+0.04}_{-0.04}$
SDSS J1001+5027 (B-A)	$+0.41^{+0.10}_{-0.09}$	$+0.29^{+0.05}_{-0.05}$	$-0.16^{+0.04}_{-0.04}$
HE 1104−1805 (B-A)	$-0.18^{+0.04}_{-0.04}$	$-0.08^{+0.03}_{-0.03}$	$-0.09^{+0.02}_{-0.02}$
SDSS J1206+4332 (A-B)	$+0.50^{+0.10}_{-0.09}$	$-0.37^{+0.18}_{-0.15}$	$+0.39^{+0.11}_{-0.10}$
SDSS J1353+1138 (A-B)	$+1.04^{+0.03}_{-0.03}$	$+0.94^{+0.02}_{-0.02}$	$+0.00^{+0.02}_{-0.02}$
WFI J2033−4723 (B-C)	$-0.26^{+0.02}_{-0.02}$	$-0.09^{+0.02}_{-0.02}$	$-0.27^{+0.02}_{-0.02}$
HE 2149−2745 (B-A)	$-0.03^{+0.03}_{-0.03}$	$+0.13^{+0.02}_{-0.02}$	$-0.02^{+0.02}_{-0.02}$

Notes. $\Delta m - \Delta m_{\rm Mg\,II\,\lambda2798}$, of the Fe(1) and Fe(2) blends after continuum subtraction, and of the Mg II λ2798 continuum. The Mg II λ2798 emission line flux (after continuum subtraction) is used as the no-microlensing reference in all cases.

Table 4
Differential Microlensing Using C III] λ1909 as Reference

Object (pair)	Fe(1) Region	Fe(2) Region	λ1909 Continuum
HE 0047−1756 (B-A)	$-0.15^{+0.08}_{-0.07}$	$-0.01^{+0.03}_{-0.03}$	$+0.25^{+0.03}_{-0.03}$
HE 0435−1223 (B-A)	$+0.32^{+0.03}_{-0.03}$	$+0.52^{+0.02}_{-0.02}$	$-0.21^{+0.02}_{-0.02}$
HE 0435−1223 (D-B)	$+0.18^{+0.02}_{-0.02}$	$+0.08^{+0.02}_{-0.02}$	$+0.23^{+0.02}_{-0.02}$
SDSS J0806+2006 (B-A)	$+0.02^{+0.55}_{-0.36}$	$+0.62^{+0.08}_{-0.08}$	$+0.54^{+0.08}_{-0.07}$
SBS 0909+532 (B-A)	$+0.54^{+0.12}_{-0.10}$	$+0.72^{+0.10}_{-0.09}$	$+0.66^{+0.13}_{-0.11}$
SDSS J0924+0219 (B-A)	$+0.07^{+0.02}_{-0.02}$	$-0.14^{+0.02}_{-0.02}$	$-0.22^{+0.02}_{-0.02}$
FBQS J0951+2635 (B-A)	$+0.72^{+0.07}_{-0.07}$	$+0.70^{+0.04}_{-0.04}$	$+0.92^{+0.05}_{-0.04}$
QSO 0957+561 (B-A)	$+0.56^{+0.02}_{-0.02}$	$-0.02^{+0.02}_{-0.02}$	$+0.71^{+0.02}_{-0.02}$
SDSS J1001+5027 (B-A)	$+0.59^{+0.10}_{-0.09}$	$+0.46^{+0.05}_{-0.05}$	$-0.30^{+0.04}_{-0.04}$
HE 1104−1805 (B-A)	$-0.16^{+0.08}_{-0.08}$	$-0.06^{+0.07}_{-0.06}$	$+0.01^{+0.06}_{-0.06}$
SDSS J1206+4332 (A-B)	$+0.43^{+0.08}_{-0.08}$	$-0.44^{+0.16}_{-0.14}$	$+0.50^{+0.08}_{-0.08}$
SDSS J1353+1138 (A-B)	$+1.46^{+0.08}_{-0.08}$	$+1.36^{+0.08}_{-0.07}$	$+0.14^{+0.08}_{-0.08}$
WFI J2033−4723 (B-C)	$-0.28^{+0.02}_{-0.02}$	$-0.11^{+0.02}_{-0.02}$	$-0.29^{+0.02}_{-0.02}$
HE 2149−2745 (B-A)	$+0.00^{+0.04}_{-0.04}$	$+0.16^{+0.03}_{-0.03}$	$-0.13^{+0.03}_{-0.03}$

Notes. $\Delta m - \Delta m_{\rm C\,III]\,\lambda1909}$, of the Fe(1) and Fe(2) features after continuum subtraction, and of the C III] λ1909 continuum. The C III] λ1909 emission line flux (after continuum subtraction) is used as the no-microlensing reference in all cases.

2 (of pair k), respectively. The joint likelihood for all the image pairs,

$$L(\Delta m_{\rm obs,1}, \ldots, \Delta m_{\rm obs,14}|r_s) = \prod_{k=1}^{14} p_k(\Delta m_{{\rm obs},k}|r_s), \quad (4)$$

then gives the likelihood distribution for the size r_s.

Normalizing the likelihood functions to unity gives the Bayesian posterior probabilities with either a uniform (linear grid) or logarithmic (log grid) prior on r_s. Figures 3 and 4 show, for linear and logarithmic grids, respectively, the resulting probability distributions for the Fe(1) and Fe(2) line regions, and the continuum under the Mg II λ2798 (C III] λ1909) line when using the Mg II λ2798 (C III] λ1909) line to estimate the flux ratios in the absence of microlensing. The most significant result is that the UV iron blends seem to originate in a region with a size comparable to that of the underlying UV continuum. From these posterior probability distributions we obtain size estimates, in $\sqrt{M/M_\odot}$ light-day units, for the uniform (logarithmic) prior of $r_s = 5.3 \pm 2.4$ ($r_s = 5.3 \pm 2.1$) and $r_s = 5.3 \pm 1.8$ ($r_s = 5.3 \pm 1.7$) for the Mg II λ2798 and C III] λ1909 continua, respectively. This is in reasonable agreement with current expectations about the size of the region generating the continuum in quasars (e.g., Morgan et al. 2010; Jiménez-Vicente et al. 2012). We obtain similar sizes, in $\sqrt{M/M_\odot}$ light-day units, for the Fe(1) and Fe(2) line emission regions with $r_s = 4.6 \pm 1.8$ ($r_s = 4.8 \pm 1.7$) and $r_s = 5.1 \pm 1.8$ ($r_s = 5.1 \pm 1.7$), using the Mg II λ2798 lines as the magnification reference, and $r_s = 2.7 \pm 1.1$ ($r_s = 2.9 \pm 0.9$) and $r_s = 3.3 \pm 1.2$ ($r_s = 3.4 \pm 1.1$), using C III] λ1909. While the C III] λ1909 estimates are systematically smaller, the results are statistically consistent.

4. DISCUSSION AND CONCLUSIONS

We have found evidence that the UV iron line pseudo-continuum regions are microlensed, with amplitudes

comparable to those of nearby continuum emission regions. When we formally estimate the size, we find $r_s \sim 4\sqrt{M/M_\odot}$ light-days, slightly smaller than the continuum regions ($r_s \sim 3$–$7\sqrt{M/M_\odot}$ light-days), and far smaller than either the high- or low-ionization line emission regions in the BLR, as estimated with either microlensing (Guerras et al. 2013) or reverberation mapping (see, e.g., Zu et al. 2011). These quantitative results should be regarded as preliminary since the sample is small and a single object (SDSS J1353+1138) has a disproportionate impact on the size estimates. In any case, our estimate for the size is in reasonable agreement with the results for the UV Fe II emission region based on reverberation mapping by Maoz et al. (1993). Other reverberation mapping studies indicate that the Fe II optical emission lines arise from a substantially larger region (Kuehn et al. 2008; Barth et al. 2013). However, Sluse et al. (2007) also found that a part of the optical Fe II emission may originate in a more compact region.

It is also interesting to explore the shape of the spectra to know whether microlensing acts selectively over some components of the pseudo-continuum and may shed light on the structure and kinematics of the inner regions of quasars. The shape of the unmicrolensed spectra resembles the average SDSS quasar spectra well (see Figure 1). The microlensed spectra, however, seem to be selectively enhanced at some of the spectral features in the iron emission templates from Vestergaard & Wilkes (2001). This is particularly true for the Fe(1) blend that appears strongly magnified in three of the four microlensed objects. On the other hand, in the Fe(2) blend of SDSS J1353+1138 (see also the low signal-to-noise ratio (S/N) spectra from FBQS J0951+2635 and SDSS J0806+2006), the enhanced features look broader and more flat-topped. Notice, in particular, the relative weakness of the C II] λ2326 emission line compared to the unmicrolensed spectra and the strong enhancement of the Fe II emission at ∼2300 Å that can be hardly identified in the average SDSS quasar spectrum. A similar relative enhancement of the Fe II emission around the (tentatively identified) Fe III λ2418 (narrow) + [Ne IV] λ2423 blend is observed in SDSS J0806+2006. High-S/N spectra, combined with detailed modeling of the iron emission, could help to understand both the origin of the iron emission and the structure of the innermost regions of quasars (inner BLR or/and accretion disk).

In a series of papers, we used archival spectra of lensed quasars and microlensing to measure the fraction of matter in compact objects (Mediavilla et al. 2009), the size of a quasar's accretion disk (Mediavilla et al. 2011b; Jiménez-Vicente et al. 2012), the size of the BLR (Guerras et al. 2013), and the temperature profile of the quasar's accretion disk (J. Jiménez-Vicente et al., in preparation). It is clear that the next step is to revisit these objects to search for spectral changes, or even to begin systematic spectroscopic monitoring.

This research was supported by the Spanish Ministerio de Educación y Ciencia with the grants AYA2010-21741-C03-01/02 and AYA2011-24728. J.J.V. is also supported by the Junta de Andalucía through the FQM-108 project. J.A.M. is also supported by the Generalitat Valenciana with the grant PROMETEO/2009/64. C.S.K. is supported by NSF grant AST-1009756. V.M. gratefully acknowledges support from FONDECYT through grant 1120741.

REFERENCES

Abajas, C., Mediavilla, E., Muñoz, J. A., Gómez-Álvarez, P., & Gil-Merino, R. 2007, ApJ, 658, 748
Baldwin, J. A., Ferland, G. J., Korista, K. T., Hamann, F., & LaCluyzé, A. 2004, ApJ, 615, 610
Barth, A. J., Pancoast, A., Bennert, V. N., et al. 2013, ApJ, 769, 128
Blackburne, J. A., Pooley, D., Rappaport, S., & Schechter, P. L. 2011, ApJ, 729, 34
Boroson, T. A., & Green, R. F. 1992, ApJS, 80, 109
Brotherton, M. S., Tran, H. D., Becker, R. H., et al. 2001, ApJ, 546, 775
Chartas, G., Kochanek, C. S., Dai, X., Poindexter, S., & Garmire, G. 2009, ApJ, 693, 174
Dai, X., Kochanek, C. S., Chartas, G., et al. 2010, ApJ, 709, 278
Eigenbrod, A., Courbin, F., Dye, S., et al. 2006, A&A, 451, 747
Ferland, G. J., Hu, C., Wang, J.-M., et al. 2009, ApJL, 707, L82
Francis, P. J., Hewett, P. C., Foltz, C. B., et al. 1991, ApJ, 373, 465
Goicoechea, L. J., Gil-Merino, R., & Ullán, A. 2005, MNRAS, 360, L60
Guerras, E., Mediavilla, E., Jiménez-Vicente, J., et al. 2013, ApJ, 764, 160
Inada, N., Oguri, M., Becker, R. H., et al. 2006, AJ, 131, 1934
Jiménez-Vicente, J., Mediavilla, E., Muñoz, J. A., & Kochanek, C. S. 2012, ApJ, 751, 106
Kuehn, C. A., Baldwin, J. A., Peterson, B. M., & Korista, K. T. 2008, ApJ, 673, 69
Kuraszkiewicz, J. K., Green, P. J., Forster, K., et al. 2002, ApJ, 143, 257
Maoz, D., Netzer, H., Peterson, B. M., et al. 1993, ApJ, 404, 576
Mediavilla, E., Mediavilla, T., Muñoz, J. A., et al. 2011a, ApJ, 741, 42
Mediavilla, E., Muñoz, J. A., Falco, E., et al. 2009, ApJ, 706, 1451
Mediavilla, E., Muñoz, J. A., Kochanek, C. S., et al. 2005, ApJ, 619, 749
Mediavilla, E., Muñoz, J. A., Kochanek, C. S., et al. 2011b, ApJ, 730, 16
Mediavilla, E., Muñoz, J. A., Lopez, P., et al. 2006, ApJ, 653, 942
Morgan, C. W., Hainline, L. J., Chen, B., et al. 2012, ApJ, 756, 52
Morgan, C. W., Kochanek, C. S., Dai, X., Morgan, N. D., & Falco, E. E. 2008, ApJ, 689, 755
Morgan, C. W., Kochanek, C. S., Morgan, N. D., & Falco, E. E. 2010, ApJ, 712, 1129
Mosquera, A. M., Kochanek, C. S., Chen, B., et al. 2013, ApJ, 769, 53
Motta, V., Mediavilla, E., Falco, E., & Muñoz, J. A. 2012, ApJ, 755, 82
Motta, V., Mediavilla, E., Muñoz, J. A., et al. 2002, ApJ, 574, 719
Oguri, M., Inada, N., Hennawi, J. F., et al. 2005, ApJ, 622, 106
Pooley, D., Blackburne, J. A., Rappaport, S., & Schechter, P. L. 2007, ApJ, 661, 19
Pooley, D., Rappaport, S., Blackburne, J., et al. 2009, ApJ, 697, 1892
Pooley, D., Rappaport, S., Blackburne, J. A., Schechter, P. L., & Wambsganss, J. 2012, ApJ, 744, 111
Schechter, P. L., Gregg, M. D., Becker, R. H., et al. 1998, AJ, 115, 1371
Sluse, D., Claeskens, J.-F., Hutsemékers, D., & Surdej, J. 2007, A&A, 468, 885
Sluse, D., Hutsemékers, D., Courbin, F., Meylan, G., & Wambsganss, J. 2012, A&A, 544, A62
Sluse, D., Schmidt, R., Courbin, F., et al. 2011, A&A, 528, 100
Vanden Berk, D. E., Richards, G. T., Bauer, A., et al. 2001, AJ, 122, 549
Vestergaard, M., & Wilkes, B. J. 2001, ApJS, 134, 1
Wambsganss, J. 2006, Saas-Fee Advanced Course 33: Gravitational Lensing: Strong, Weak and Micro (Berlin: Springer), 453
Wisotzki, L., Schechter, P. L., Chen, H. W., et al. 2004, A&A, 419, L31
Zu, Y., Kochanek, C. S., & Peterson, B. M. 2011, ApJ, 735, 80

8

Conclusions and Work in Progress

We have explored the physical phenomenon of microlensing, applied to a real sample of quasar spectra, with the goal of extracting new information about both the lens galaxy and quasar source. This thesis includes a database of spectra from the literature, and four articles that made use of it. Three of them are statistical studies built on a set of differential microlensing measures across many objects of the sample, whereas the other article consists in the measures of many emission lines from the far UV to the NIR of a single object.

Throughout the four studies based on the database and the tools of Gravitational Microlensing, we have pursued different goals:

- The first work (Mediavilla et al. 2009) relied on the idea that the MACHO content of extragalactic halos would alter the shape of the differential microlensing measures histogram, thus we set up the goal of *constraining the mean values of the mass fraction in compact objects of lens halos.*

- The second study is based on the analysis of many spectral features (lines and continuum) from the far UV to the NIR (Mediavilla et al. 2011). The differential microlensing measures pointed out a wavelength dependence of the continuum magnification, that was the basic idea leading to the attempt of *a characterization of the temperature profile of the accretion disk.*

- The third work (Guerras et al. 2013) departed from the idea that the core and the wings of broad emission lines (BEL) arise from different regions. Since microlensing is sensitive to the size of the emitting region, we set up as our goal *measuring the size of the region giving rise to the broad emission in quasars.*

- The last work (Guerras et al. 2014) was born from having consistently observed, while working in the other articles, the presence of several very broad blends of iron lines in the spectra. Thanks to the addition of some new spectra to the database, we could attempt a statistical study of the microlensing of the UV iron blends, that could shed some light on the poorly understood *origin of the Iron emission in quasars.*

Regarding the completion of the goals, the database has proven to be useful. A review of the most important results follows:

- We have extended to the extragalactic domain the local use of microlensing to probe the properties of galaxy halos, making a contribution to the missing dark matter problem. Our results impose an upper limit of 10% of the mass in microlenses in galactic halos, or even less, depending upon the size of the quasar source. The amount of microlensing detected can be explained by the presence of the normal star populations, thus being compatible with very low or no content at all of MACHOs in galactic halos.

- Microlensing has proven to be a useful tool in extracting information about the structure of the accretion disk at the very centre of the quasar engine. From the chromatic microlensing measures in SBS 0909+532, we were able to derive a temperature profile that is consistent with the $\lambda^{3/4}$ power law of the thin disk model.

- Our microlensing size estimates for the Broad Line Region (BLR) are in good agreement with those obtained by previous studies based upon reverberation mapping. Additionally, the High Ionization Lines seem to arise from a more compact region than the Low Ionisation Lines.

- The final study on the UV Iron emission gives the first microlensing-based clues about its origin. Measures of the microlensing magnification of the iron blended

line quotients are similar to those of the continuum emission. In fact, our numerical estimates show that the iron lines may arise from the very inner part of the engine, in a region as compact as the accretion disk. Such results are in reasonable agreement with some reverberation mapping estimates on single active galaxies.

The next step in microlensing-based[1] future developments is achieving a second epoch of spectroscopic observations for the objects in the database, to study microlensing variability. Spectroscopic monitoring of several objects on a regular basis would provide direct evidence of caustic crossing, powerfully adding constraints that are needed if we want to narrow the uncertainties and achieve better models for the quasar structure. Possible applications include:

- High resolution studies of the possible BLR structure, revealed by chromatic asymmetries in the wings of lensed spectra,
- Narrowing the uncertainties in the BLR size determination, allowing a better distinction between high ionization lines (HIL) and low ionization lines (LIL).
- The application of iron emission templates to separate possible different emission regions giving rise to the blends.
- Mapping the extinction curves of galaxies at intermediate redshifts.

To name just a few. Essentially, multi-epoch lensed spectra together with an improvement in the homogeneity of the measures (the same lines observed for all the objects, with the same instrumentation) will open the door to a deeper understanding of lensed quasars.

[1] This thesis work relies on models that consider only compact objects as substructure. However, the $SIS + \gamma$ models fit the observed flux ratios poorly in lenses with more than two images. Microlensing alone cannot possibly account for that discrepancies because they appear also in radio wavelengths, where the size of the emitting region is too big to be significantly affected by microlensing. The presence of intermediate-sized dark matter clumps causing millilensing is the most likely explanation and it constitutes a very interesting direction for future research (e.g. Metcalf & Amara 2012, Zackrisson & Riehm 2010, Kochanek & Dalal 2004).

References

[1] C Alcock, RA Allsman, DR Alves, TS Axelrod, AC Becker, et al. **The MACHO project: microlensing results from 5.7 years of Large Magellanic Cloud observations**. *The Astrophysical Journal*, **542**:281–307, 2000.

[2] AJ Barth, A Pancoast, VN Bennert, BJ Brewer, G Canalizo, et al. **The lick AGN monitoring project 2011: Fe II reverberation from the Outer Broad-Line Region**. *The Astrophysical Journal*, **769**:128, 2013.

[3] M Born. **Zur Quantenmechanik der Stoßvorgänge**. *Zeitschrift fur Physik*, **37**:863–867, 1926.

[4] Bradley M Peterson. *An introduction to Active Galactic Nuclei*. Cambridge, 1997.

[5] BW Carroll and DA Ostlie. *An introduction to modern Astrophysics*. Addison-Wesley, San Francisco: Pearson, 2nd (international) edition, 2007.

[6] O Chwolson. **Über eine mögliche Form fiktiver Doppelsterne**. *Astronomische Nachrichten*, **221**:329, 1924.

[7] VH Chavushyan. **SBS 1520+ 530: a new gravitationally lensed system at z= 1.855.** *Astronomy and Astrophysics*, **70**:67–70, 1997.

[8] A Eigenbrod, F Courbin, S Dye, G Meylan, D Sluse, et al. **Astrophysics COSMOGRAIL : the COSmological MOnitoring II . SDSS J0924 + 0219 : the redshift of the lensing galaxy , the quasar spectral variability and the Einstein rings**. *Astronomy and Astrophysics*, **757**:747–757, 2006.

[9] A Einstein. **Die Grundlage der allgemeinen Relativitätstheorie**. *Annalen der Physik*, **354**(7):769–822, 1916.

[10] A Einstein. *Vier Vorlesungen über Relativitätstheorie*. Druck und Verlag, F. Vieweg, Braunschweig, 1921.

[11] A Einstein. **Lens-like action of a star by the deviation of light in the gravitational field**. *Science*, **84**:506–507, 1936.

[12] J Fohlmeister, CS Kochanek, EE. Falco, J Wambsganss, M Oguri, et al. **A two-year time delay for the lensed quasar SDSS J1029+2623**. *The Astrophysical Journal*, **764**:186, 2013.

[13] PJ Francis, PC Hewett, CB Foltz, FH Chaffee, RJ Weymann, et al. **A high signal-to-noise ratio composite quasar spectrum**. *The Astrophysical Journal*, **373**:465–470, 1991.

[14] LJ Goicoechea. **The dark halo of the main lens galaxy in QSO 0957+ 561**. *Monthly Notices of the Royal Astronomical Society*, **360**:L60–L63, 2005.

[15] P Gómez-Álvarez and E Mediavilla. **Recurrence of the blue wing enhancements in the high-ionization lines of SDSS 1004+ 4112A**. *The Astrophysical Journal*, **5**:1–5, 2006.

[16] E Guerras, E Mediavilla, J Jiménez-Vicente, CS Kochanek, Munoz JA, et al. **Microlensing of quasar broad emission lines: constraints on Broad Line Region size**. *The Astrophysical Journal*, **764**:160, 2013.

[17] E Guerras, E Mediavilla, J Jiménez-Vicente, CS Kochanek, Munoz JA, et al. **Microlensing of Quasar Ultraviolet Iron Emission**. *The Astrophysical Journal*, **778**:123, 2013.

[18] CD Impey, CB Foltz, CE Petry, IWA Browne, and AR Patnaik. **Hubble Space Telescope observations of the gravitational lens system B1422+231**. *The Astrophysical Journal*, **53**:L53, 1996.

[19] N Inada, M Oguri, RH Becker, RL White, MD Gregg, et al. **Sdss J0806+ 2006 and sdss J1353+ 1138: two new gravitationally lensed**

quasars from the Sloan Digital Sky Survey. *The Astronomical Journal*, **1934**:1934–1941, 2006.

[20] CR Keeton. **Computational methods for gravitational lensing**. *eprint arXiv:astro-ph/0102340*, 2001.

[21] CR Keeton, S Burles, PL Schechter, and J Wambsganss. **Differential microlensing of the continuum and broad emission lines in SDSS J0924+0219, the most anomalous lensed quasar**. *The Astrophysical Journal*, **639**:1–6, 2006.

[22] CS Kochanek and N Dalal. **Tests for Substructure in Gravitational Lenses**. *The Astrophysical Journal*, **610**:69–79, 2004.

[23] W Kollatschny. **Kinematics in the central Broad Line Region of AGN.** *Memorie della Societa Astronomica Italiana Supplementi*, **15**:94, 2010.

[24] JK Kuraszkiewicz and PJ Green. **Emission line properties of Active Galactic Nuclei from a pre-COSTAR faint object spectrograph Hubble Space Telescope spectral atlas**. *The Astrophysical Journal*, **143**:257–276, 2002.

[25] D Maoz and H Netzer. **Variations of the ultraviolet Fe II and Balmer continuum emission in the Seyfert galaxy NGC 5548**. *The Astrophysical Journal*, **404**:576–583, 1993.

[26] E Mediavilla, JA Munoz, CS Kochanek, E Falco, S Arribas, et al. **The first precise determination of an optical-far-ultraviolet extinction curve beyond the Local Group (z=0.83)**. *The Astrophysical Journal*, **749**:749–754, 2005.

[27] E Mediavilla, JA Munoz, P López, T Mediavilla, C Abajas, et al. **A fast and very accurate approach to the computation of microlensing magnification patterns Based on Inverse Polygon Mapping**. *The Astrophysical Journal*, **653**:942–953, 2006.

[28] E Mediavilla, JA Munoz, E Falco, V Motta, E Guerras, et al. **Microlensing-based estimate of the mass fraction in compact objects in lens galaxies**. *The Astrophysical Journal*, **706**:1451–1462, 2009.

[29] E Mediavilla, JA Munoz, CS Kochanek, E Guerras, J Acosta-Pulido, et al. **The structure of the accretion disk in the lensed quasar SBS 0909+532**. *The Astrophysical Journal*, **730**:16, 2011.

[30] RB Metcalf and A Amara. **Small-scale structures of dark matter and flux anomalies in quasar gravitational lenses**. *Monthly Notices of the Royal Astronomical Society*, **419**:3414–3425, 2012.

[31] ND Morgan and JAR Caldwell. **WFI J2026 4536 and WFI J2033 4723: Two new quadruple gravitational lenses**. *The Astronomical Journal*, **2617**:2617–2630, 2004.

[32] CW Morgan and CS Kochanek. **Microlensing of the lensed quasar SDSS 0924+ 0219**. *The Astrophysical Journal*, **647**:874–885, 2006.

[33] V Motta, E Mediavilla, E Falco, and JA Munoz. **Measuring microlensing using spectra of multiply lensed quasars**. *The Astrophysical Journal*, **755**:82, 2012.

[34] R Narayan and M Bartelmann. **Lectures on gravitational lensing**. *eprint arXiv:astro-ph/9606001*, 1996.

[35] J Navarro, CS Frenk, and SDM White. **The Structure of cold dark matter halos**. *Astrophysical Journal*, **462**:563, 1996.

[36] I Newton. *Philosophiae Naturalis Principia Mathematica*. London, 1687.

[37] M Oguri and N Inada. **Discovery of two gravitationally lensed quasars with image separations of 3"from the Sloan Digital Sky Survey**. *The Astrophysical Journal*, **106**:106–115, 2005.

[38] LČ Popović and G Chartas. **The influence of gravitational lensing on the spectra of lensed quasi-stellar objects**. *Monthly Notices of the Royal Astronomical Society*, **357**:135–144, 2005.

[39] S Refsdal. **On the possibility of determining Hubble's parameter and the masses of galaxies from the gravitational lens effect**. *Monthly Notices of the Royal Astronomical Society*, **128**:307, 1964.

[40] S Refsdal. **On the possibility of testing cosmological theories from the gravitational lens effect**. *Monthly Notices of the Royal Astronomical Society*, **134**:101, 1966.

[41] Gordon T Richards, Charles R Keeton, Bartosz Pindor, Joseph F Hennawi, Patrick B Hall, et al. **Microlensing of the Broad Emission Line Region in the quadruple lens SDSS J1004+4112**. *The Astrophysical Journal*, **610**:679–685, 2004.

[42] EE Salpeter. **Accretion of interstellar matter by massive objects.** *The Astrophysical Journal*, **140**:796–800, 1964.

[43] NI Shakura and RA Sunyaev. **Black holes in binary systems. Observational appearance**. *Astronomy and Astrophysics*, **24**:337–355, 1973.

[44] II Shapiro. **Fourth Test of General Relativity**. *Physical Review Letters*, **13**:789–791, 1964.

[45] PL Schechter, MD Gregg, RH Becker, DJ Helfand, and RL White. **The first FIRST gravitationally lensed quasar: FBQ 0951+2635**. *The Astronomical Journal*, **115**:1371–1376, 1998.

[46] M Schmidt. **Models of Quasi-stellar Sources**. In K. N. Douglas, I. Robinson, A. Schild, E. L. Schucking, J. A. Wheeler, et al., editors, *Quasars and high-energy astronomy*, page 55, 1969.

[47] Falco EE Schneider P, Ehlers J. *Gravitational Lenses*. Springer-Verlag, 1992.

[48] D Sluse and JF Claeskens. **Multi-wavelength study of the gravitational lens system RXS J1131-1231: III. Long slit spectroscopy: micro-lensing probes the QSO structure**. *Astronomy and Astrophysics*, **468**.

[49] J Surdej and JF Claeskens. **HST confirmation of the lensed quasar J03. 13.** *Astronomy and Astronphysics*, **4**:5–8, 1997.

[50] RM Wald. *General Relativity*. The University of Chicago Press, 1984.

[51] Weymann RJ Walsh D, Carswell RF. **0957 + 561 A, B - Twin quasistellar objects or gravitational lens**. *Nature*, **279**:381–384, 1979.

[52] Winston R et al. *Nonimaging optics*. Academic Press, 2004.

[53] L Wisotzki, T Becker, and L Christensen. **Integral-field spectroscopy of the quadruple QSO HE 0435-1223: evidence for microlensing**. *Astronomy and Astrophysics*, **463**:455–463, 2003.

[54] L Wisotzki and T Koehler. **Spectral variability in the double QSO HE 1104-1805: further evidence for gravitational lensing.** *Astronomy and Astrophysics*, **297**:L59, 1995.

[55] L Wisotzki, P L Schechter, H Chen, D Richstone, and K Jahnke. **HE 0047 1756 : A new gravitationally lensed double QSO**. *Astronomy and Astrophysics*, **34**:31–34, 2004.

[56] O Wucknitz, L Wisotzki, S López, and MD Gregg. **Disentangling microlensing and differential extinction in the double QSO HE0512-3329**. *Astronomy and Astrophysics*, **405**:445–454, 2003.

[57] DD Xu, D Sluse, L. Gao, J Wang, C Frenk, et al. **How well can cold-dark-matter substructures account for the observed lensing flux-ratio anomalies?** *eprint arXiv:astro-ph/1307.4220*, 2013.

[58] E Zackrisson and T Riehm. **Gravitational Lensing as a Probe of Cold Dark Matter Subhalos**. *eprint arXiv:astro-ph/0905.4075*, 2010.

[59] F Zwicky. **Nebulae as gravitational lenses**. *Phys. Rev.*, **51**:290–290, 1937.

Declaration

I herewith declare that I have produced this paper without the prohibited assistance of third parties and without making use of aids other than those specified; notions taken over directly or indirectly from other sources have been identified as such. This paper has not previously been presented in identical or similar form to any other Spanish or foreign examination board.

The thesis work was conducted under the supervision of Dr. Evencio Mediavilla Grádolph and Dr. Alejandro Oscoz Abad at the *Instituto de Astrofísica de Canarias (IAC)*.

Eduardo Guerras Valera